Probing Light-Matter Interactions in Plasmonic Nanotips

DISSERTATION

zur Erlangung des mathematisch-naturwissenschaftlichen Doktorgrades
"Doctor rerum naturalium"
der Georg-August-Universität Göttingen

im Promotionsprogramm ProPhys
der Georg-August University School of Science (GAUSS)

vorgelegt von

Benjamin Schröder

aus Georgsmarienhütte

Göttingen, 2020

Betreuungsausschuss

Prof. Dr. Claus Ropers, IV. Physikalisches Institut
Prof. Alec M. Wodtke, PhD, Institut für Physikalische Chemie/
Max-Planck-Institut für biophysikalische Chemie
PD Dr. Martin Wenderoth, IV. Physikalisches Institut

Mitglieder der Prüfungskomission

Referent: Prof. Dr. Claus Ropers, IV. Physikalisches Institut
Korreferent: Prof. Alec M. Wodtke, PhD, Institut für Physikalische Chemie/
Max-Planck-Institut für biophysikalische Chemie

Weitere Mitglieder der Prüfungskomission

PD Dr. Martin Wenderoth, IV. Physikalisches Institut
Prof. Cynthia A. Volkert, PhD, Institut für Materialphysik
Prof. Dr. Vasily Moshnyaga, I. Physikalisches Institut
Prof. Dr. Andreas Tilgner, Institut für Geophysik

Tag der mündlichen Prüfung: 14.07.2020

To my children

Abstract

The exploration of light-matter interaction has inspired some of the most essential theories and applications in fundamental science and technology. Cutting-edge research, such as ultrafast time-resolved and super-resolution experiments, relies on the in-depth knowledge of the interaction of photons and electrons. In these research fields, the controlled guiding, concentration, and conversion of electromagnetic energy are the central requirements of any technological advance.

This thesis explores the remarkable properties of nanotips featuring waveguiding, field enhancement, and energy localization of electromagnetic surface waves which arise from collective electron oscillations – called surface plasmons (SPs). Nanotips are key components in ultrafast time-resolved electron-beam and scanning probe techniques. However, a complete physical picture of the complex SP evolution is not yet established.

Here, we provide detailed contributions to the understanding of surface plasmons in metal nanotips studied in three experiments. In particular, we analyze the SP mode propagation along the tip shaft and its behavior when approaching the tip end by means of electron energy loss spectroscopy (EELS). EELS allows for spatially and spectrally resolved SP measurements. We find characteristic standing wave patterns in the SP maps and implement a semianalytical model that identifies SP back-reflection from the apex as the main reason for the observed standing waves. Our analysis reveals a reflection efficiency of nearly 100% for sufficiently small opening angles.

In a subsequent experiment, we exploit the near-field enhancement of SPs to investigate nonlinear photoelectron emission from gold tips. The SP modes are excited via direct apex illumination or via grating couplers milled into the shaft several tens of micrometers away from the tip end. We demonstrate efficient remote multiphoton photoemission driven by grating-coupled plasmons by inserting the tips into a field emitter assembly enabling the control of the active emission sites along the tip structure.

The final experiment explores the excitation of photoelectrons in a sub-nanometer gap between a gold tip and a flat metal substrate. For this purpose, the challenging combination of scanning tunneling microscopy with pulsed femtosecond-laser excitation is realized. Based on a one-dimensional transport model, electrons in the tip are found to absorb energy from the enhanced SP near-field in the gap. This results in a non-equilibrium charge distribution with electrons populating high-energy states and transferring to the sample. We use the locality of the photocurrent for a sophisticated imaging mode with nanometer precision.

Zusammenfassung

Die Erforschung von Licht-Materie-Wechselwirkung hat viele grundlegende Theorien und Anwendung in der Forschung und Technologie inspiriert. Aktuelle Forschungsprojekte, wie z.B. ultraschnelle zeit- und superaufgelöste Bildgebungsverfahren, sind auf tiefgreifendes Wissen über die Wechselwirkung von Photonen und Elektronen angewiesen. In diesen Forschungsfeldern ist der gezielte Transport, die Konzentration und die Umwandlung von elektromagnetischer Energie eine zentrale Voraussetzung für technologischen Fortschritt.

Diese Arbeit befasst sich mit den außergewöhnlichen Eigenschaften von Nanospitzen, die Wellenleitung, Feldverstärkung und Energielokalisierung von elektromagnetischen Oberflächenwellen erlauben. Diese Wellen entstehen durch kollektive Elektronenschwingungen in der Oberfläche und werden Oberflächenplasmonen (OP) genannt. Nanospitzen sind Schlüsselkomponenten in Experimenten, die auf gepulsten Elektronenstrahlen und Rastersonden basieren. Trotz dieser breiten Anwendung ist bisher noch kein vollständiges physikalisches Verständnis des komplexen Verhaltens von Oberflächenplasmonen etabliert.

Diese Arbeit bietet detaillierte Beiträge zum Verständnis von Oberflächenplasmonen in metallischen Nanospitzen anhand von drei Experimenten. Im Genauen analysieren wir die Ausbreitung von OP entlang des Spitzenschafts und das Verhalten bei Annäherung ans Spitzenende mithilfe von Elektronenenergieverlust-Spektroskopie (EELS). EELS erlaubt die spektral und räumlich aufgelöste Messung von OP. Wir messen charakteristische, stehende Wellenmuster und nutzen ein semi-analytisches Modell zur Beschreibung der Ausbreitung von OP. Dadurch können wir zeigen, dass die Plasmonen am Spitzenende mit nahezu 100% Effizienz reflektiert werden.

In einem anschließenden Experiment verwenden wir die Nahfeldverstärkung von OP um nichtlineare Elektronenemission von Goldspitzen zu untersuchen. Plasmonen werden entweder durch direkte Beleuchtung des Spitzenendes oder mittels Gitterkopplern angeregt, die einige zehn Mikrometer vom Spitzenende in die Oberfläche graviert sind. Wir demonstrieren eine effiziente Elektronenquelle basierend auf Plasmonen, die am Gitter angeregt werden. Dazu werden die Spitzen in einen Feldemitter eingebaut, der die Kontrolle über die aktiven Emissionsorte entlang der Spitzenstruktur erlaubt.

Das letzte Experiment untersucht die Anregung von Photoelektronen in der (Sub)-Nanometer breiten Lücke zwischen einer Goldspitze und einer flachen Metalloberfläche. Zu diesem Zweck wird die experimentell herausfordernde Kombination eines gepulsten Femtosekundenlasers mit einem Rastertunnelmikroskop realisiert. Basierend auf einem eindimensionalen Transportmodell, wird gezeigt, dass die Elektronen in der Spitze Energie vom verstärkten Nahfeld in der Lücke zwischen Spitze und Probe absorbieren. Dies führt zu einem Nichtgleichgewicht der Elektronenpopulation: Elektronen besetzen hochenergetische Zustände und transferieren in die Probe. Wir nutzen die Lokalisierung des Photoelektronenstroms für einen Bildgebungsmodus mit Nanometer-Genauigkeit.

Contents

List of Figures

List of Abbreviations and Symbols

Abbreviation	Meaning
ABH	Apparent barrier height
AFM	Atomic force microscopy
A-NSOM	Apertureless near-field scanning optical microscopy
ARPES	Angle-resolved photoemission spectroscopy
BPD	Beam position detector
CDM	Coupled dipole model
CL	Cathodoluminescence
CTP	Charge transfer plasmon
DGTD	Discontinuous Galerkin time domain
EEL	Electron energy loss
EELP	Electron energy loss probability
EELS	Electron energy loss spectroscopy
FER	Field emission resonance
FIB	Focused ion beam
fs-PPM	Femtosecond point-projection microscopy
fs-STM	Femtosecond scanning tunneling microscopy
FWHM	Full-width at half-maximum
GC	Grating coupler
HAADF	High-angle annular dark-field
HHG	High-harmonic generation
LEM	Local excitation microscopy
LSP	Localized surface plasmon
MCP	Micro channel plate
MPPE	Multiphoton photoemission
NRA	Non-recoil approximation
PEEM	Photoemission electron microscopy
PINEM	Photon-induced near-field electron microscopy
PML	Perfectly matched layer
SEM	Scanning electron microscopy
SP	Surface plasmon
SPP	Surface plasmon polariton
STEM	Scanning transmission electron microscopy
STM	Scanning tunneling microscopy
STS	Scanning tunneling spectroscopy
TEM	Transmission electron microscopy
TERS	Tip-enhanced Raman spectroscopy

TM	Transverse-magnetic
UHV	Ultrahigh vacuum
ULEED	Ultrafast low-energy electron diffraction
UTEM	Ultrafast transmission electron microscopy
ZLP	Zero-loss peak

Symbol	**Meaning**
A_I, A_R, and A_T	Amplitudes of incoming, reflected, and transmitted electron waves
A_j, ΔE_j, and E_j	Parameters for effective population function
α_ω and $\alpha_\omega^{\text{eff}}$	(Effective) polarizability
α_T	Tip opening angle
d_{sa} and d_{se}	Suppressor-apex and suppressor-extractor distances
d_{stm} and d_{feed}	Beam splitter-STM and beam splitter-feedback detector distance
E	Electron energy
ΔE	Electron energy loss
E_{vac}	Vacuum energy edge
E_F, $E_{F,T}$ and $E_{F,S}$	Fermi energy (of tip and sample)
E_e	Relativistic electron energy
e	Elementary charge
$\mathbf{E}_0$	Incident electric field
$\mathbf{E} = (E_x, E_y, E_z)$	Electric field
$\mathbf{E}^{\text{e}^-} = (E_r^{e^-}, 0, E_z^{e^-})$	Electric field of moving electron (cylindrical coordinates)
$\mathbf{E}^{\text{ind}} = (E_x^{\text{ind}}, E_y^{\text{ind}}, E_z^{\text{ind}})$	Induced electric field
$\mathbf{E}_{\text{nf}}$, $\mathbf{E}_{\text{nf}}^t$, $\mathbf{E}_{\text{nf}}^s$	Near-field (of tip and sample)
$\mathbf{E}^{\text{out}}$	Total field outside the nanostructure
$\varepsilon(\omega)$, ε_t, ε_s, and ε_d	Permittivity (of the tip, sample and dielectric)
ε_∞, $\Delta\varepsilon$, ω_D, ω_L, γ_D, and γ_L	Parameters for Drude-Lorentz model
ε_0	Vacuum permittivity
F_{sa} and F_{se}	Suppressor-apex and suppressor-extractor electrostatic forces
F	Field enhancement
$f(E)$	Fermi-Dirac distribution as a function of energy E
f^t and f^s	Population distribution of tip and sample
f_{eff} or $f_P(E)$	Effective population distribution
Γ and Γ_a	Field ratio of double plate capacitor and for pure apex emission
$\Gamma(\omega)$, $\Gamma^{\text{tip}}(\omega)$, $\Gamma_m(\omega)$, $\Delta\Gamma(\omega)$	EELP (of a tip, mode m, and modification due to reflection)
$\Gamma_P(E)$	Electron transfer for a given laser power P as a function energy E
I_{total}, I_{pc}, I_{SP}, I_n, and I	(Total, photo-induced, setpoint, partial) current
I_1 and I_2	Current of first and second photo channel
I_{ap} and I_{gr}	Photoemission current from apex and grating
I_ω	Local light intensity
k^t and k^s	Electron wave vector in the tip and sample
$\lvert\mathbf{k}\rvert = k$	Wave vector and wave number of light
Δk	Momentum mismatch
$\lvert\mathbf{k}_e\rvert = k_e$	Wave vector and wave number of electron induced field
κ, κ_{pc}, and κ_{tc}	Decay constant (for photocurrent and tunnel current)

L_{spp}	SPP propagation length
L_{vac} and L_{tip}	Transversal SPP decay length into vacuum and tip
λ	Wavelength of light
λ_{spp}	SPP wavelength
n	(Nonlinear) photon order/nonlinearity
M_{if}	Transition matrix element for $i \to f$ state change
m	Azimuthal mode order
m_e	Electron rest mass
ω	(Light) frequency
ω_p	Plasma frequency
ω_c	Cut-off frequency
ω_t	Threshold frequency
P	Laser power
$\mathbf{p}$, $\mathbf{p}_s$ and $\mathbf{p}_t$	Dipole moment (of tip and sample)
$\mathbf{p}_e$	Electron momentum vector
Φ, Φ_T, and Φ_S	Work function (of tip and sample)
Φ_{eff}	Effective work function
Φ_{ABH}, Φ_{pc}, and Φ_{tc}	Apparent barrier height (for photocurrent and tunnel current)
$\varphi_{\mathrm{spp}}(x_1, x_2)$	Accumulated SPP phase propagating from x_1 to x_2
ϕ	Angle
Ψ, Ψ^t, and Ψ^s	Electron wave function (of the tip and sample)
q	Longitudinal SPP wave number
q_{mR}	Longitudinal SPP wave number for mode m and cylinder radius R
q_t and q_d	Transversal SPP wave number in the tip and dielectric (vacuum)
R_T	Tip apex radius
$R(x)$ and $R'(x)$	Local radius along tip and its gradient
R_c	Cut-off radius
$\mathbf{r} = (x, y, z) = (x', y', z')$	Cartesian coordinates
$\mathbf{r} = (r, \varphi, z)$	Cylindrical coordinates
$\mathbf{r}_e = (x_e, y_e, v_e t)$	Electron trajectory
σ	Surface charge density
T	Transmission probability
T_0 and T_e	Initial and electronic temperature
T^t and T^s	Electron temperature of tip and sample
θ	Angle of incidence
U_{ext}, U_{sup}, and U_{tip}	Voltages applied to extractor, suppressor, and tip
U_B	Bias voltage
V, V^t, V^s, and V^g	Potential (of the tip, sample, and gap)
V_{img}, V^t_{img}, and V^s_{img}	Image potential (of tip and sample)
$\lvert\mathbf{v}\rvert = v_e$	Electron velocity
z	Relative tip-sample distance
z_{gap}	Tip-sample distance (gap width)
z_0	Tip position start point
Δz	Start point correction

CHAPTER 1

Introduction

Light-matter phenomena rank among the most prominent research objects in natural science including the photoelectric effect in physics [1, 2], supernovas in astronomy [3], photocatalysis in chemistry [4], as well as photosynthesis and vitamin D formation in biology [5, 6]. Modern research in solid state physics, surface science, and nanotechnology are inconceivable without analytical methods based on the interaction of matter with electromagnetic radiation (light), such as laser, photoemission, or X-ray spectroscopy, ultrafast[1] time-resolved imaging, and X-ray crystallography. In the mentioned techniques and processes, light provides the key functionalities of a flexible energy source and a fast information carrier that excites matter and can be used to analyze the involved interaction mechanisms and dynamics [7, 8].

Yet, there are plenty of open questions to explore in both fundamental science and technology. For example, effects in quantum optics may be utilized for quantum information processing [9, 10] and sample dynamics can be observed on a femtosecond timescale, which might be extended to the attosecond regime by next-generation pulse sources [11, 12]. Superresolution techniques allow to optically excite and investigate substances beyond the diffraction limit [13, 14] and strongly enhanced electromagnetic fields can drive highly nonlinear phenomena, like high-harmonic generation (HHG) [15, 16]. An essential aspect in many of these techniques is the capability of a controlled waveguiding of light including the concentration of electromagnetic energy and the comprehensive knowledge of its conversion pathways into other types of matter excitations (e.g., electron-hole pairs or phonons).

[1] "Ultrafast" refers to the time interval $\sim 10^{-18} - 10^{-12}$ s including the attosecond ($1\,\text{as} = 10^{-18}$ s), femtosecond ($1\,\text{fs} = 10^{-15}$ s), and picosecond ($1\,\text{ps} = 10^{-12}$ s) range.

Strongly linked to these endeavors is the rapidly developing field of *nanoplasmonics* [17, 18], launched by advances in nanofabrication techniques and broadband radiation sources [19, 20]. In nanoplasmonics, light interacts with electrons in the surface of a *nanostructure* (mostly made of metals) with typical dimensions ranging from the nanometer ($1\,\mathrm{nm} = 10^{-9}\,\mathrm{m}$) to micrometer ($1\,\mu\mathrm{m} = 10^{-6}\,\mathrm{m}$) scale. Plasmonic nanostructures feature a spatial concentration of optical waves beyond the diffraction limit [21, 22]. Specifically, the coherent coupling of light to collectively oscillating electrons results in characteristic *electromagnetic wave modes*, which are bound to the interface between the object and its environment (e.g., vacuum) [23]. Such a mode is called surface plasma wave or *surface plasmon* (SP) – referring to the analogue free charge motion in a plasma [24]. The remarkable property of this interaction is the capability to guide and enhance an SP near-field that is accompanied by a concentration of its electromagnetic energy to nanoscale volumes [17, 22].

The main objectives of nanoplasmonics are the understanding of the spatiotemporal evolution of SPs on their intrinsic length (nano- to micrometers) and time (femto- to picoseconds) scales as well as the development of nanostructure designs that have customized functionalities including SP excitation, SP waveguiding, and sub-wavelength light confinement [25–29]. As a consequence of the persistent miniaturization process, highly nonlinear and quantum effects play a growing role in these objectives [16, 30–33].

In this context, a metallic cone structure with an apex of a few nanometer in radius (*nanotip*) features an essential and multifunctional model system. In the tip structure, two basic manifestations of SP modes exist – both are accompanied by a strong near-field enhancement and energy concentration at the tip end (*hotspot*). On the one hand, the shaft is an effective waveguide for a *propagating* SP mode that is gradually confined when approaching the apex (*nanofocusing*), whereas, on the other hand, the nanometric apex provides a direct *localized* plasmon mode [34–36].

Although the excitation, evolution and relaxation of surface plasmons in nanostructures – and particular in nanotips – have been investigated and applied for several years, a comprehensive and in-depth understanding of the underlying physical processes has yet not been established. Experimental and theoretical challenges arise, for instance, from the complexity of SP dynamics (rapid dephasing/decay, many-body and multiscale description), and the inherent sensitivity on the specific (atomistic) structure and its environment [31, 37, 38].

This thesis advances the knowledge of surface plasmon excitations in cone-like nanostructures by investigating gold nanotips regarding three relevant aspects. Initially, we analyze and explain waveguiding (nanofocusing) of surface plasmons propagating towards the tip end. Subsequently, the process of nonlinear electron emission from the apex by interaction with nanofocused SPs is investigated. And finally, we explore the plasmon-mediated electron transport in a nanometric tunnel gap between a tip and a flat sample surface.

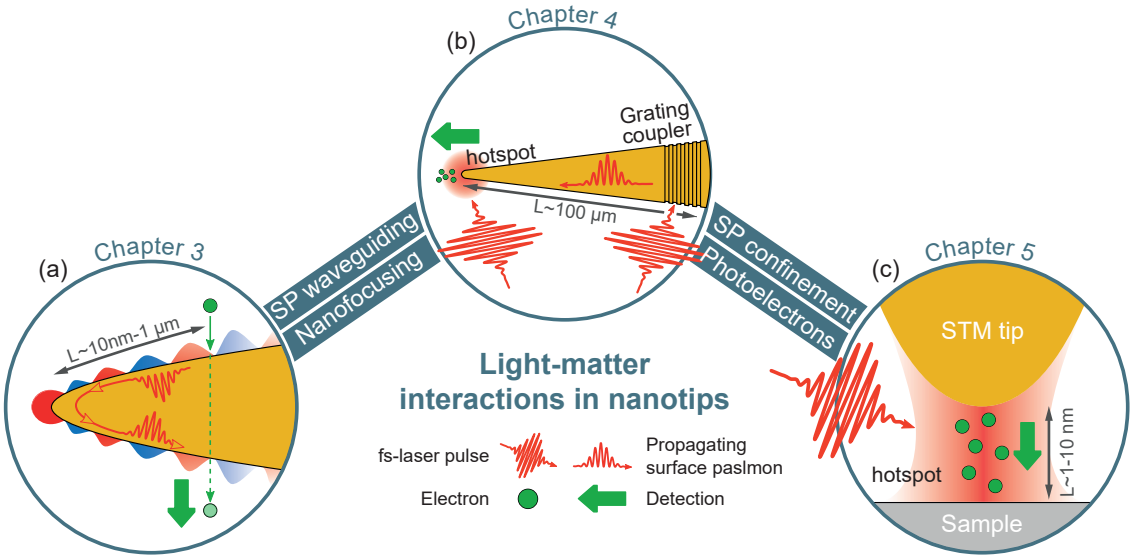

Fig. 1.1: Sketches of the three implemented experiments based on surface plasmon (SP) waveguiding/nanofocusing and localization/hotspot. (a) Mapping of SP modes resulting from the waveguiding properties of a gold nanotip. (b) Demonstration of an effective electron gun remotely driven by SPs that are launched with a grating coupler. (c) Near-field-driven photocurrents in the tunnel gap of a scanning tunneling microscope. The quantity L denotes the typical length scale on which the respective experiment in operating.

Figure 1.1 schematically illustrates the three conceptually different experiments operated on length scales covering a range from less than a nanometer to several tens of micrometer. The first aspect we address is the capability of metal tips to waveguide and localize surface plasmons. SP nanofocusing has been exploited in novel types of scanning probe techniques, such as ultrafast apertureless near-field scanning optical microscopy (A-NSOM) [39, 40] and tip-enhanced Raman spectroscopy (TERS) [41, 42]. A-NSOM features optical, super-resolved imaging of surfaces on a $\lesssim 10$ nm length scale [43–46], whereas TERS can provide spectral fingerprints of single molecules by detecting frequency shifts in the emission spectra [47–49]. Moreover, nanofocusing improves the achievable magnification and time resolution in femtosecond point-projection microscopy (fs-PPM) [50–52]. However, the spatial mode distribution and the SP propagation behavior at the apex are yet not understood.

In our experiment, we use an transmission electron microscope (TEM) to excite and spatially map SPs in free-standing gold nanotips on a $\sim 10\,\text{nm} - 1\,\mu\text{m}$ scale (see the characteristic length scale L in Fig. 1.1(a)). The simultaneous detection of electron energy loss spectra (EELS) in combination with finite-element and semianalytical modeling explains the complex superposition of different SP modes. Most importantly, we find the SPs reaching the apex to be back-reflected with a nearly 100% efficiency.

The second aspect of this work comprises photoelectrons emitted by plasmons. In the quickly developing field of electron-beam instruments, the release of ultrashort electron pulses from tip apexes by fs-laser transients allows for an observation of electron and lattice dynamics on a femtosecond to picosecond timescale in ultrafast transmission electron

microscopy (UTEM) [53, 54], ultrafast low-energy electron diffraction (ULEED) [55, 56], and fs-PPM [52]. Propagating and nanofocusing SPs may provide an efficient electron gun featuring new degrees of freedom by electron wave front tailoring [12].

We investigate SP-driven multiphoton photoemission from gold nanotips induced by grating couplers several ten micrometers away from the apex (see L in Fig. 1.1(b)). The structures are inserted into a modified field emitter assembly fully compatible with state-of-the-art UTEMs. This allows for a precise emission site-selectivity and control of the lateral beam spread. Grating-coupled SPs demonstrate a higher electron yield compared to direct apex illumination.

In our final experiment, we apply the nanometric field localization at the apex of a nanotip in a scanning tunneling microscope (STM). STM features sub-nanometer resolved surface mapping and spectroscopy, as well as controlled manipulation of individual atomistic species [57–59]. The ultimate combination of STM with a pulsed laser beam focused into the tunnel gap provides ultrafast time-resolved STM and nonlinear excitation setups (fs-STM) [60–62]. However, thermal instabilities due to tip expansion have prevented a regular application of fs-STM as they require elaborated and expensive illumination schemes [60, 63, 64].

We establish thermally stable STM operation under fs-laser illumination of the gap between a gold nanotip and a metal surface. The optical excitation results in the generation of photoelectrons with a specific dependency on the tip-sample distance (see Fig. 1.1(c)). We use an electron transport and coupled dipole model to explain the mechanisms involved in the photocurrent and identify different parameters controlling the photo-driven transfer. Importantly, the roles of surface plasmons excited in the tunnel gap and higher-energy electron channels are clarified. Topographies with nanometer precision evidence that the photoelectrons can be used in a reliable STM mapping mode.

Outline

Chapter 2 discusses the key concepts of light-matter interactions relevant in this thesis. The two general types of a localized and a propagating SP mode are exemplary outlined by a spherical particle and a flat interface including their capability to localize and enhance the plasmon near-field (sec. 2.1). In addition, a general picture of the two mechanisms to excite propagating surface plasmons (fast electrons and grating couplers) used in this thesis is presented. Subsequently, SP relaxation processes (sec. 2.2) and photo-driven electron emission based on a Sommerfeld model (sec. 2.3) are outlined. The chapter is concluded by a brief summary of the nanostructure preparation applied to fabricate the used tips (sec. 2.4).

In chap. 3, plasmon propagation along nanotip surfaces is analyzed. We start with a comprehensive introduction to SP waveguiding and nanofocusing with metal tips (sec. 3.1). The basics of EELS instrumentation used to map SP propagation are briefly described as well (sec. 3.2). The main experimental and theoretical results on the basis of the EELS measurements are discussed in sec. 3.3 representing our study published in Ref. [65] with the title "Real-space imaging of nanotip plasmons using electron energy loss spectroscopy". The chapter is concluded in sec. 3.4 by a comparative discussion of related literature in the light of our semianalytical model published in Ref. [66].

Chapter 4 presents the feasibility of an electron gun assembly that is driven by nanofocusing surface plasmons. The first section 4.1 provides a description of the setup established to measure photoelectron emission. Subsequently, we demonstrate the effective photoemission from gold nanotips controlled via electrostatic fields in sec. 4.2 and published in Ref. [67] with the title "An ultrafast nanotip electron gun triggered by grating-coupled surface plasmons".

In chap. 5, the realization of fs-STM is presented and laser-mediated electron transport in the tunnel contact is discussed. We start with two general processes that govern the currents emerging in an STM combined with fs-illumination, namely the formation of a plasmon near-field in the gap (sec. 5.1) and quantum tunneling transport (sec. 5.2). Both physical pictures are applied in sec. 5.3 to identify photocurrent channels and their transfer mechanisms. Our results have been published in Ref. [68] with the title "Controlling photocurrent channels in scanning tunneling microscopy". The final section 5.4 presents technical information on the challenging combination of a fs-laser source with an STM.

Finally, this thesis is concluded in chap. 6 with a summary of the major results found in our experiments and analysis. Relevant aspects from the literature with respect to the presented studies are discussed as well. Additionally, potential experimental schemes that may provide further insights are outlined.

The section Author contributions on page 117 lists the specific author's contributions to the three peer-reviewed publications reprinted in the secs. 3.3, 4.2, and 5.3.

CHAPTER 2

Light-matter interaction in metal nanostructures

Photons or electrons incident on a substance (e.g., solid or molecule) provide an immensely broad range of possible excitation pathways depending on their initial energy, momentum, and – in the case of photons – polarization state [7, 8, 69, 70]. This substantial complexity of optical interactions is further increased when considering *nanostructures* (i.e., objects with micro- or nanometer dimensions), since they exhibit fascinating phenomena enabled by their nanoscale geometry [24, 71–73]. Figure 2.1 presents a brief summary of fundamental excitations that can be driven in a nanostructure, which result in different scattering or emission channels.

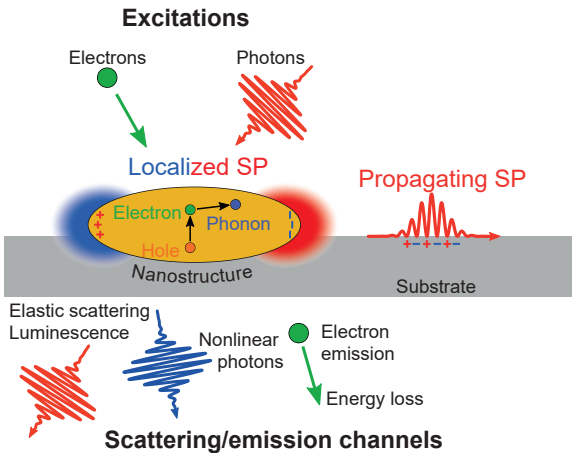

Fig. 2.1: Schematic illustration of the most fundamental excitations of a nanostructure. Incident electrons or photons can transfer energy and momentum via a rich variety of pathways to the constituents of the material (electrons and ions) and its quasiparticles (holes, phonons, plasmons, etc.). In experimental solid state physics, the resulting scattering and emission channels, e.g., elastically scattered photons, luminescence, nonlinear photon generation, electron emission, or electron energy loss are the observables carrying the fingerprint of the respective interaction. In this thesis, we focus on localized and propagating surface plasmons (SPs).

A general classification of the diverse physical interactions can be made using the number of involved particles in the material (single-particle vs. collective excitations), the degree of coherence between the incident field and the polarization induced in the material, the locality of the excitation, the involved energy levels (valence vs. core electron excitations), and the relevant (quasi)-particles (e.g., electrons, holes, plasmons, phonons, spins) [69, 74].

This thesis focuses on the collective oscillation of conduction band electrons in the near-infrared to visible wavelength regime ($\sim 0.5 - 3\,\mathrm{eV}$) and its nonlinear scattering mechanisms. Specifically, light-driven electron emission (transport) from metal tip nanostructures and energy loss through electron-metal interactions are the essential phenomena discussed here. The interaction of the photons and the electrons with the sample is fully described in the framework of the macroscopic Maxwell equations: A space-time-dependent incident field $\mathbf{E}(\mathbf{r}, t)$ induces a polarization in the specimen $\mathbf{P}(\mathbf{r}, t)$ including the fields of the collective electron oscillations. Typically, the calculations are done in frequency-space, where the polarization $\mathbf{P}(\mathbf{r}, \omega) \propto \varepsilon(\omega)\mathbf{E}(\mathbf{r}, \omega)$ directly follows from the complex-valued dielectric function (permittivity) $\varepsilon(\omega)$ that incorporates the optical response of the material[1] [24, 73, 74]. Explicit analytical solutions only exist for simple structures, e.g., spheres, planar surfaces or cylinders; most of the nanostructures must be treated by semi-analytical or numerical approaches [72]. Quantum effects must be included in the optical response for nanostructures with characteristic length scales $\lesssim 1\,\mathrm{nm}$ [71]. Although a strict quantum theoretical treatment is beyond the scope of this thesis, we make some important adaptions, for example, by using the Sommerfeld theory that models a metal as an electron gas confined to the structure volume with a state population given by an occupation function. In thermodynamical equilibrium, this is the Fermi-Dirac distribution [8, 75].

2.1 Collective electron oscillations: plasmon modes

Electromagnetic fields or charged particles can interact with metals or doped semiconductors by displacing the conduction electrons (electron gas) out of their equilibrium positions. This may result in a collective oscillatory motion of the electrons (plasma oscillation). Plasmonic modes exist in two general classes of longitudinal bulk oscillations and transversal surface plasma (SP) oscillations [38, 69, 73]. The first obey a nearly flat dispersion relation $\omega = \omega_p$ with the plasma frequency ω_p ($\sim 9\,\mathrm{eV}$ for gold) and can only be excited by charge particle impact [69]. On the contrary, SP oscillations are excitable by light and exist as transverse surface waves at interfaces of two environments (materials) with one having a negative and the other one having a positive permittivity for a given frequency (e.g., near-infrared to visible energies for gold-vacuum interfaces). They exhibit a coherent coupling to a surface bound electromagnetic wave giving rise to a *field enhancement* and a *field confinement* effect

[1] An equivalent formalism is given by the current density $\mathbf{J}$ with the complex frequency-dependent conductivity [69, 73]. We assume isotropic materials, in which the dielectric function is a scalar.

(see below). For sufficiently small samples (nanoparticles), SP oscillations can be localized and in the case of extended structures the modes may propagate along the interface [24, 76]. Both types play an important role in this work and are discussed in the following sec. 2.1.1 and sec. 2.1.2.

In the framework of quantum mechanics, the field of a plasma oscillation is quantized providing the formalism of the bosonic quasi-particle *plasmon* [31]. The mutual interplay of a surface plasmon and a light field bound to the interface is called a polariton[2]. However, in order to distinguish the two manifestations of a *localized* and *propagating* plasmonic mode, we use localized surface plasmons (LSP) and surface plasmon polaritons (SPP), respectively [76–78]. In this quantum picture, a single photon of energy $\hbar\omega$ is annihilated in the light field and a bosonic plasmon polariton of the same energy is created in the plasma field [31]. Although, we apply the classical Maxwell equations with a local dielectric function to include the material's optical properties we use the "plasmon" terms (LSP and SPP) throughout this thesis.

2.1.1 Localized surface plasmons of a spherical tip apex

Nanotips that are exposed to an electromagnetic field exhibits the remarkable properties of field enhancement and field localization owing to the surface plasmon excitations in the apex. In the following, we learn about these basic concepts by modeling the apex as a spherical nanoparticle of radius R_T, as illustrated in Fig. 2.2(a). The sphere has the frequency-dependent permittivity $\varepsilon_t(\omega)$ and is surrounded by a dielectric medium with a constant permittivity ε_d [73]. For simplicity, we assume an incoming plane wave $\mathbf{E}_0(t)$ polarized in the z-direction. The free electrons of the particle (conduction band electrons), follow $\mathbf{E}_0(t)$ and the negatively charged carriers are separated from the positively charged lattice ions, i.e., the polarization $\mathbf{P}(t)$ is induced into the sphere. This results in a surface charge density $\sigma(t)$ which is accompanied by a restoring force. In frequency-space, a resonance characteristic depending on the structure size and optical material properties is found. The interplay of the time-varying charge separation and its accompanying electromagnetic near-field is the *localized surface plasmon*[3] (LSP) polariton [73, 79–81].

Within the quasi-static Rayleigh approximation (tip radius R_T is much smaller than the light wavelength $\lambda = 2\pi c/\omega$) the field is assumed to be spatially constant across the particle and oscillates in time, $\mathbf{E}_0 \exp(-i\omega t)$. Solving the Laplace equation ($\mathbf{E} = -\nabla \cdot V(\mathbf{r})$) with Legendre polynomials, the potential $V(\mathbf{r})$ is found. It leads to the field [73]

$$\mathbf{E}^{\text{out}}(\mathbf{r},t) = \mathbf{E}_0 e^{-i\omega t} + \mathbf{E}_{\text{nf}}(\mathbf{r},t) = \mathbf{E}_0 e^{-i\omega t} + \frac{3\mathbf{n}(\mathbf{n}\cdot\mathbf{p}) - \mathbf{p}}{4\pi\varepsilon_0\varepsilon_d}\frac{1}{r^3}, \tag{2.1}$$

[2] There exist different forms of polaritons, classified according to their underlying matter excitation (e.g., phonon-, plasmon-, or exciton-polaritons) [69].
[3] In the literature, it is also named LSP resonance (LSPR) to emphasize the resonant character.

outside the particle (radial distance $r = |\mathbf{r}|$ and unit vector $\mathbf{n} = \mathbf{r}/r$ in the direction of $\mathbf{r}$). $\mathbf{E}^{\text{out}}$ is the superposition of the incident light field (first term) and the near-field of a dipole $\mathbf{E}_{\text{nf}}$ located at the particle center (second term). The dipole moment $\mathbf{p}(t) = \varepsilon_0 \varepsilon_d \alpha_\omega \mathbf{E}_0 e^{-i\omega t}$, is proportional to $\mathbf{E}_0$ with the polarizability

$$\alpha_\omega = 4\pi R_T^3 \frac{\varepsilon_t - \varepsilon_d}{\varepsilon_t + 2\varepsilon_d}. \tag{2.2}$$

An LSP is linked to the near-field enhancement $F = |\mathbf{E}^{\text{out}}|/|\mathbf{E}_0| > 1$ for a small denominator in Eq. 2.2 ($\varepsilon_t \to -2\varepsilon_d$), also known as the Fröhlich condition [73]. Figure 2.2(b) presents the calculated enhancement F in the xz-plane for a gold sphere in vacuum with a radius of 10 nm and illumination with $\lambda = 800$ nm ($\hbar\omega = 1.55$ eV). Two regions of enhanced field strength ($F > 1$, green to red) close to the surface are observable. The distinct direction of the field pattern (along the vertical axis) is governed by the light polarization. Figure 2.2(c) shows the line profile of F along the central vertical dotted line in (b). This simple example represents the main concept of *plasmonic hotspots*: The field enhancement ($F \approx 3.3$ in the example) at the particle's surface and the localization (measured by the full-width at half-maximum of F, here: 6 nm). Hence, the field is strongly confined to a sub-wavelength scale of the order of R_T.

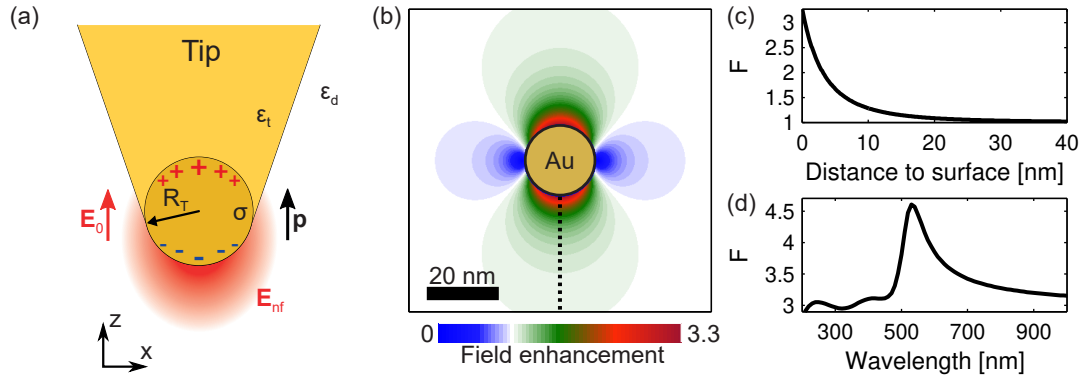

Fig. 2.2: Tip apex modeled as a sphere and the resulting LSP field distribution. (a) Schematic illustration of a tip apex approximated by a sphere of radius R_T and permittivity $\varepsilon_t(\omega)$ embedded in a dielectric medium (ε_d). A homogenous field, $\mathbf{E}_0 \exp(-i\omega t)$, oscillating with ω and magnitude $\mathbf{E}_0$ causes a time-varying surface charge distribution $\sigma(t)$ giving rise to a polarization with dipole moment $\mathbf{p}$. This leads to the near-field $\mathbf{E}_{\text{nf}}$ of the LSP that is calculated for a vacuum environment ($\varepsilon_d = 1$) with the permittivity of gold ($\varepsilon_t \approx -24 + 1i$) taken from Ref. [82] at $\lambda = 800$ nm (1.55 eV). (b) Field enhancement $F = |\mathbf{E}^{\text{out}}|/|\mathbf{E}_0|$ of a gold sphere with $R_T = 10$ nm mapped in the xz-plane and calculated with Eq. 2.1. (c) Profile of the field enhancement normal to the sphere surface along the dashed line in (b). The maximum enhancement of $F \approx 3.3$ is found at the sphere surface with a near-field decay to zero ($F = 1$) after ~ 25 nm. (d) The wavelength dependency of F evaluated at its maximum. A distinct resonance is found at 530 nm with $F \approx 4.6$, whereas for the majority of the displayed wavelength range $F > 3$ applies.

The analysis of Eq. 2.1 and Eq. 2.2 reveals a general rule for the existence of enhanced near-fields. The Fröhlich condition requires a negative permittivity ($\varepsilon_t < 0$) that compensates the positive ε_d of the surrounding dielectric. Besides, the imaginary component must be as small as possible ($\text{Im}(\varepsilon_t) \ll 1$) to maximize the field enhancement. In other words,

the damping of electromagnetic modes because of absorption in the material must be small [80]. This leads to a resonant characteristic due to the wavelength dependency of $\varepsilon_t(\omega)$, as presented in Fig. 2.2(d). Both requirements are sufficiently fulfilled in the near-infrared and visible wavelength regime for, e.g., copper, gold and silver [83]. Note that Eq. 2.1 describes only the near-field of the oscillating dipole; from a strict calculation the total field can be derived and the prominent dipolar electromagnetic radiation follows [84]. We briefly discuss absorption in the material and radiation to the far-field as limiting factors of the lifetime and field enhancement of excited plasmons in sec. 2.2.

The applied quasi-static approximation stays valid for nanoparticles under illumination with visible light up to sizes of $\sim 100\,\mathrm{nm}$ [73], which includes apex radii between 10 nm and 20 nm relevant in our experiments. Generally, the resonance structure and field enhancement sensitively depends on the specific geometry and material [85]. On the theoretical side, more sophisticated tip models have been studied that include retardation effects and modifications of the resonance structure for elongated spheroids [80, 85–87] based on Mie theory [88]. Besides, there is a variety of studies based on (semi)-analytical and numerical methods that explore the field distribution and resonance behavior of realistic tip structures by varying material, excitation scheme and geometry parameters [87, 89–101]. Thereby, field enhancement factors on the order of $10 \leq F \leq 100$ are commonly found exceeding the values of the sphere dipole model because of a geometry induced charge accumulation at the tip's end [91, 100, 102]. Experimental investigations on gold tips, however, have demonstrated field enhancements between 4 and 14 that are ranging at the lower boundary of the theoretical approaches [67, 103–106]. Here, F is determined from linear and nonlinear photon and electron emission measurements under similar excitation conditions. Most importantly, F is maximized for p-polarized excitation fields (polarization along the tip's symmetry axis), while s-polarization strongly suppresses the enhancement [85, 90, 91, 103, 104].

2.1.2 Propagating surface plasmons of planar interfaces

In the case of spatially extended structures, it is possible to excite propagating plasmon excitations [25, 76]. Figure 2.3(a) exemplarily illustrates such a mode for a planar interface between a metal and a dielectric semi-infinite half space. The collective oscillation of the surface charge density $\sigma(t)$ couples to an electromagnetic near-field in the dielectric and in the metal. This mutual interaction of photons with plasmons results in a mode bound to and propagating along the interface – this is the *surface plasmon polariton* (SPP) [24, 25, 72]. The associated field distribution obeys a transverse-magnetic (TM) mode with finite electric and magnetic field components $(E_x, E_z, H_y) \propto \exp(iqx - q_j z)$ in the tip ($j = t$) and vacuum ($j = d$). A straight forward calculation based on the tangential continuity condition

at the interface (cf. Ref. [73]) provides the SPP dispersion relation,

$$q(\omega) = \frac{\omega}{c}\sqrt{\frac{\varepsilon_t(\omega)\varepsilon_d}{\varepsilon_t(\omega)+\varepsilon_d}} \qquad \text{and} \qquad q_j(\omega) = \pm\sqrt{\left(\frac{\omega}{c}\right)^2 \varepsilon_j - q(\omega)^2} \tag{2.3}$$

with the SPP wavenumber $q(\omega)$ along the surface and the field's evanescent decay into the tip ($L_{\text{tip}} = 1/|2q_t|$) and into the vacuum ($L_{\text{vac}} = 1/|2q_d|$). SPP excitation is found for real wavenumbers under the condition $\text{Re}(\varepsilon_t) < \varepsilon_d$ (agreeing with the Fröhlich condition in the last section), which leads to values $q(\omega) > \omega/c$ in the relevant energy regime $1\,\text{eV} < \hbar\omega < 3\,\text{eV}$. Consequently, there is no simultaneous energy and momentum conservation between freely propagating light with wave vectors $|\mathbf{k}| = k = \omega/c$ and SPP modes at a planar interface. Figure 2.3(b) demonstrates this fact by comparing the real part of the SPP dispersion $\hbar\omega(q)$ (solid red line) calculated with Eq. 2.3 for a Drude metal and the dispersion of light in vacuum for grazing incidence $\hbar\omega = ck$ (dotted line). For all energies, the SPP dispersion is on the right side of the light line and special techniques delivering additional momentum Δk must be applied for the purpose of SPP excitation[4] (inset in Fig. 2.3(b)) [24, 73].

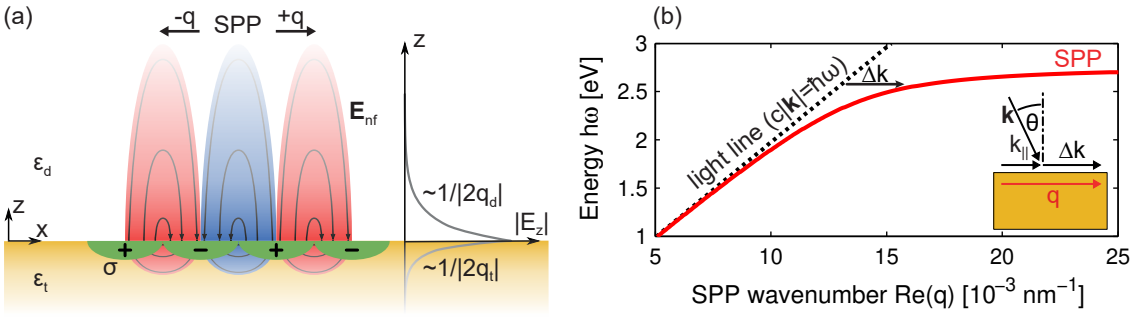

Fig. 2.3: Surface plasmon polaritons (SPPs) at planar interfaces. (a) A schematic illustration of the field distribution $\mathbf{E}_{\text{nf}}$ of an SPP and the associated surface charge density σ (green areas) for the interface between a metal and dielectric with permittivities ε_t and ε_d, respectively. The surface wave propagates bound to the interface in $\pm x$-direction with respect to a complex dispersion relation $\pm q(\omega)$ and decays evanescently inside ($L_{\text{tip}} = 1/|2q_t|$) and outside ($L_{\text{vac}} = 1/|2q_d|$) the metal. (b) SPP dispersion relation (solid red line) for a Drude metal ($\varepsilon_t(\omega) = \varepsilon_\infty - \omega_p^2/\omega^2$) with $\omega_p = 9\,\text{eV}$ and $\varepsilon_\infty = 9.8$ [80] calculated with Eq. 2.3. There is no intersect with the light line (dashed line). Hence, a far-field with an in-plane momentum component $k_\parallel = |\mathbf{k}|\sin\theta$ ($|\mathbf{k}| = \omega/c$) can only couple to SPPs if an additional momentum Δk is provided to fulfill energy and momentum conservation, $q = k_\parallel + \Delta k$ (inset).

In order to realize SPP launching different implementations have been developed to fulfill the phase matching condition, $q(\omega) = (\omega/c)\sin\theta + \Delta k$, among which are prism geometries [107, 108], scanning probes [109, 110], and topological protrusions (surface defects) [24, 111, 112]. In our experiments, we use fast electrons and periodic surface structures (grating couplers) to launch SPPs.

[4] A light wave vector $\mathbf{k}$ under an angle of incidence $0 \leq \theta < 90°$ does not change this situation, since the in-plane wave vector component, $k_\parallel = (\omega/c)\sin\theta$, is smaller than ω/c for all values of θ.

2.1.3 SPP excitation via charged particles

The field of nanoplasmonics strongly benefits from the possibility of electromagnetic mode (in particular SPP) excitation in matter by fast electrons transmitting through or closely passing the sample under investigation [74, 113–118]. In their pioneering works Ritchie [119], Powell et al. [120], and Stern et al. [121] identified the excitation of volume and surface plasmon resonances (~ 10 eV) to be responsible for the found electron energy loss (EEL) ΔE when the electrons transmit through thin metallic films. Modern EEL spectroscopy (EELS) experiments are performed in transmission electron microscopes with ~ 10 meV spectral resolution [116] and are operated in a scanning mode (STEM) allowing to spatially map plasmon mode distributions in the mid-infrared domain with nanometer precision [122].

From the sample's viewpoint, the electron moving with a velocity $\mathbf{v}$ is accompanied by a time varying evanescent field $\mathbf{E}^{\mathrm{e}^-}(\mathbf{r}, t)$ which induces a polarization $\mathbf{E}^{\mathrm{ind}}$ in the material. Under certain conditions (discussed below), this electron-matter interaction leads to the excitation of electromagnetic modes of the electron gas including SPPs. Thus, the field $\mathbf{E}^{\mathrm{e}^-}$ associated with the electron can be considered as a light source with an energy-momentum relation $\hbar\omega(\mathbf{k}_e)$. The spectral components $\mathbf{E}^{\mathrm{e}^-}(\mathbf{r}, \omega)$ determine the energy levels accessible for this excitation mechanism. Specifically, the spectral amplitude and width of $\mathbf{E}^{\mathrm{e}^-}$ scale with $\mathbf{v}$ – demanding electron kinetic energies of a few tens of keV for investigations of plasmons in the eV regime [117].

Considering energy-momentum conservation, the transfer of energy $\hbar\omega$ and momentum $\mathbf{k}_e$ from $\mathbf{E}^{\mathrm{e}^-}$ to an electromagnetic mode (induced polarization) reduces the electron energy E_e to $(E_e - \hbar\omega) = \sqrt{|\mathbf{p}_e - \hbar\mathbf{k}_e|^2 c^2 + m_e c^4}$, with m_e being the rest mass and $\mathbf{p}_e$ the momentum of the electron [123]. Since we deal with relative low energy and momentum transfers compared to E_e and $\mathbf{p}_e$, we can use the non-recoil approximation (NRA) ($E_e \gg \hbar\omega \approx \hbar c|\mathbf{k}_e|$) leading to the linear dispersion relation [74, 123]

$$\omega = \mathbf{k}_e \cdot \mathbf{v} = k_e v_e \cos(\phi).$$

Here ϕ denotes the angle between $\mathbf{k}_e$ and $\mathbf{v}$. Figure 2.4(a) shows the dispersion of the electron associated field $\omega = k_e v_e$ ($|\mathbf{k}_e| = k_e, |\mathbf{v}| = v_e$) for $\phi = 0°$ as a green line and transferable energies with $0° < \phi \leq 90°$ are represented by the gray shaded area. When the electron encounters a metallic interface a coupling to surface plasmon polaritons is possible due to energy-momentum conservation, as demonstrated by the overlapping section of the schematic SPP dispersion $q(\omega)$ (red line in Fig. 2.4(a)) with $\omega = \mathbf{k}_e\mathbf{v}$ [74]. The intersection given by $q(\omega_t) = \omega_t / v_e = k_e$ defines the energy threshold $\hbar\omega_t$ below which coupling to the plasmonic modes is prevented because of momentum mismatch.

Essentially, the accessible energy range and the spatial mapping capability of the sample's electromagnetic modes depend on the spectral composition and spatial extent of $\mathbf{E}^{\mathrm{e}^-}$ [117]. Figure 2.4(b) presents the electric components $E_r^{e^-}$ and $E_z^{e^-}$ calculated in cylindri-

cal coordinates by treating the electron as a point charge propagating along a line trajectory in z-direction (kinetic energy $eU = 200\,\mathrm{keV}$) [124]. The field is given at the position $(z, r) = (0, 10\,\mathrm{nm})$ (solid black and red line), where both field components are temporally located within 0.05 fs to 0.1 fs representing an ultrashort burst of radiation at the reference point. The field components act differently on a probe charge positioned at r: the force linked to $E_r^{e^-}$ (black line) points in one direction for the entire transient, while the force in z-direction (red line) changes its sign at $t = 0$. Moreover, the r-component has a four times higher peak field strength. Increasing the radial distance r to 40 nm raises the pulse duration by a factor of four and decreases the maximal amplitude by a factor of 16, as shown by the second transient (dashed lines in Fig. 2.4(b)).

The evanescent character of $\mathbf{E}^{e^-}$, i.e., the spatial confinement to the source, is presented in Fig. 2.4(c) as the time-integrated total intensity $\propto \int \mathrm{d}t(|E_r^{e^-}|^2 + |E_z^{e^-}|^2)$. The reduction by six orders of magnitude over a distance change from $r = 1\,\mathrm{nm}$ to $r = 100\,\mathrm{nm}$ from the electron demonstrates the field localization to the electron trajectory[5]. This property is crucial to the capability of SPP mode mapping with nanometer precision, since the swift electron acts as an effective local probe [117]. The spectral content (Fourier transform) of the transient field (inset of Fig. 2.4(c)) is exemplary shown for $r = 10\,\mathrm{nm}$ (solid line) as the energy spectrum of the total intensity normalized to its maximum. The broad energy range ($\sim 20\,\mathrm{eV}$ at half-maximum) allows for the excitation of modes with resonance energies in the extreme ultraviolet domain.

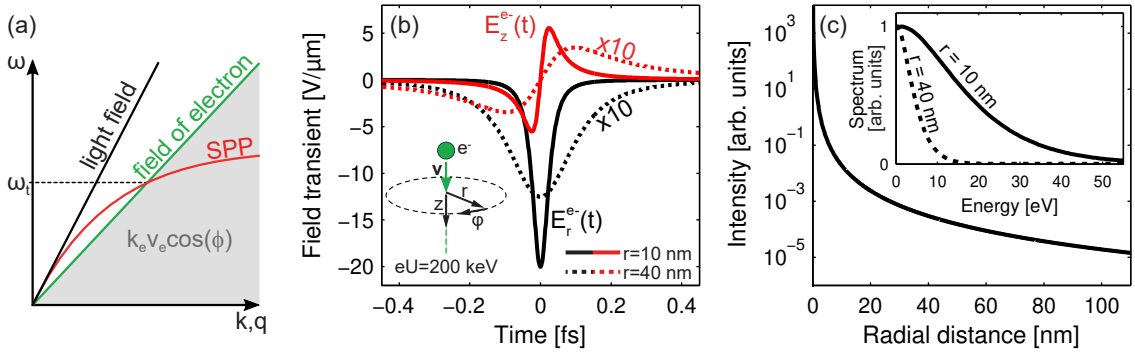

Fig. 2.4: Fast electrons as a light source for SPP excitation. (a) Schematic illustration of the dispersion relation of the electron associated field (green line) compared to light in vacuum (black line) and SPP dispersion (red line). The electron can excite electromagnetic modes by momentum and energy conservation above a certain threshold $q(\omega_t)$. (b) The electric field of an electron with 200 keV kinetic energy given by the radial (black lines) and longitudinal (red lines) components. Presented are the transients for two positions $r = 10\,\mathrm{nm}$ (solid lines) and $r = 40\,\mathrm{nm}$ (dashed lines) with respect to the electron position (cf. inset). (c) The time-integrated total intensity $\propto \int \mathrm{d}t(|E_r^{e^-}|^2 + |E_z^{e^-}|^2)$ as a function of radial distance r demonstrates the electron's local probe properties. An intensity decay by a factor of ~ 100 in the range $r = 10\,\mathrm{nm}$ to $r = 40\,\mathrm{nm}$ is observed. This is accompanied by a decrease of the spectral components of the fields: The bandwidth of the energy spectra normalized to their maxima (inset) decrease from 20 eV to 5 eV (measured by the half-value).

[5] For $r \to 0$, the intensity diverges due to the point-like character of the charge carrier. This singularity is removed in a proper quantum description based on a self-energy formalism [74, 124].

Despite the fact that we have not yet introduced a real sample to the description, the consideration of the energy-momentum relation and the time-varying field of a swift electron passing a probe charge conveys an instructive picture of the interaction of the electrons and electromagnetic modes. In conclusion, high-velocity point charges provide a broadband, ultrashort and local light source ideal to investigate electromagnetic modes with a dispersion relation outside the dispersion of light in vacuum.

2.1.4 SPP excitation via grating couplers

A periodic arrangement of surface defects with sub-wavelength dimensions can provide additional momentum Δk to overcome the momentum mismatch between far-field light and SPPs (cf. inset Fig. 2.3(b)) [111]. In our experiment, we use grating couplers (GCs) of several slits milled into the tip shaft by a focused ion beam (FIB) (see Fig. 2.8(b)). Light with the wave vector $\mathbf{k}$ illuminates a grating of periodicity p_g under an angle of incidence θ, as schematically illustrated in Fig. 2.5(a).

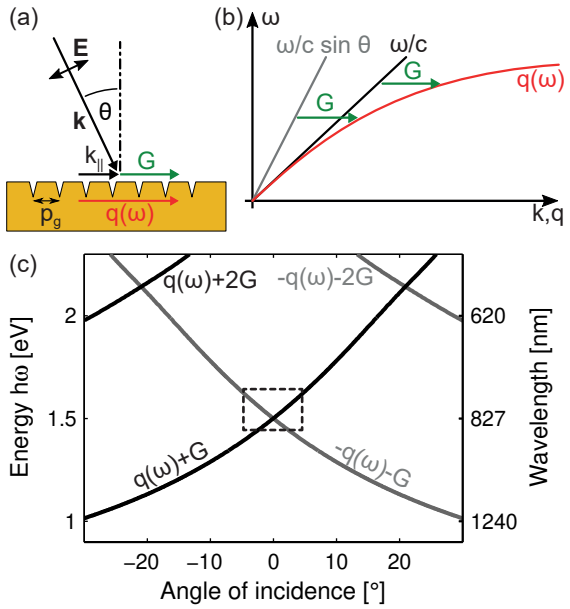

Fig. 2.5: SPP excitation via a grating coupler (GC). (a) Far-field light with wave vector $\mathbf{k}$ illuminates a GC with grating periodicity p_g under an angle of incidence θ with respect to the surface normal. The field $\mathbf{E}$ is polarized in the plane of incidence (p-polarization). Resonant SPP coupling occurs for a phase matching condition (cf. Eq. 2.4) which requires an equality between the SPP dispersion $q(\omega)$ (red arrow) and the sum of the scattering vector $\nu G = \nu 2\pi/p_g$ (green arrow) and the in-plane component $k_\parallel = \omega/c \sin\theta$ of the incident light (black arrow). (b) Schematic SPP dispersion relation (red line) and light lines for grazing incidence ($\theta = 90°$, black line) and $0° < \theta < 90°$ (gray line). Depending on the angle of incidence, momentum conservation is given for different energies/frequencies (illustrated by the first diffraction order with green arrows). (c) Plot of $\omega(\theta)$ calculated with the phase matching condition (Eq. 2.4) for an SPP dispersion of a flat gold surface (Eq. 2.3) and the diffraction orders $\nu = \pm 1$ and $\nu = \pm 2$. The parameter range of our experiment is indicated by the the dashed area.

The GC causes the light incident on the structure to be scattered into different diffraction orders given by the integer ν and grating vector $G = 2\pi/p_g$ (green arrow). An excitation of SPP waves occurs if the light field $\mathbf{E}$ has a polarization component perpendicular to the grating grooves (p-polarization) and if the phase matching condition (momentum conservation),

$$q(\omega) = k_\parallel(\omega) + \nu G = \frac{\omega}{c} \sin\theta + \nu \frac{2\pi}{p_g} \tag{2.4}$$

is fulfilled [23, 24, 125]. Here, $k_\parallel = |\mathbf{k}| \sin\theta = \omega/c \sin\theta$ is the in-plane component of the incident light wave vector. Figure 2.5(b) illustrates this relation with a schematic SPP dispersion (red line) for the scenarios of grazing incidence ($\theta = 90°$) (black line) and

$0° < \theta < 90°$ (gray line). Using Eq. 2.4, we find the parameters θ and ν to excite an SPP mode[6] for a given frequency ω and a grating period p_g.

Figure 2.5(c) shows the phase matching condition of Eq. 2.4 (in the form $\omega(\theta)$) for the SPP dispersion of a semi-infinite interface for the $\nu = \pm 1$ and $\nu = \pm 2$ diffraction orders. Here, $q(\omega)$ is calculated with Eq. 2.3 and the gold permittivity taken from Ref. [82]. Our experiment (chap. 4) is restricted to an angle of incidence close to perpendicular to the tip surface ($\theta \approx 0°$) with an excitation spectrum centered at 780 nm nm with ~ 120 nm spectral bandwidth (leading to an angle and energy region indicated by the dashed area in Fig. 2.5(c)). We roughly adjusted the grating periodicity to provide an sufficient SPP coupling for the $\nu = \pm 1$ resonance[7].

2.2 Relaxation mechanisms of surface plasmon excitations

Once a polarization including SP modes is induced, it relaxes over time either by *radiative* or *non-radiative* decay mechanisms. This limits the surface plasmon lifetime τ_{sp} and the achievable field enhancement [81, 130–132]. LSPs and SPPs are mostly affected by intrinsic non-radiative electron-hole pair, electron-electron, and electron-phonon excitations (non-radiative damping rate γ_{nr}). These are incorporated in the dielectric function of the material ($\gamma_{\mathrm{nr}} \propto \mathrm{Im}(\varepsilon_t)$) leading to the finite LSP resonance width observed in Fig. 2.2(d) and a spatially limited SPP propagation (cf. Fig. 3.3 in sec. 3.1) [80]. The SP decay mechanisms evolve on different time scales and the non-equilibrium dynamics can be viewed as a scattering cascade that is schematically shown in Fig. 2.6 [133]. On a timescale of $\lesssim 100$ fs the absorption of (multiple) photons from the SP field generates electron-hole pairs (Landau damping) resulting in a non-thermalized electron distribution [134]. If the number of absorbed photon energy quanta is sufficiently large multiphoton photoemission can occur (see below). During the subsequent 100 fs to 1 ps, electron-electron interactions (Auger transitions) lead to a quasi-equilibrated (hot electron) distribution characterized by an effective electron temperature T_e. This cools down on a $1 - 10$ ps timescale by electron-phonon coupling (Ohmic loss), that is much slower because of the higher inertia of crystal ions [133]. A two-temperature model assigning separate thermal conductivities and heat capacities to the electron and to the phonon system has been developed to treat the heat transfer [135]. Applying this formalism to pump-probe experiments on tungsten tips demonstrated electron peak temperatures of $T_e \approx 2000$ K (for pulse energies in the mJ regime) [136]. Finally, on the timescale of tens of picoseconds to several tens of nanoseconds, diffusion transports the heat into the bulk material [133].

In addition to these intrinsic damping mechanisms, also crystal imperfections (e.g., grain

[6] Varying the angle of incidence θ in spectrally resolved transmission or reflection measurements allows to map the SPP dispersion relation over a wide range of $q(\omega)$ [112, 126, 127].

[7] Similar experimental schemes with gratings on gold tips have demonstrated effective acceptance bandwidths (wavelength spectrum that is coupled by the GC) of $\sim 60 - 100$ nm [45, 128, 129].

boundaries), scattering at the structure surface, non-locality of the dielectric function, and quantum size effects can modify the damping rates [71, 134, 137, 138].

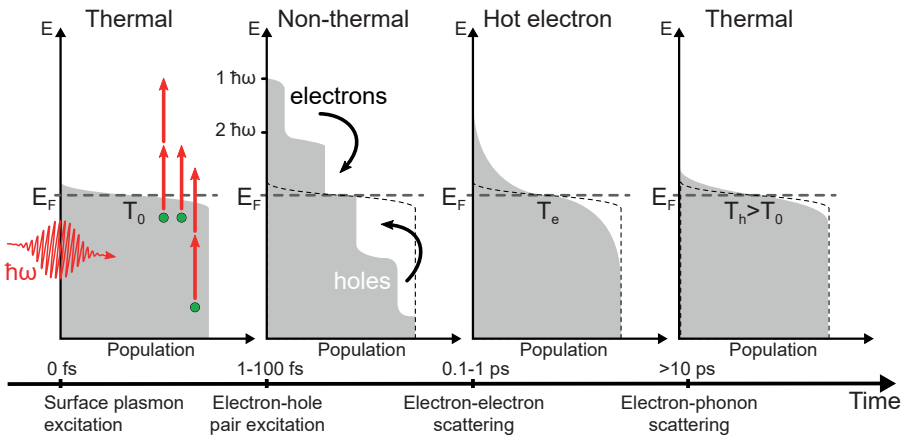

Fig. 2.6: Population dynamics followed by photon absorption. At time zero a light field with photon energies of $\hbar\omega$, e.g., an SP near-field, couples to the electronic system in thermodynamical equilibrium (with temperature T_0). On a timescale of $\sim$ 100 fs, single electrons absorb (multiple) photon energies (red arrows) which generates a highly non-thermal occupation of electron-hole pairs. Subsequently, the excited system evolves in a time of $\sim$ 100 fs-1 ps into a hot electron distribution by electron-electron scattering (black arrows). The resulting population is associated with an effective temperature $T_e \gg T_0$. This is followed by the coupling to the phonon system on a timescale of $\gtrsim$ 10 ps ending in an equilibrated state with a slightly higher temperature $T_h > T_0$. Finally, diffusion leads to dissipation (not shown). Adapted from Ref. [133].

SPPs at flat interfaces are bound modes, thus they do not decay through radiative processes [73]. On the contrary, LSPs of spherical particles emit photons to the far-field via dipole radiation with a cross-section proportional to R_T^6, while the intrinsic absorption cross-section scales with R_T^3 [80, 81, 85]. Because of this different dependencies, radiation plays a minor role for LSP decay of nanoparticles with $R_T \lesssim 20$ nm [139]. However, linear and nonlinear photon emission carries the fingerprints of the underlying relaxation pathways and is the central part of many spectroscopic and time-resolved optical experiments and applications. For example, interferometry experiments with the second harmonic generation from gold tip apexes have demonstrated an apex LSP lifetime of $\tau_{\mathrm{sp}} \approx 20$ fs – basically, limited by the above mentioned intrinsic damping mechanisms [140].

2.3 Light-driven electron emission

Complementary to photon-based analytical methods, optically driven electron emission from a sample is a powerful tool, which can provide fundamental insights into the electronic band structure and charge carrier dynamics in many different materials. Prominent experimental techniques making use of this are ultrafast angle-resolved photoemission spectroscopy (ARPES [141, 142]) and photoemission electron microscopy (PEEM [143–145]). Furthermore, electron pulses emitted through fs-laser excitation are used in gun assemblies in ultrafast electron microscopy (UTEM [54, 146, 147], fs-PPM [51, 52]) and ultrafast diffraction

experiments (ULEED [55, 56, 148]). This allows for time-resolved measurements in the femtosecond to picosecond-regime. In these examples, plasmonic near-fields generated at nanostructures play a crucial role, as they enhance and confine the electron current.

We discuss the basic concepts of electron transfer from a solid to vacuum based on the Sommerfeld model for metals (an electron gas moving in a one-dimensional potential well) [75, 149]. In thermodynamical equilibrium, the electrons populate the states with energies E up to the Fermi edge[8] E_F. This situation in schematically illustrated in the left panel of Fig. 2.7(a) (gray shaded area of the population f). At the sample surface the charge carriers face a potential barrier of an energy $E_{\mathrm{vac}} > E_F$ preventing the electrons from emitting into the vacuum. In other words, the electrons at E_F must gain at least the work function $\Phi = E_{\mathrm{vac}} - E_F$ to be released from the material. The potential transition from the solid to the vacuum can be approximated by an image potential (solid black line in the right panel of Fig. 2.7) originating from the self-induced polarization of an electron outside the sample that is described by the Coulomb interaction $V_{\mathrm{img}} \propto -e^2/4z$ of the electron with its induced image in the sample [84]. Two general strategies come into mind how a charge carrier can emit from the material (excluding a change of Φ). Either the electron is energetically elevated to states with $E > E_{\mathrm{vac}}$ (Figs. 2.7(a-c)) or the barrier "trapping" the electron is modified in such a way that the tunneling probability to the vacuum is significantly increased (Fig. 2.7(d)).

2.3.1 Multiphoton photoemission

The linear surface photoelectric effect is an important example of the former scenario that bases on the energy change of electrons – presented in Fig. 2.7(a). Here, an electron absorbs a photon energy $\hbar\omega > \Phi$ exceeding the work function and is transferred to the vacuum. The mechanism was discovered by Hertz in 1887 [1] and explained by Einstein in 1905 [2]. According to these groundbreaking studies, the absorption process involves a single light quantum determining the final kinetic energy of the electron $\hbar\omega - \Phi$ and the light intensity I_ω only determines the amount of emitted electrons (the current I). In particular, photons with $\hbar\omega < \Phi$ are not able to release electrons to the vacuum. As a matter of fact, this statement is restricted to surfaces that are exposed to small photon densities (linear optics).

For increased intensities, nonlinear optics must be applied. Here, an electron can absorb several photons, each of which has an energy smaller than the work function. However, the total energy of n absorbed photons may exceed the barrier ($n\hbar\omega > \Phi$) leading to *multiphoton photoemission* (MPPE) (Fig. 2.7(b)). This process involves $n-1$ real or virtual intermediate states that the electron traverses and the specific pathway depends on the actual band structure of the material [150–153]. In general, this mechanism requires intense light fields in order to provide n photons to be absorbed in a sufficiently small period of

[8] We assume a temperature T_0 much smaller compared to the Fermi temperature that attains values of several 10^4 K in metals [8].

time. Hence, the invention of the laser – seven decades after Hertz experiments on linear photoemission – was necessary to demonstrate two-photon absorption for the first time in 1961 [154]. Nowadays, ultrashort laser pulses and field enhancing nanostructures are utilized to drive highly nonlinear absorption processes [30, 149, 155].

Static heating or a transient elevation of the electron temperature is another way of electron transfer over the barrier (Fig. 2.7(c)). Here, the high-energy tail of an electron distribution following from the Fermi-Dirac distribution $f(E) = (\exp[(E-E_F)/k_B T_e]+1)^{-1}$ exceeds E_{vac} (Boltzmann constant k_B) [8]. In the case of static heating, this is called thermionic emission and it requires electron temperatures T_e of the order of a few thousands of Kelvin. Thus, only high-melting point materials (e.g., tungsten) can be used in hot-cathode guns in electron microscopy [156].

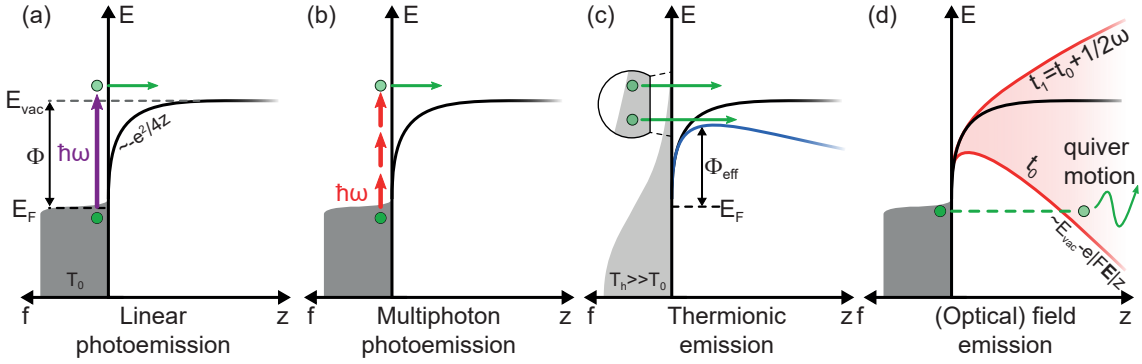

Fig. 2.7: Schematic illustration of electron transport pathways from a metal to the vacuum. The electron gas populates states in the metal represented by the Fermi-Dirac distribution $f(E)$ (gray shaded areas) for a temperature $T_0 \ll T_F$ (Fermi temperature T_F is of the order of 10^4 K). An image potential ($V_{\mathrm{img}} \propto -e^2/4z$) modifies the energy landscape outside the metal (black line). (a) Energy of a single photon absorbed by an electron (purple arrow) leads to electron emission (green arrow) if its energy $\hbar\omega$ exceeds the work function $\Phi = E_{\mathrm{vac}} - E_F$ (linear photoemission). (b) For sufficiently high field intensities, the electron can absorb the energy of several photon quanta (red arrows) leading to multiphoton photoemission even if $\hbar\omega < \Phi$. (c) A high-energy tail of a distribution with $T_h \gg T_0$ provides electrons (zoom-in) with energies exceeding the vacuum barrier (thermionic emission). Such a population can be generated by static heating or a by transient hot electrons. The Schottky effect reduces the work function to an effective value Φ_{eff} by applying a positive potential to the counter electrode (blue line). (d) A field $\mathbf{E}$ (either static or oscillating) normal to the surface reduces the barrier height and causes a finite width of the vacuum barrier at the energy of the electrons (lower red line) leading to quantum tunneling (dashed green line). Potentially, $\mathbf{E}$ is enhanced by a factor $F > 1$ at the nanostructure. In the case of an intense oscillating near-field $F\mathbf{E}$ the barrier periodically increases and decreases in the time range $[t_0, t_1 = t_0 + 1/2\omega]$ separated by one half-cycle (red shaded area). As a result, electrons can perform quiver motion in the field once they are released.

A phenomenological model that describes both linear photoemission and thermionic emission including the light intensity and temperature dependency was firstly formulated by Fowler [157] and DuBridge [158] in the early 1930s. The resulting formalism can be generalized to arbitrary nonlinearities delivering partial current densities I_n which compose to the total electron flux $I_{\mathrm{total}} = \sum_{n=0} I_n$ [159–162]. I_n is a function of the material properties including the electron escape probability, the number of electrons that absorbed the energy of n photons and the number of available electrons (see Appendix 7.1 for a brief summary of the

equations). Note that the generalized Fowler-DuBridge theory includes also the Richardson equation for thermionic emission ($n = 0$) and thermally assisted MPPE [162]. The current density I_n of the order n scales with the light intensity $I_\omega \propto |\mathbf{E}|^2$ and thus with the laser power P according to a power law, $I_n \propto |\mathbf{E}|^{2n} \propto P^n$. Most importantly, this effect can be strongly increased by plasmonic near-fields enhancing $\mathbf{E}$ by the enhancement factor F:

$$I_n \propto |F\mathbf{E}|^{2n} \propto P^n. \tag{2.5}$$

From this relation we expect an integer slope n in a double logarithmic representation ($\log I_n \propto n \log P$) for a pure n-photon process and it highlights the importance of the enhancing effect of plasmonic near-fields on the nonlinear photocurrent yield ($\propto F^{2n}$) [163, 164]. Moreover, Eq. 2.5 allows for a calculation of the near-field enhancement factor present in a photoemission process, as it is used in chap. 4.

In general, the total current density I_{total} emitted from metal tip apexes under laser illumination can involve a mixture of different mechanisms (e.g., different orders of photon absorption or photon-assisted strong-field emission) depending on the laser pulse duration, the pulse energy and the applied static bias voltage [104–106, 136, 163–172]. Furthermore, different initial electron states may contribute to I_{total}; an aspect of particular importance for gold tips, as the d-band of gold provides a significant increase of the density of states for energies approximately 2.2 eV below the Fermi edge [173, 174]. Finally, because of the ultrafast laser illumination, non-equilibrium populations and their relaxation contributes with time-dependent pathways to I_{total} [104, 171, 175]. All of this may result in non-integer photon orders when extracted using Eq. 2.5 [105, 152, 161, 163].

2.3.2 Strong-field photoemission and the Keldysh parameter

Figure 2.7(d) shows a scenario in which electronic states $E < E_{\text{vac}}$ outside the sample become accessible due to a change of the potential. For instance, applying a static negative voltage to the material with respect to a counter-electrode forms a finite barrier wall with a maximum height smaller than E_{vac}. In a quantum mechanical picture, the wave function of the electron decays exponentially but is unequal to zero inside the barrier and hence the charge has a finite probability to tunnel through the wall. This is used, for example, in field emission guns for electron microscopy [156]. Nordheim and Fowler derived the exponential current density relation $I_{\text{total}} \propto |\mathbf{E}|^2 \exp(\Phi^{3/2}/|\mathbf{E}|)$, for a static triangular potential resulting from the field component $\mathbf{E}$ normal to the metal surface [176]. In addition, the effective barrier height calculated with $\Phi_{\text{eff}} = \Phi - \sqrt{e^3|\mathbf{E}|/4\pi\varepsilon_0}$ reduces the necessary temperature for thermionic emission (cf. Fig. 2.7(c)) if sufficiently high electrostatic fields are applied (Schottky emitter) [156, 164].

Static field emission has an optical analogue called strong-field photoemission, in which the potential modification leading to tunneling is provided by the electromagnetic field. The necessarily high field amplitudes can be provided, e.g., by tip apexes illuminated with

intense laser pulses [105, 136, 163, 165, 166, 172, 177–180]. For one half-cycle a finite barrier is generated and hence "opens" the tunnel channel, whereas the next half-cycle suppresses electron transfer by increasing the potential wall (cf. red shaded area in Fig. 2.7(d)).

In general, multiphoton and strong-field photoemission may contribute to an optically driven photocurrent. The relative contributions of both are determined from the Keldysh parameter [181]

$$\gamma_K = \sqrt{\frac{\Phi}{2U_P}},$$

which distinguishes the photoemission ($\gamma_K \gg 1$) from the strong-field regime ($\gamma_K \ll 1$). The ponderomotive potential $U_P = e^2|\mathbf{E}|^2/4m_e\omega^2$ quantifies the average energy that a free charge carrier gains if it quivers in the linearly polarized sinusoidal electric field $\mathbf{E}$ normal to the surface. Essentially, decreasing the field's frequency ω or increasing the field's intensity $I_\omega \propto |\mathbf{E}|^2$ raises the strong-field contribution to the total photocurrent [164].

Laser amplification systems in combination with field enhancing nanostructures have been used to explore the transition from MPPE to strong-field photoemission for a free standing tungsten tip [105] and a platinum-gold STM junction [182]. The experiments found peak intensities of $\sim 10\,\mathrm{TW/cm^2}$ (corresponding to $|\mathbf{E}| = 10\,\mathrm{V/nm}$) for Keldysh parameters of 1 to 2. However, our experiments are operated with laser oscillators (no amplification) well above the transition ($\gamma_K \gtrsim 10$), thus strong-field processes play no role in our analysis.

2.4 Fabrication of plasmonic nanostructures

The central subjects of all presented experiments (chap. 3 to chap. 5) are gold nanotips; its fabrication can be regarded as a three-step procedure. Firstly, polycrystalline gold wires (250 µm in diameter) are annealed for $8 - 12\,\mathrm{h}$ in vacuum (base pressure $10^{-7} - 10^{-8}$ mbar) with temperatures of 650 °C to 800 °C. This increases the size of the crystal grains and provides quasi-monocrystalline apex segments after etching [45]. Scanning electron microscope (SEM) images and diffraction measurements in TEM evidence grains of several tens of micrometer in size.

Secondly, the wires are electrochemically etched in 37% hydrochloric acid with a Platinum-Iridium (PtIr) counter electrode surrounding the gold anode (Fig. 2.8(a)) [183]. The etching rate at the interface of gold, air, and solution is increased compared to the deeper immersed part of the gold wire which forms a tapered meniscus region [184]. We apply the voltage in a two-step program. Pre-etching ($\sim 100\,\mathrm{s}$) is performed with a direct current (DC) voltage of 2 V lying significantly over the redox potentials of the involved reactions that range from 0.93 V to 1.15 V [185]. This process creates a pronounced meniscus (Fig. 2.8(a)). Afterwards, a short period ($5 - 10\,\mathrm{s}$) of alternating (AC) voltages of $4 - 5\,\mathrm{V}$ square waves detaches the lower wire part leading to the apex formation. It is crucial that after the detachment the applied voltage is immediately switched off in order to prevent a blunting of

the apex due to further etching. Apex radii of the order of ~ 10 nm are achievable with this method (Fig. 2.8(b)). The high voltage etching significantly increases the surface smoothness. Subsequently, the nanostructure quality including the surface roughness, grain size, opening angle, and apex radius is examined with SEM imaging (Figs. 2.8(b-d)).

In the final fabrication step, focused ion beam (FIB) milling is used to either cut and transfer $30 - 60$ µm long apex segments to a TEM Cu wire grid used in the experiments presented in chap. 3 (Fig. 2.8(d)) or to mill a grating coupler into the shaft surface which is explored in chap. 4 (Fig. 2.8(b)). The tips utilized in the STM measurements (chap. 5) are inserted into tip holders after the second fabrication step (Fig. 2.8(c)).

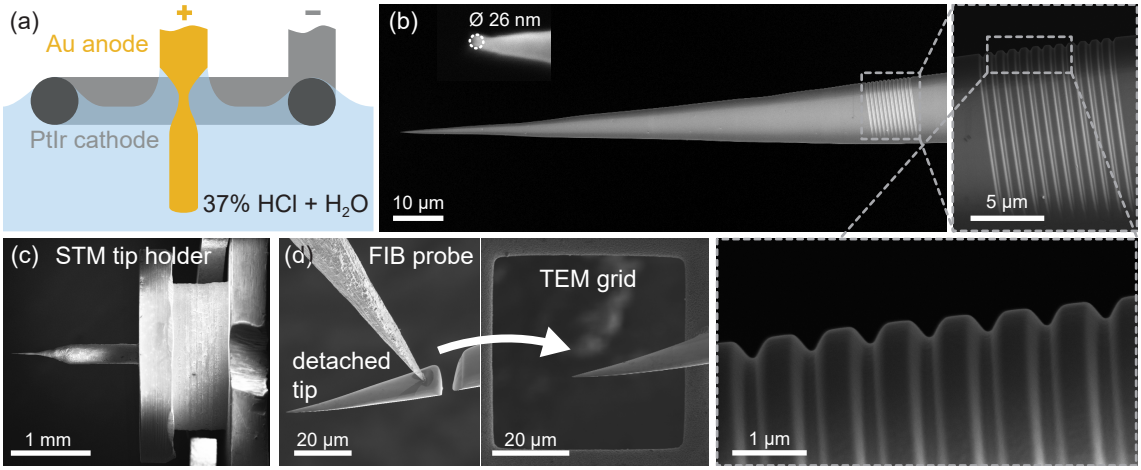

Fig. 2.8: Fabrication of gold nanotip structures. (a) Schematic illustration of the electrochemical etching process of a gold (Au) wire anode surrounded by the Platinum Iridium (PtIr) counter electrode in 37% hydrochloric acid (HCl). A meniscus in the air-gold-acid interface develops during the etching process resulting in the detachment of the immersed wire part. This provides nanotips with apex radii of the order of ~ 10 nm and sufficiently smooth surfaces. (b) Example of a gold taper with $R_T = 13$ nm (inset) equipped with a grating coupler milled with a focused ion beam (FIB) into the surface 90 µm away from the apex. The grating consists of 12 slits with a periodicity of 780 nm and a depth of 200 nm (zoom-in). (c) Our STM experiment requires tip working lengths of 2 ± 0.2 mm and specialized tip holders allowing an in-situ exchange in the STM measurement head. SEM imaging is used to ensure the correct length and tip integrity before the holder is inserted into the UHV transfer chamber. (d) For the STEM-EELS experiment tip sections of $\sim 30 - 60$ µm length are detached by FIB milling from the gold wires and transferred with the FIB probe onto conventional TEM copper grids.

CHAPTER 3

Surface plasmon polaritons on nanotip surfaces

Surface plasmon polariton (SPP) modes are evanescent, bound excitations existing at spatially extended metal-dielectric interfaces, as we have discussed in sec. 2.1. In contrast to localized surface plasmons (LSPs), SPPs travel along the interfaces [24, 73]. The conversion of SPPs into confined modes provide a convenient local excitation scheme by spatially separating the SPP generation from the interaction region [35, 128, 186–188]. A nanotip realizes such an interconversion in which the plasmon mode propagating along the shaft surface is gradually transformed into a localized excitation at the apex (see sketch in Fig. 3.1) [128, 188, 189]. This *nanofocusing* process – initially introduced by Babadjanyan et al. [190] and Stockman [191] – is accompanied by an enhancement of the electromagnetic field and a localization of the energy into nanoscale dimensions [35]. On the theoretical side, different aspects of nanofocusing has been investigated such as field enhancement [192–197], non-locality [198, 199], non-adiabaticity [200] and SPP wave packet evolution [201, 202]. Experimentally, nanofocusing has been utilized in (time-resolved) apertureless near-field scanning optical microscopy (A-NSOM) [39, 40, 45, 46, 188, 203–207], tip-enhanced Raman spectroscopy (TERS) [41, 42, 188, 208, 209], and in point-projection microscopy (PPM) [50–52, 210] as light and electron sources. Despite this variety of studies, the exact SPP propagation properties of nanotips are yet not completely understood.

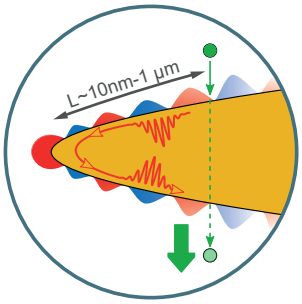

Fig. 3.1: Sketch of the experiment.

In this chapter, we investigate SPP waveguiding occurring in gold nanotip structures that are relevant in the mentioned experimental applications. The following sec. 3.1 describes the key concept of nanofocusing along metallic tips including their electromagnetic mode distribution, surface confinement and their gradual change along the tapering structure as a function of the tip's local radius $R(x)$. Subsequently, a brief concept of electron energy loss spectroscopy (EELS) in a transmission electron microscope (TEM) is presented in sec. 3.2, as we apply it to analyze the SPP mode propagation on gold tapers in real-space. The experimental findings and analysis has been published in Ref. [65] with the title "Real-space imaging of nanotip plasmons using electron energy loss spectroscopy" and is reprinted in sec. 3.3. Importantly, a semianalytical model (Ref. [66]) is used that fully captures the involved physical mechanisms resulting in the measured electron energy loss. Section 3.4 provides a complementary, recapitulating description of this model and a discussion of related studies, that – in a sense – deviate from our interpretation.

3.1 Waveguiding with metal nanotips

In general, the SPP waveguiding properties including the propagation length, localization and lifetime are essentially governed by the dispersion relation $q(\omega)$. It is derived by solving the Maxwell equations for the electric and magnetic field $\mathbf{E}$ and $\mathbf{H}$, respectively, with continuity conditions of the tangential components of $\mathbf{E}$ and $\mathbf{H}$ at the metal-dielectric interface [73]. We model a tip as a cone with a spherical apex, as schematically illustrated in the top panel of Fig. 3.2. The radius $R(x)$ depends on the two parameters apex radius R_T and opening angle α_T. An adequate theoretical description – known as adiabatic nanofocusing – can be found by approximating the tip structure with thin cylinders with slowly decreasing radii $R_i(x_i)$ which are stacked up to resemble the tip (bottom panel in Fig. 3.2) [191, 211].

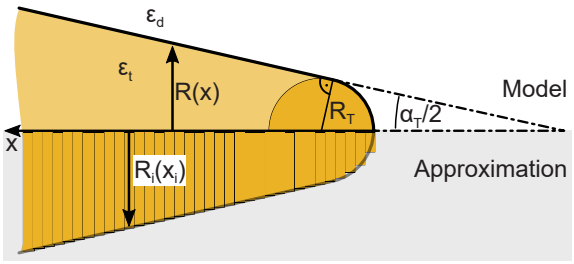

Fig. 3.2: Model and approximation of a metal tip. The tip's radius $R(x)$ is the surface of a cone with an opening angle of α_T truncated by a spherical apex with radius R_T and $R(0) = 0$ (black curve). Nanofocusing and electron energy loss is calculated for the tip modeled as a stack of thin cylinders at position x_i with radius R_i in such a way that $R_i(x_i) = R(x)$.

The electromagnetic eigenmodes (the fields $\mathbf{E}$ and $\mathbf{H}$) of a cylinder of radius R in cylindrical coordinates $\mathbf{r} = (r, \varphi, x)$ are determined by the scalar function

$$F_{j,m}(r, \varphi, x) = f_{j,m}(q_j r) \cdot \exp\left(im\varphi + iqx - i\omega t\right) \tag{3.1}$$

for the inside ($j = t$) and outside ($j = d$) of the cylinder [212, 213]. Here, the x-component of the wave vector (propagation constant) and the azimuthal mode order are denoted with

q and the integer m, respectively. The radial field distribution is governed by $f_{j,m}(q_j r)$ that is mainly determined from Bessel J_m and Henkel $H_m^{(1)}$ functions of the order m. Since we are interested in the surface bound (non-radiative) eigenmodes of the cylinder, the waves must not propagate radially and the radial wave vector components

$$q_t = -\sqrt{\left(\frac{\omega}{c}\right)^2 \varepsilon_t - q^2} \qquad \text{and} \qquad q_d = \sqrt{\left(\frac{\omega}{c}\right)^2 \varepsilon_d - q^2}, \tag{3.2}$$

must be imaginary. This follows from momentum conservation ($q_j^2 + q^2 = \varepsilon_j k^2$) with the free space wavenumber $k = \omega/c$. The dispersion relation $q(\omega)$ we are looking for is calculated by a transcendental equation derived from the continuity condition at the cylindrical surface (see Appendix 7.2). In particular, combinations of q_{mR} and ω that fulfill Eq. 7.1 for a given azimuthal mode number m and a cylinder radius R provide the SPP dispersion [189, 212, 213].

In direct comparison to the dispersion of freely propagating electromagnetic waves ($\omega = ck$) surface bound SPP modes are found to have a wavenumber larger at a given energy, as found in sec. 2.1. Figure 3.3(a) shows the real part of the dispersion relation $\mathrm{Re}(q)$ of the fundamental mode ($m = 0$) for gold cylinders of different radii ($R = 30\,\mathrm{nm}$ to $R = \infty$, solid lines, increasing with gray arrow) and for energies in the near-infrared to the visible range[1] calculated with Eq. 7.1. We observe an increasing wave vector with decreasing radii, i.e., the SPP wavelength $\lambda_{\mathrm{spp}} = 2\pi/\mathrm{Re}(q)$ decreases for smaller tip radii. This wavelength compression is one of the remarkable properties of nanofocusing (see below). Since the radial field extension (Eq. 3.2) decreases simultaneously this leads to a stronger confinement. For radii in the micrometer regime, the curves match to the dispersion relation of the planar interface given by Eq. 2.3 (solid black line in Fig. 3.3(a)) [73].

The oscillating electrons in the metal are strongly affected by scattering events (damping) [132, 133]. Quantitatively, the SPP intensity is reduced by a factor of e^{-1} for a propagation distance of $L_{\mathrm{spp}} = 1/|2\ \mathrm{Im}(q)|$ (Fig. 3.3(b)) [73]. For a broad energy bandwidth L_{spp} has values of several tens to a few hundreds of micrometer. If the energy of the SPP mode reaches the d-band edge of gold $\gtrsim 2.2\,\mathrm{eV}$ interband transitions drastically reduce L_{spp} down to the sub-micrometer domain, thus causing inefficient SPP waveguiding for these energies [134]. Moreover, the propagation length is increased for larger cylinder radii (gray arrow in Fig. 3.3(b)).

Up to now we have concentrated on the dispersion of the fundamental mode ($m = 0$). The physical meaning of m is illustrated by the insets of Figs. 3.3(c) and (d) as the different associated transverse field distributions. The fundamental mode is constant along the azimuthal direction φ and its polarization points in a direction normal to the surface (radial direction r). Higher-order field distributions exhibit a number of $2 \cdot m$ nodes resulting in multipolar fields, for instance, in a dipole-, quadrupole-, or hexapole-like distribution for

[1] This is the energy range relevant for our discussion; details on an extended energy scale can be found, e.g., in Refs. [24, 73].

$m = \pm 1$, $m = \pm 2$, or $m = \pm 3$ with the sign governing the direction of rotation [213, 214]. The high-order dispersions show also a different quantitative behavior, since the modes only exist for energies exceeding a certain cut-off relation $q(\omega_c)$ that depends on the cylinder radius and mode number (cf. black dots in (c) and (d)) [213, 215]. $q(\omega_c)$ increases with increasing mode order (for a constant radius).

Effectively, for a given mode m and energy $\hbar\omega$ this results in a cut-off radius R_c below which the mode cannot exist anymore. Importantly, the taper acts as a mode filter: Only the $m = 0$ mode propagates without a cut-off all along a tapered nanostructure and converges into nanometric volumes at the apex [65, 66, 191, 216, 217]. However, higher-order modes can be excited for radii $R > R_c$ and their mode superposition forms a complex interference pattern in energy loss measurements [65, 218, 219], as we demonstrate in secs. 3.3. These modes are gradually converted to radiative modes if they approach the respective cut-off radius [110, 217, 218].

Now we can investigate the central properties of nanofocusing by following the idea of stacked cylinders with decreasing radii to approximate a nanotip (see Fig. 3.2) for the excitation energy[2] $\hbar\omega = 1.55\,\mathrm{eV}$. The local radius $R(x)$ of the metal tip continuously decreases with a rate of $R' = \mathrm{d}R/\mathrm{d}x$ which is assumed to be small [191] (limits are discussed below). As we have seen, this leads to a gradual compression of the SPP wavelength λ_{spp} (increasing $q(\omega)$): For radii $10\,\mathrm{nm} \lesssim R \lesssim 100\,\mathrm{nm}$, λ_{spp} reduces from $\sim 730\,\mathrm{nm}$ to $\sim 270\,\mathrm{nm}$ (Fig. 3.3(e)). This has three striking consequences. Firstly, the field localizations $L_{\mathrm{tip}} = 1/|2q_t|$ and $L_{\mathrm{vac}} = 1/|2q_d|$ are connected to q (and thus λ_{spp}) via Eq. 3.2. With decreasing λ_{spp} also L_{tip} and L_{vac} in the tip and the vacuum are reduced down to 10 nm and 20 nm at $R = 10\,\mathrm{nm}$, respectively (Fig. 3.3(f)). Hence, the field localization at the tip apex is of the order of the apex radius corresponding to a confinement far below the diffraction limit of far-field light [189]. This reflects our findings for LSPs in sec. 2.1. Secondly, the SPP waves become slower approaching the tip end, because the group $v_g = |\mathrm{d}\omega/\mathrm{d}q|$ and phase velocity $v_p = |\omega/q|$ drastically decrease from a value close to the speed of light c down to a few percentage of c (Fig. 3.3(g)) [191]. Thirdly, a strong field enhancement and optical energy confinement is present for adequate small radii [35].

Typically, the theoretical studies on this subject and on the demonstration of wavelength compression and field enhancement rely on very small structure dimensions ($R \approx 1\,\mathrm{nm}$, $\alpha_T \leq 5°$) (e.g., in Refs. [191, 199]), which are hard to achieve by experimental schemes. This is also accompanied by rather unrealistic field enhancement factors F reaching several hundreds. However, these studies give valuable insights into the general mechanism and provide a versatile toolbox for the calculation of tip structures used in sec. 3.3.

[2] This energy corresponds to 800 nm that is the central wavelength of the widely used Titanium:Sapphire laser oscillator (A typical bandwidth is indicated in Fig. 3.3(a) by the red shaded area).

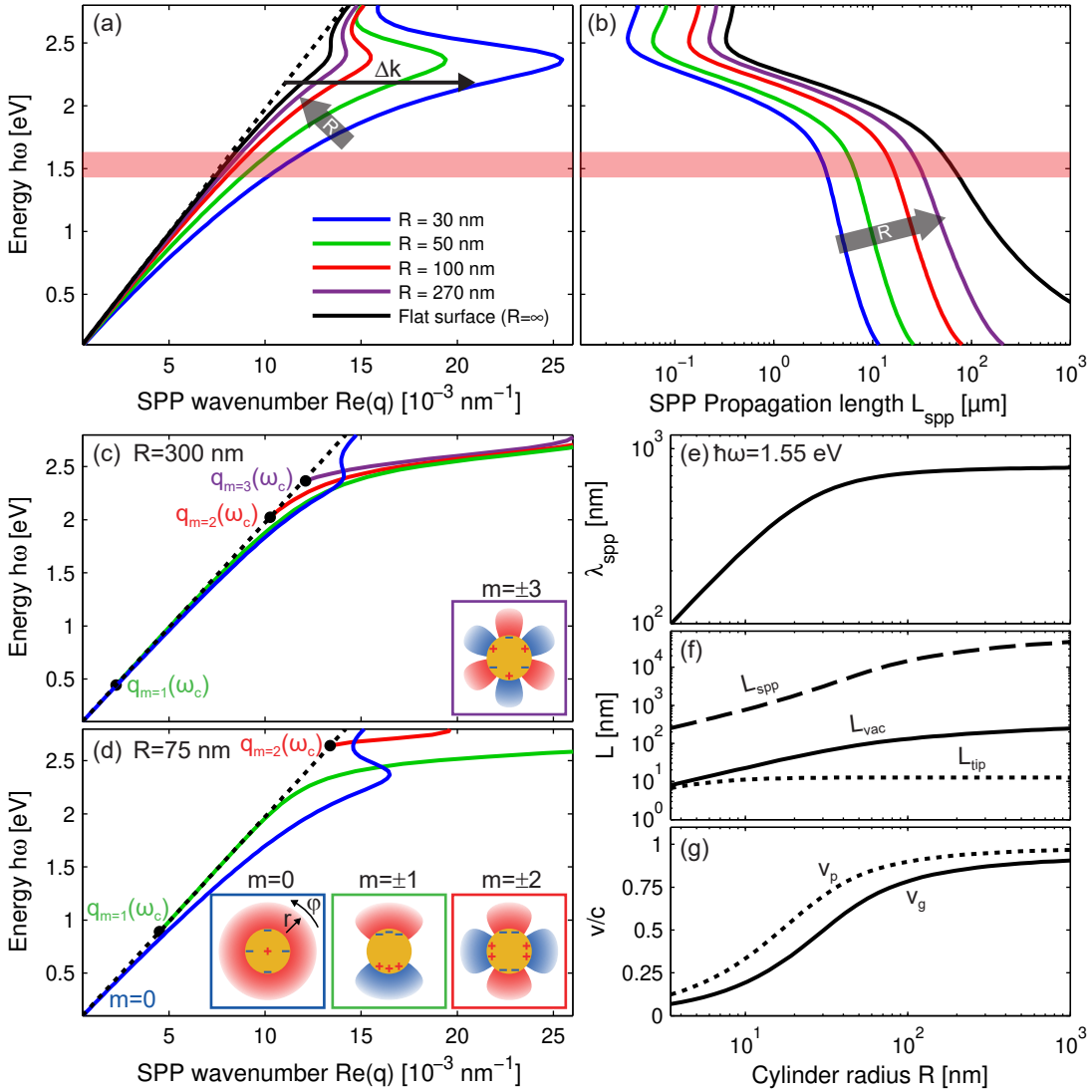

Fig. 3.3: Nanofocusing SPP propagation on a gold tip. (a) The dispersion relations $\mathrm{Re}(q(\omega))$ for the cylinder radii 30 nm, 50 nm, 100 nm, and 270 nm (blue to purple lines). With increasing radius (gray arrow) the wave vector decreases and finally converges to the flat interface SPP dispersion (solid black line). A momentum mismatch Δk (black arrow) between far-field light (dotted black line) and SPPs prevents a direct coupling. The energy range of 1.55 ± 0.1 eV provided by typical Titanium:Sapphire laser oscillators (used in the experiments presented in chap. 4) is indicated by the red shaded area. (b) With increasing radius R (gray arrow) SPPs are less damped and exhibit an increasing propagation length $L_{\mathrm{spp}} = 1/|2\ \mathrm{Im}(q)|$ (same radii as in (a)). (c,d) Higher-order mode dispersion for the cylinder radius $R = 300$ nm (c) and $R = 75$ nm (d) ($m = 0$ to $m = \pm 3$ are indicated and correspond to the blue to purple line). A cut-off relation $q_m(\omega_c)$ prevents SPPs for $\omega < \omega_c$ (black dots) at the free light dispersion (dotted line). Only the fundamental mode (blue line) does not have a cut-off radius and exists for $R \to 0$. The insets schematically present the cross-sectional electromagnetic field and surface charge distribution as a function of azimuthal (φ) and radial (r) position (not to scale). (e-g) For $\hbar\omega = 1.55$ eV, nanofocusing exhibits a strong influence on SPP propagation for $R \lesssim 100$ nm. The wavelength λ_{spp} reduces from 730 nm to 270 nm at $R = 10$ nm (e), while the propagation length L_{spp} is suppressed to < 1 µm (dashed line in (f)). Importantly, the intensity is strongly localized to dimensions of the order of the tip radius ($L_{\mathrm{vac}} = 130$ nm to 20 nm) in the vacuum (solid line) accompanied by a slight confinement ($L_{\mathrm{tip}} = 13$ nm to 10 nm) in the metal (dotted line). The phase (v_p) and group velocity (v_g) decrease to 30% and 20% of the speed of light at $R = 10$ nm, respectively.

The applicability of the presented approximation has a major limit which concerns the slow tapering rate R' of the tip. We assume an adiabatic change of the SPP wavelength over a propagated distance of λ_{spp}. In this case, the mode does not "feel" the tapering change and gradually adjusts itself to the smaller radius [35]. From an eikonal approximation the condition of this adiabaticity can be expressed by the adiabatic parameter [191],

$$\delta_{\mathrm{ad}}(x) = R' \frac{\mathrm{d}(q^{-1})}{\mathrm{d}R} \ll 1. \tag{3.3}$$

Numerical studies demonstrated that the limit can be estimated to $\delta_{\mathrm{ad}}(x) < 0.85$ [36, 200, 220]. Consequently, this restricts the tip opening angle to a critical value below which adiabatic nanofocusing occurs ($\lesssim 25°$ for visible light and gold tips) [220].

Adiabatic nanofocusing predicts an asymptotic stopping of an SPP approaching the singularity ($R = 0$) at the tip end due to the decreasing group and phase velocity (cf. Fig. 3.3(g)) [191]. However, real tips are truncated by a curved apex leading to a breakdown of the adiabatic condition at some point. This is accompanied by coupling to radiating far-field modes, by absorptive losses and by SPP mode reflection [65, 66, 128, 200, 219]. Thereby, the achievable field enhancement and confinement are limited.

3.2 Experimental setup: electron energy loss measurement

This section briefly explains the instrumentation[3] of STEM-EELS; the technical specifications of the instrument used in the experiment are found in sec. 3.3.6 'Electron energy-loss spectroscopy instrumentation'. A sketch of the setup is illustrated in Fig. 3.4(a). Electrons generated in a field emitter gun are fed into an electrostatic monochromator (omega-type) and accelerated to the desired operation energy. A magnetic lens system guides the charge carriers through a unit that corrects for spherical aberrations (C_s-corrector) and also provides the lateral raster scanning of the beam in the xy-plane. The corrected and energy filtered beam is focused onto the sample plane in which the electron-matter interaction takes place. Subsequently, the scattered electrons are collected by either a high-angle annular dark-field (HAADF) detector or by an energy loss spectrometer. This combination provides simultaneously geometrical (by the HAADF) and spectral (by the EELS) information as a function of beam position (x_e, y_e). This allows for the correlation of a specific energy loss with the morphology of the sample.

An example of an HAADF image of a gold tip is presented in Fig. 3.4(b). The energy loss spectrum at the position marked by the green dot is plotted in Fig. 3.4(c). It is centered at the zero-loss peak (ZLP) representing the electrons undergone elastic scattering or very small interactions. The quantity determining the energy resolution is the width of the ZLP (130 meV in (c)). Electron-matter interaction (back-action of induced electromagnetic modes) is present as oscillating signatures in the loss spectra for energies beyond the ZLP

[3] A comprehensive description of the TEM used in our experiment can be found in Ref. [221].

overlap (inset). Although a factor of $10^{-3} - 10^{-4}$ smaller than the ZLP maximum, the SPP signal is clearly distinguishable compared to a reference spectrum (black line) recorded without any electron-sample interaction.

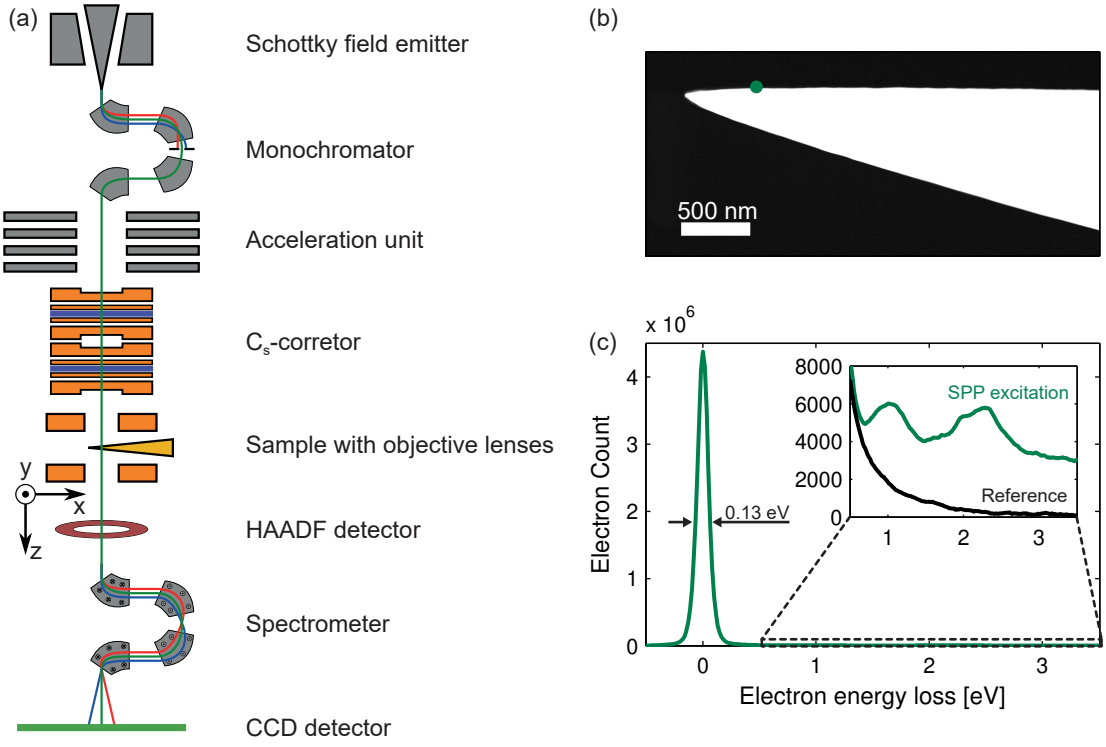

Fig. 3.4: STEM-EELS experiment. (a) Schematic illustration of the setup used in our experiments. (b) HAADF image of a gold tip. (c) Example of a typical loss spectrum (green line) measured at a position close to the tip surface (green dot in (b)). The distribution of the dominating zero-loss peak (ZLP) gives the energy resolution of 130 meV at full-width at half-maximum. (Inset) Electron-matter interaction causes pronounced signal features in the energy loss range of $\gtrsim 0.5$ eV (green line) that are clearly distinguishable from the reference spectrum recorded at a remote position from the sample (black line).

3.3 Real-space imaging of nanotip plasmons using electron energy loss spectroscopy

Benjamin Schröder, Thorsten Weber, Sergey V. Yalunin, Thomas Kiel, Christian Matyssek, Murat Sivis, Sascha Schäfer, Felix von Cube, Stephan Irsen, Kurt Busch, Claus Ropers, and Stefan Linden
Physical Review B **92** (2015), 085411
DOI: 10.1103/PhysRevB.92.085411

Abstract We report the spatial mapping of surface plasmons on conical gold nanotips by electron energy-loss spectroscopy. We observe standing wave patterns resulting from reflections of the fundamental surface plasmon mode at the nanotip apex. The experimental results are in very good agreement with numerical calculations using the discontinuous Galerkin time domain method and analytical computations based on a cylindrical mode expansion.

3.3.1 Introduction

Metallic nanostructures can capture propagating optical waves and confine the electromagnetic energy in nanometric volumes by the excitation of surface plasmons [73]. The associated enhancement of the local light intensity is of great interest for nanoscale spectroscopy and locally amplified light matter interactions [22, 30, 31]. These features have been essential for the development of plasmonics, enabling nanostructure-based light control [21, 25, 35, 37].

A prototypical structure combining both localized and delocalized plasmonic excitations and their interconversion is the conical metallic nanotip. It features an intense optical hot spot, which may be directly generated by focusing far-field radiation onto the apex. The corresponding near-field excitation has enabled various applications in imaging and spectroscopy, including tip-enhanced Raman scattering [222], apertureless near-field optical microscopy (A-NSOM) [183, 223], and ultrafast photoemission [170, 172]. Particularly efficient optical coupling into the apex excitation can be achieved with geometrically converging bound surface plasmon polariton (SPP) modes traveling towards the apex, a process commonly referred to as nanofocusing [35, 190, 191]. On conical tips, nanofocusing was demonstrated using grating coupling [128], with subsequent applications in A-NSOM [45, 188, 203, 204]. In order to fully harness the capabilities of this scheme, detailed knowledge of the spatial and spectral distribution of the plasmonic near-field is of upmost importance. Moreover, relevant questions involve fundamental and higher-order SPP mode dispersions on conical nanotips [224], as well as the precise breakdown of the adiabatic approximation, the role of SPP reflection near the apex [200], and the influence of these phenomena on achievable local field enhancements.

Interestingly, although the local hot spot at the apex has been employed in numerous ex-

periments, the actual propagating SPP modes responsible for nanofocusing on conical tapers have so far not been imaged in real space. Employing inelastic electron scattering processes, cathodoluminescence spectroscopy [225–227] and electron energy loss spectroscopy (EELS) [113, 228–233] as well as photon-induced near-field electron microscopy (PINEM) [146, 234] have been very successful in mapping photonic modes in nanostructures with high spatial and spectral resolutions. EELS resolves the spontaneous energy loss arising from swift electrons passing through or nearby a structure, and interacting with the self-induced electric field (see Fig. 3.5(a)) [74, 119, 235].

Here, we report the spatial mapping of surface plasmons on conical gold nanotips using EELS. We observe the formation of standing wave patterns in the loss distribution, which is shown to be formed by SPP reflection in the apex region. The experimental EELS maps are in very good agreement with numerical calculations using the discontinuous Galerkin time domain (DGTD) method and analytical computations based on a cylindrical mode expansion. Among the processes that govern the achievable field enhancement in nanofocusing, such as local absorption and far-field scattering, we demonstrate that the SPP reflection at the apex plays a major role.

3.3.2 Experiments

The measurements were carried out on gold nanotips fabricated by electrochemical etching of thermally annealed 0.25 mm diameter wires in hydrochloric acid, similar to a method reported in Refs. [45, 183]. For each tip, a 30 µm long section of the resulting conical structure was separated from the wire by focused ion beam etching, followed by a transfer to a standard transmission electron microscopy (TEM) grid (50 µm mesh size). Inspection of the prepared tips by scanning electron microscopy yields full opening angles between 9° and 20° and radii of curvature of $10 - 30$ nm. To spectrally and spatially map surface plasmon propagation on the nanotips, we use EELS in combination with scanning TEM at 200 keV electron energy, achieving an energy resolution of 0.13 eV. For details see Supplemental material 3.3.6 'Electron energy-loss spectroscopy instrumentation'.

In the experiments, an electron-beam is raster scanned normal to the cone axis over an area of several μm^2 in the apex region of the tip, recording EEL spectra at every position (see Fig. 3.5(b),(c)). Figure 3.5(d)-(k) displays EEL maps for selected loss energies for a tip with an opening angle of 14° and 13 nm radius of curvature of the apex (see Fig. 3.5(b)). At all energies, we observe a pronounced maximum near the apex and clear spatial oscillations along the cone, with a decreasing period for higher loss energies. Fig. 3.6(a) depicts energy- and position-dependent lineouts through the spectral data, recorded parallel to the edge of the cone. This representation illustrates the continuous energy-dependent shift and period-shortening of the observed oscillations. In particular, it is evident that the first maximum shifts towards the apex for energies below 1 eV and remains localized at this position for higher energies.

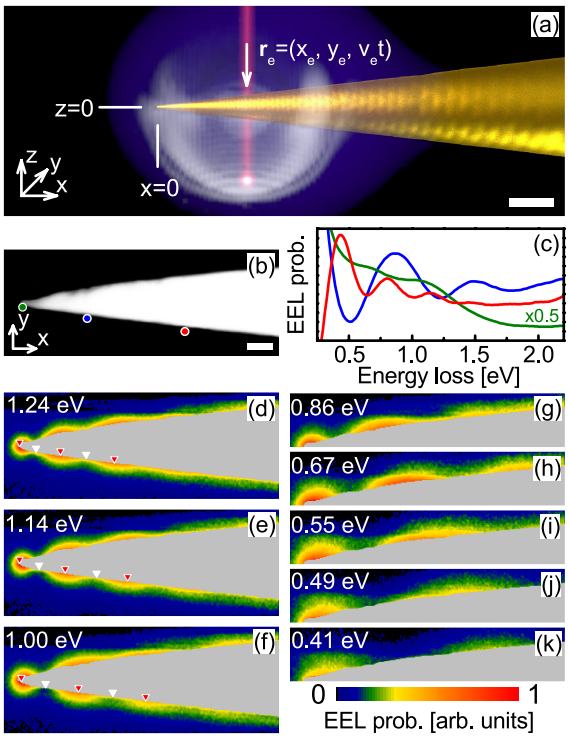

Fig. 3.5: (a) Illustration of swift electron (trajectory $\mathbf{r}_e$ with velocity v_e in z-direction) interacting with the self-induced field at a nanoscale tip. Scale bar: 500 nm. The color-coded image represents the absolute value of the self-induced field for a specific time delay obtained by DGTD simulations described in the main text (see also Supplemental material 3.3.6 'Computation of the loss probability' and movie in Supplemental material) (b) High-angle annular dark-field TEM image of the raster scanned area. Scale bar: 200 nm. Apex radius: 13 nm, opening angle: 14°. (c) Exemplary electron energy loss (EEL) probability spectra at positions indicated in (b). (d-k) Normalized EEL maps for energies between 0.41 eV and 1.24 eV. A gray mask covers the opaque tip area. Positions of maximal and minimal loss signals along the tip edge are indicated by red and white triangles, respectively. Increasing the energy loss leads to a shift of the nodes and antinodes towards the apex. Color scale is normalized to the maximum value in each panel.

3.3.3 Numerical calculations

Spatial oscillations in the local EEL intensity are well-known from finite structures exhibiting a discrete set of resonant modes governed by geometrical boundary conditions [113, 229–232]. At nanowires of constant diameter, surface plasmon reflections at terminations were recently reported [233]. It is not obvious, however, in what way such concepts translate to a conical nanofocusing geometry, which involves adiabatic wave compression and axially varying propagation constants within a set of azimuthal modes. To theoretically analyze this scenario, we conducted two types of calculations yielding insight into the energy loss mechanisms and the near-field modes involved. As we will show below, the observations primarily arise from reflection of the fundamental azimuthal mode of the SPP at the apex, leading to standing wave interference. The first set of simulations was conducted using the Discontinuous Galerkin Time Domain (DGTD) method [236, 237]. It allows for a solution of Maxwell's equations in the time domain for arbitrary geometries. Specifically, the DGTD method allows us to compute the polarization induced in the nanostructure by a traversing classical, relativistic electron. The back-action of the induced field on the electron is then responsible for the loss process [74, 119]. The details of the method and its application to EELS are outlined in Supplemental material 3.3.6 'Computation of the loss probability'. The gold tip is modeled as a cone with opening angle 14°, finite length of 15 µm and apex radius of 20 nm. The permittivity of gold is modeled as a linear combination of one Drude and three Lorentz poles (see Supplemental material 3.3.6 'Solution of Maxwell's equations'). Fourth-order elements with element sizes down to 1.5 nm near the tip apex were employed.

Using the experimental geometry and without adjustable parameters, we obtain quantitative agreement with the experimental findings regarding the energy- and position-dependent loss profiles (Fig. 3.6(b)). Specifically, excellent correspondence of the positions of local extrema is obtained including the previously described shift of the apex maximum (for better comparison, red and white lines in Fig. 3.6(b) denote positions of experimental maxima and minima, respectively).

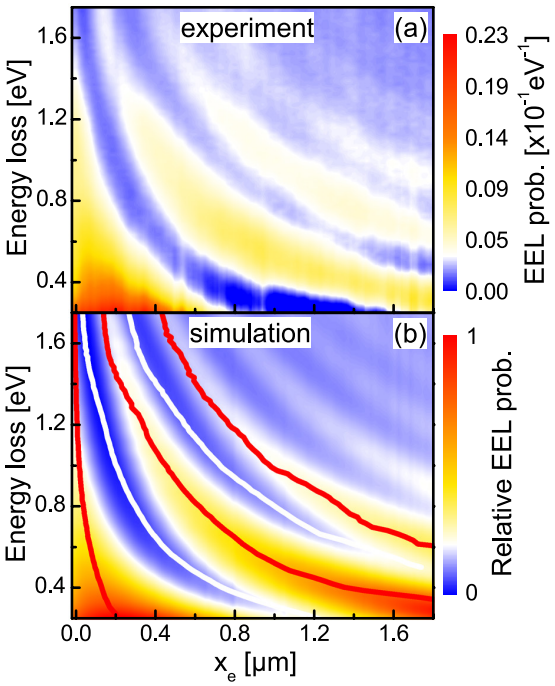

Fig. 3.6: (a) Energy- and position-dependent loss probability distribution evaluated along the lower tip edge (see Fig. 3.5). $x = 0$ corresponds to the apex position. (b) Corresponding simulation using the DGTD method and the geometry of the experiment. Red and white lines indicate positions of local maxima and minima, respectively, in the experiments. The color scale is normalized to the maximum.

The microscopic origin of the observed spatial and spectral modulations can be identified from the time-domain representation of the computed induced electric field as depicted in Fig. 3.5(a). Figure 3.7 displays the magnitude of the induced electric field near the tip surface (in the tip plane, $z = 0$) as a function of time and distance from the apex, for an electron traversing the tip at the position $x_e = 950$ nm. At the time $t = 0$ (time of closest distance between electron and surface), two SPP wave packets are generated, propagating towards (left) and away from (right) the apex (see arrows). The former is reflected at the apex and reaches the original excitation position x_e at a time $t \approx 9$ fs. The SPP reflection observed in Fig. 3.7 also manifests itself in a retarded action on the electron, which causes the spectral and spatial oscillations found (cf. Fig. 3.6). (The Supplemental material presents a movie of the induced time-dependent, three-dimensional intensity distribution.) We note that, at the position of the electron (treated as a point particle), the SPP reflection is not directly evident in the time-dependent induced electric field: Within the time span between the excitation and the back-reflection to the excitation point, the electron leaves the near-field region. However, in the standard treatment of EELS [74], the temporal Fourier components of the induced field along the entire line trajectory enters in the loss probability (see Supplemental material 3.3.6 'Computation of the loss probability'). Thus, despite a purely classical treatment, one may consider the delocalization of the quasimonoenergetic electron along its trajectory to be implicitly included in the description.

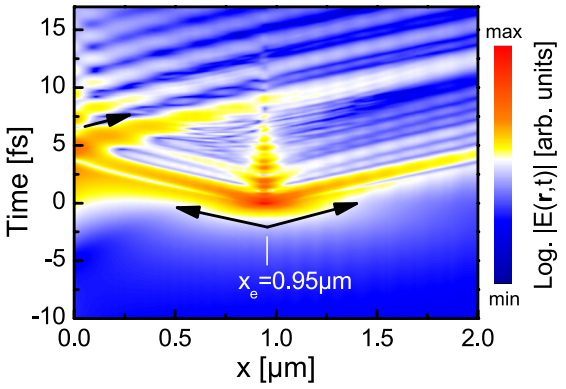

Fig. 3.7: Space-time representation of the magnitude of the induced electric field along the metal surface of the tip (in the tip plane $z = 0$) for an electron passing by the structure at $x_e = 950$ nm, and at a minimum distance of 50 nm from the surface in the y-direction. Outgoing wave packets to the left and right are visible, together with pronounced reflections at the tip apex (arrows).

3.3.4 Semianalytical model

In order to connect our observations to the nanofocusing phenomenon, it is very instructive to study the influence of individual bound SPP modes propagating along the tip on the EEL intensity. To this end, we developed a fully retarded semianalytical model to calculate the loss probability distribution for a given position along the cone surface (see also Supplemental material 3.3.6 'The semianalytical model'). The model locally approximates the cone as a straight cylinder of the same radius and accounts for SPP propagation on the tapered structure in an adiabatic picture [190, 191]. The self-induced field responsible for the EEL signal [74] can be expanded in a series of cylindrical vector harmonics [238]. Some of these correspond to surface bound SPP modes, which are characterized by a propagation constant (on-axis wave vector) q and azimuthal mode index m. The fundamental azimuthal mode is labeled with $m = 0$, and positive (negative) indices denote modes that are rotating parallel (antiparallel) relative to the traversing electron.

Figures 3.8(a) and (c) display the computed excitation probabilities (and therefore EEL probabilities) of different SPP modes as a function of probe position (solid lines), derived using the local cone diameter. The fundamental mode has no cut-off, as discussed before [216], and can therefore be excited at any distance from the apex, with a close to exponential decay probability towards larger radii. In contrast, the higher-order modes each exhibit a cut-off at particular cone radii. Coupling to the negative index azimuthal modes is strongly suppressed (exemplarily shown for the $m = -1$ mode in Fig. 3.8(a),(c), orange lines), which can be understood by considering the angular momentum mismatch between these modes and the external field created by the electron. SPP reflections are incorporated in the model by coupling to both left- and right-propagating modes, with a locally varying relative phase that is derived from an action integral (adiabatic approximation) containing propagation to the reflection point and back. The resulting interference pattern for the fundamental mode (reflection at the apex) is plotted as a dashed line in Fig. 3.8(a),(c), and Fig. 3.8(b),(d) compares the predicted cumulative EEL probability for all modes (solid lines) to experimental traces (circles) from a second tip (opening angle 11°, tip radius 17 nm; cf. high-angle annular dark-field TEM image, EEL maps,

and lineout plot in Fig. 3.9 in Supplemental material 3.3.6 'Experimental results on a second nanotip'). Very good agreement between experiment and model is already found by including the apex reflection of only the fundamental mode. Furthermore, a moderate wavelength compression near the apex [190, 191] is reproduced. We note that extreme wavelength compression is not expected for the given energies and cone diameters, and pronounced SPP reflection is the only discernible consequence of the apex-related breakdown of the adiabatic approximation. Possible cut-off-related reflections of higher-order modes may contribute to the dephasing of the modulations observed at larger distances, but are insignificant near the tip end (up to 2 µm at energies below 1 eV), and can also be suppressed by coupling to the far-field.

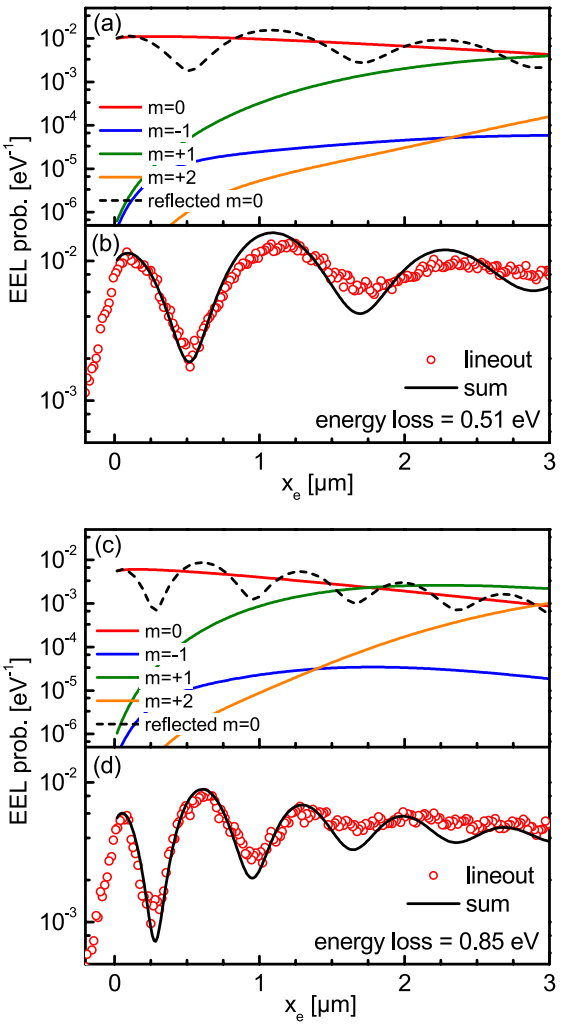

Fig. 3.8: Semi-logarithmic plots of the experimental and calculated loss probabilities for energies of 0.51 eV and 0.85 eV as a function of probe position. (a,c) Solid lines: loss probabilities of individual modes (radius of curvature: 17 nm, opening angle: 11°). Dashed line: Apex reflection of the fundamental mode leads to an oscillating loss probability. (b,d) Experimental trace (circles) and model computations (solid lines), summing over azimuthal modes.

3.3.5 Summary

In conclusion, we have demonstrated the real space imaging of surface plasmon polaritons on gold nanotips using EELS. The experimental findings are in quantitative agreement with results from DGTD simulations and analytical computations. The results highlight the importance of apex reflections of the fundamental azimuthal SPP mode, with direct consequences for future plasmonic nanofocusing applications.

Acknowledgments We gratefully acknowledge financial support by the Deutsche Forschungsgemeinschaft (DFG) within SFB-1073 (project C04).

B. Schröder and T. Weber contributed equally to this work.

3.3.6 Supplemental material

Electron energy-loss spectroscopy instrumentation

The experimental work was carried out using a Zeiss Libra200 MC Cs-STEM CRISP (Corrected Illumination Scanning Probe) operated at 200 kV. The instrument is equipped with a monochromated Schottky-type field-emission cathode (MC-FEG), and a double hexapole-design corrector for spherical aberrations of the illumination system (C_s-corrector). Both components, the monochromator and the C_s-corrector, are manufactured by CEOS GmbH.

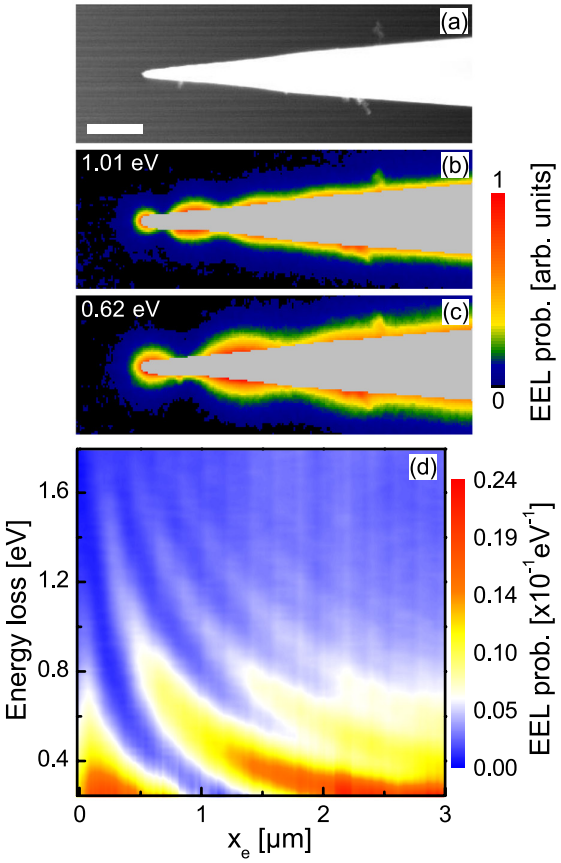

Fig. 3.9: (a) High-angle annular dark-field TEM image of the raster-scanned area. Scale bar: 500 nm. Apex radius: 17 nm, opening angle: 11°. (b), (c) EEL maps for 1.01 eV and 0.62 eV loss energy. A gray mask covers the opaque tip area. The color scale is normalized to the maximum value in each panel. (d) Energy- and position-dependent loss probability distribution evaluated along the upper tip edge. $x = 0$ corresponds to the tip position.

For EELS experiments an in-column Omega-type energy filter, fully corrected for second order aberrations, is integrated into the microscope column [239]. The spectra are recorded using a Gatan UltraScan 2 k × 2 k CCD camera with an acquisition time for each spectrum of 15 ms and a dispersion of the spectrometer of 0.016 eV/channel. The energy resolution, which is defined by the full-width-at-half-maximum of the spectrum's zero-loss peak, varies from 0.098 eV to 0.163 eV, depending on the spatial position on the scan area. In the present STEM-EELS experiments, the electron-beam raster-scans over the sample with a step width of 6 nm.At each step on the 1.95 µm × 0.79 µm scan area, an energy-loss spectrum is recorded. For data post-processing, every spectrum is normalized to its total number of electron counts. Subsequently, the first moment of the zero-loss peak is centered to 0 eV for each spectrum. For presenting the EEL-maps, the zero-loss peak, determined from a reference measurement, is subtracted from the spectra.

Experimental results on a second nanotip

Figure 3.9(a) shows a high-angle annular dark-field TEM image of a second gold nanotip. The nanotip has an opening angle of 11° and a radius of curvature of the apex of

17 nm. Figure 3.9(b),(c) show two exemplary EEL maps. Also on this nanotip, standing wave patterns can clearly be identified. In Fig. 3.9(d), lineouts of the electron energy-loss probability are depicted as a function of energy and position. From lower to higher energies, one observes a shift and period-shortening of the oscillations.

Computation of the loss probability

The probability that an electron loses the energy $\hbar\omega$ when passing a target particle is given by [74]:

$$\Gamma(\omega) = \frac{e}{\pi\hbar\omega} \int \mathrm{d}t \, \mathrm{Re}\left(e^{-i\omega t}\mathbf{v} \cdot \mathbf{E}^{\mathrm{ind}}\left(\mathbf{r}(t), \omega\right)\right) \tag{3.4}$$

where e is the unit charge, and $\mathbf{E}^{\mathrm{ind}}\left(\mathbf{r}(t), \omega\right)$ is the Fourier component of the electric field induced by the electron evaluated at the electron's position. Therefore, the computation of the Electron Energy Loss Probability (EELP) reduces to computing the induced field, i.e., the total field minus the incident field. Usually the momentum transfer to the electron is neglected, such that it travels along a straight-line trajectory with constant velocity. This assumption, known as the non-recoil approximation (NRA), allows for an analytic evaluation of the incident field caused by the electron. The field is given by

$$\begin{aligned}
\mathbf{E}\left(\mathbf{r}, t\right) &= \frac{e\gamma}{4\pi\varepsilon_0\varepsilon} \frac{\mathbf{d}(t)}{\left(\mathbf{d}^2(t) + \left(1/\gamma^2 c^2\right)\left(\mathbf{d}(t) \cdot \mathbf{v}\right)^2\right)^{3/2}}, \\
\mathbf{H}\left(\mathbf{r}, t\right) &= \frac{\mathbf{v}}{c^2} \times \mathbf{E}\left(\mathbf{r}, t\right),
\end{aligned}$$

with $\mathbf{d}(t) = \mathbf{r}_e(t) - \mathbf{r}$ and $\gamma = 1/\sqrt{1 - v^2/c^2}$. We choose the electron to travel in z direction. Within the NRA, the electron trajectory is then given by $\mathbf{r}_e(t) = (x_e, y_e, v_e t)$. This allows us to rewrite Eq. 3.4 as

$$\Gamma(\omega) = \frac{e}{\pi\hbar\omega} \int \mathrm{d}z \, \mathrm{Re}\left(e^{-i\omega z/v_e} E_z^{\mathrm{ind}}\left(x_e, y_e, z, \omega\right)\right). \tag{3.5}$$

Having an analytic expression for the incident field at hand allows us to use a pure scattered field formalism [240] to directly solve for the induced field required in Eq. 3.5. Note that, as we are going to solve in the time domain, we need to compute the Fourier component of the induced field required in Eq. 3.5. Therefore, we record $E_z^{\mathrm{ind}}\left(x_e, y_e, z, t\right)$ for all z on the trajectory and perform a Fourier transform before evaluating the EELP (Eq. 3.5).

Solution of Maxwell's equations

We solve the full vectorial Maxwell equations for the induced field using the Discontinuous Galerkin Time Domain method [236]. We model the experimental gold tip as a cone with an opening angle of 14°. The computational domain is truncated to a 21 µm × 8 µm × 8 µm cuboid with Perfectly Matched Layers (PMLs) of 500 nm thickness at the outer boundaries

to prevent spurious reflections. In lack of a possibility to terminate the metallic cone in PMLs, we assume it to have a finite height of $h = 15\,\mu\text{m}$, which is smaller than the 30 µm tips used in the experiment. We thus expect to observe reflections that stem from the base. As detailed below, these reflections can be identified and neglected in the postprocessing.

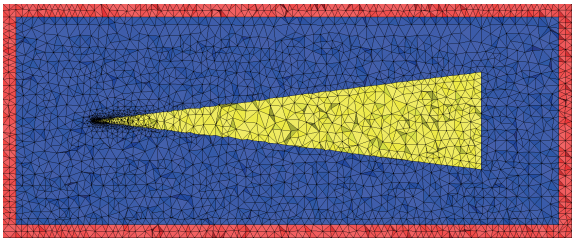

Fig. 3.10: Cross-section of the tetrahedral mesh used in the simulations. The tip is modeled as a cone (yellow) in vacuum (blue). The domain is equipped with perfectly matched layers on the outer boundaries (red).

A cross-section of the tetrahedral mesh is shown in Figure 3.10 with the metallic cone (yellow) in vacuum (blue) and the PMLs (red). The element size reduces to 1.5 nm around the apex, which has a round-off radius of 20 nm. As the induced field features high field gradients, we reduce the element size to 30 nm in the proximity of the electron trajectory to achieve a decent representation of the field. The permittivity of gold is approximated by a Drude Lorentz model of the form

$$\varepsilon(\omega) = \varepsilon_\infty - \frac{\omega_D^2}{\omega(\omega + i\gamma_D)} + \sum_L \frac{\Delta\varepsilon_L \omega_L^2}{\omega_L^2 - i\gamma_L\omega - \omega^2}.$$

With the parameters[4] stated in Tab. 3.1 we obtain a reasonable approximation of the data for gold measured by Johnson and Christy [82] over a wide range of frequencies. As already mentioned above, we expect reflections from the base of the finite cone. Figure 3.11 shows the induced field's z-component as a function of time along the electron's trajectory. x_e and y_e are kept fixed at $x_e = 950\,\text{nm}$ and $y_e = 150\,\text{nm}$. These are the raw data that we use to compute the EELP according to Eq. 3.5. At time $t = 0\,\text{fs}$ the electron is closest to the cone surface. After 50 fs the induced field has decayed by orders of magnitude. After another 50 fs we observe the reflections from the base. As these are temporally well separated from the primary fields, they can be neglected, recovering the field observed at an open tip. We found a height of $h = 15\,\mu\text{m}$ to be sufficiently large for all electron positions considered in this work.

Pole	ε_∞ or $\Delta\varepsilon$	ω_D or ω_L ($\times 10^{15}\,\text{rad}\,\text{s}^{-1}$)	γ_D or γ_L ($\times 10^{15}\,\text{s}^{-1}$)
Drude	6.39885	13.7211	0.115749
Lorentz	1.50879	4.41669	1.54401
Lorentz	1.01997	5.56004	1.82738
Lorentz	0.79923	6.71928	1.78720

Tab. 3.1: Permittivity data used in the simulation.

[4] For clarity, the quantity symbols given in the headline of the table have been changed compared to the original publication.

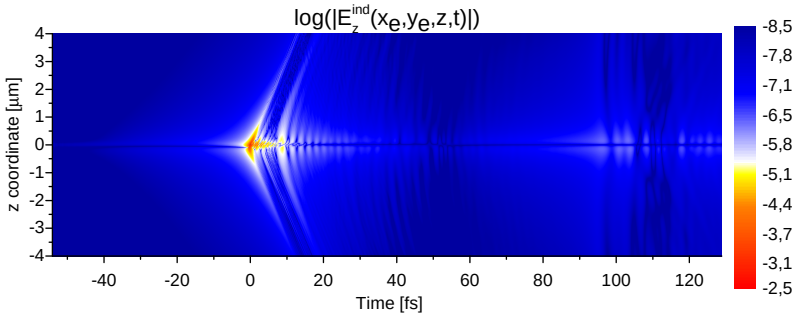

Fig. 3.11: The logarithm of the induced electric field's z component along the electron trajectory as a function of time. See text for details.

The semianalytical model

The electron energy loss have been also analyzed within a fully retarded analytical model. This model relies on expanding the induced field $\mathbf{E}^{\mathrm{ind}}(\mathbf{r},\omega)$ associated with the polarized conical metal structure in an infinite sum of independent vector harmonics:

$$\mathbf{E}^{\mathrm{ind}}(\mathbf{r},\omega) = \sum_{m=-\infty}^{\infty} \int_{-\infty}^{\infty} \mathrm{d}q \big(a_{qm}\mathbf{M}_{qm} + \bar{a}_{qm}\mathbf{N}_{qm} \big), \tag{3.6}$$

where a_{qm}, $\bar{a}_{qm}$ denote the expansion coefficients and $\mathbf{M}_{qm}$, $\mathbf{N}_{qm}$ are the vector cylindrical harmonics with m and q being the azimuthal number and the propagation constant along the cone. The expansion coefficients and the vector harmonics are analytically expressed in the Bessel and Hankel functions of the first kind [241] using the T-matrix formalism for a straight cylinder [86] and some elements of the adiabatic approaches [190, 191, 211]. Within this formalism the energy loss probability is obtained analytically by substitution of Eq. 3.6 in Eq. 3.4. A detailed description of the analytical formalism is currently in preparation for a separate publication[5].

[5] Ref. [66].

3.4 Origin of plasmonic mode structure: a comparative literature analysis

In sec. 3.3.4, we have outlined a semianalytical model (published in Ref. [66]) that calculates the energy loss probability by including the fundamental SPP mode ($m = 0$) reflected at the apex position *and* higher-order modes ($m > 0$). The total calculated loss probability $\Gamma^{\mathrm{tip}}(\omega)$ agrees very well with the experimental data (see Fig. 3.8). Figure 3.12 schematically summarizes the fundamental concept of this interpretation including the excitation of different modes and reflection causing the electron energy loss.

In this section, we address relevant information from the literature that seemingly deviate from our interpretation and which has provoked a comprehensive debate of the propagation of SPPs along nanotips. Specifically, Talebi et al. used EELS to measure plasmon maps of gold nanotips [218]. Their measurements have revealed SP maps that can be interpreted to be caused only by higher-order modes – without any fundamental mode reflection (cf. Ref. [218]). In order to unravel this difference, we recapitulate the relevant aspects of the semianalytical model in the following.

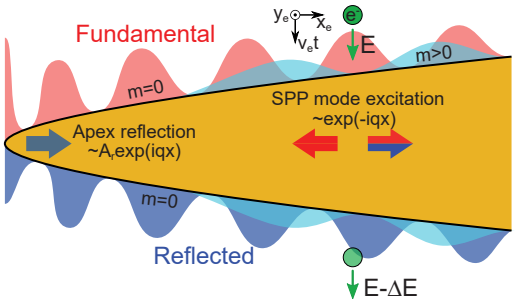

Fig. 3.12: Schematic illustration of mode excitation and electron energy loss at metal nanotips. A swift electron (kinetic energy E) polarizes the nanotip including the launching of SPPs. The fundamental azimuthal mode $m = 0$ (red) approaches the apex and is reflected with respect to a complex reflection coefficient A_r. The superposition of the fundamental, reflected and higher-order modes acts on the electron resulting in the energy loss ΔE.

The electric field that accompanies the fast electron is able to locally polarize the tip structure (cf. sec. 2.1.3). Essentially, the resulting induced field $\mathbf{E}^{\mathrm{ind}}$ can be described by cylindrical vector harmonics determined by the propagation constant $q(\omega)$ and azimuthal mode order m (cf. Eq. 3.6). We calculate the propagation constant with the adiabatic nanofocusing model and local radius $R(x)$ described in sec. 3.1. Thus, $\mathbf{E}^{\mathrm{ind}}$ becomes a function of the electron-beam position (x_e, y_e), electron velocity v_e, tip opening angle α_T and apex radius R_T. The surface bound waves with $q > k$ (SPPs) propagate in the $\pm x$-direction from the electron trajectory at position x_e (red arrows in Fig. 3.12). In general, higher-order azimuthal modes may be excited and propagate if the local radius exceeds the respective cut-off value $R(x) > R_c$. However, only the fundamental mode $m = 0$ reaches the apex from which it is reflected due to the breakdown of the adiabatic condition (blue arrow in Fig. 3.12) [200]. We assume that the higher-order modes are coupled to the far-field once $R(x)$ reduces to R_c (cf. sec. 3.1). Eventually, the complex superposition of all fields (fundamental, reflected, and higher-order) acts back on the electron leading to the loss of kinetic energy measured in the experiment [66, 74].

Mathematically, the loss probability $\Gamma_m(\omega)$ of individual modes is calculated straightforward with Eq. 3.6 inserted into Eq. 3.4. In order to consider the reflection, we incorporate a superposition of forward and backward propagating waves in the induced field [66],

$$\mathbf{E}^{\mathrm{ind}}_{m=0} \propto e^{-i\varphi_{\mathrm{spp}}(x,x_e)} + A_r e^{i\varphi_{\mathrm{spp}}(x,0)}. \tag{3.7}$$

The complex valued reflection coefficient $|A_r|e^{i\varphi_r}$ captures the reduction of the mode amplitude $|A_r|$ and includes an effective reflection point by a phase shift φ_r [233]. Moreover, the SPP waves accumulate a phase while propagating from x_2 to x_1 along the shaft, which is considered by $\varphi_{\mathrm{spp}}(x_1, x_2) = \int_{x_2}^{x_1} \mathrm{d}x\; q_{m=0}(x)$ with the fundamental propagation constant $q_{m=0}(x)$. We find the total loss probability by summing over all contributions:

$$\Gamma^{\mathrm{tip}}(\omega) = \sum_m \Gamma_m(\omega) + \Delta\Gamma_{m=0}(\omega), \tag{3.8}$$

where $\Delta\Gamma_{m=0}(\omega)$ is computed by inserting Eq. 3.7 into Eq. 3.4 [66].

For the tips analyzed in sec. 3.3, we have determined the reflection coefficient to be close to unity. Thus, the SPP waves are back propagating from the very tip end with nearly 100% efficiency leading to the standing wave pattern observed in Fig. 3.5 and Fig. 3.9.

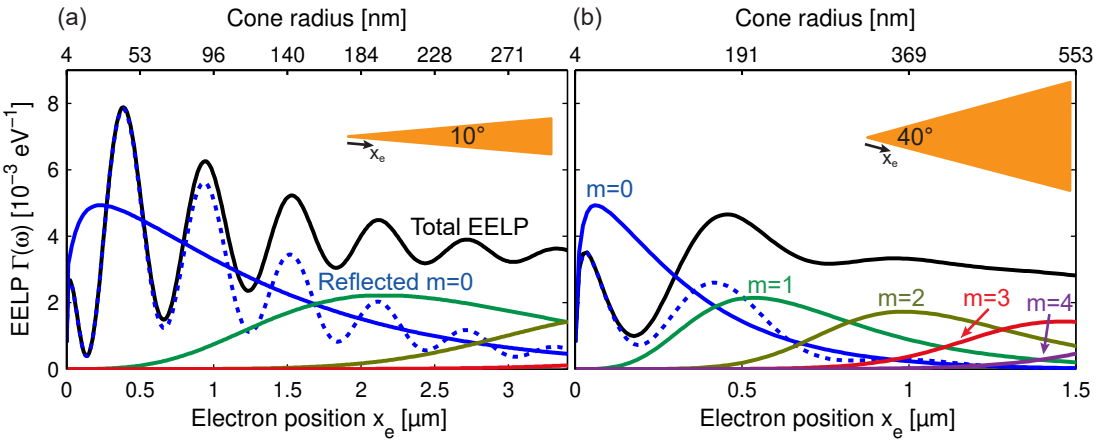

Fig. 3.13: Electron energy loss probability Γ^{tip} for gold tips with an apex radius of 10 nm and opening angles of 10° (a) and 40° (b) calculated for an energy of $\hbar\omega = 1.0\,\mathrm{eV}$ and a reflection coefficient $A_r = 1$. An oscillating signature in the total electron energy loss probability (EELP, represented by the black line) originates mainly from the reflected fundamental mode (solid and dashed blue lines) for the low-angle tip, but changes to a higher-mode dominated EELP (green to purple: $m = 1 - 4$) for high opening angles.

This fundamentally changes if the tip geometry is modified. In particular, the tip opening angle α_T has an impact on the induced field via its dependency on the local radius $R(x)$, as mentioned above. Figure 3.13 presents Γ^{tip} (calculated via Eq. 3.8) for two different opening angles of $\alpha_T = 10°$ (a) and $\alpha_T = 40°$ (b) (energy $\hbar\omega = 1.0\,\mathrm{eV}$, tip radius $R_T = 10\,\mathrm{nm}$). The oscillatory feature of the total EELP (black solid lines) is distinctly pronounced in (a), whereas it is strongly attenuated in (b). Here, the total loss due to higher-order modes

(green to purple solid lines) superimpose with the reflection contribution (blue dashed line) and dominate the total loss of kinetic energy. Furthermore, Γ^{tip} renders only small modulations for higher opening angles. Notably, this geometry dependency explains the differences in the interpretations given in this work and in Ref. [218]. We used nanotips with opening angles ranging from 11° to 14° providing a distinct reflection of the fundamental mode, whereas Talebi et al. used tips with opening angles of 19° and 49° in which reflection is strongly damped and the EELP is dominated by the local mode distribution.

In two follow-up studies Guo et al. (Refs. [217, 219]) investigated the transition from low- to high-opening angles by means of EELS and cathodoluminescence (CL) confirming the generalized interpretation of a superposition, as we have presented here. Most interestingly, they experimentally identified the breakdown of the adiabatic nanofocusing condition (Eq. 3.3) as the reason for the strong decrease of the reflection amplitude for larger opening angles: The fundamental mode radiates to the far-field, thus no electromagnetic energy is transported in a reflection process away from the apex [217]. Furthermore, higher-order modes are found to strongly couple to the far-field if the local radius $R(x)$ reaches the cut-off radius R_c – confirming the assumption made above. In conclusion, nanotips with small opening angles most efficiently waveguide SPPs and exhibit the smallest leakage radiation in the apex region. Furthermore, energy dissipation (heat) in the apex region is expected to be reduced for these tips.

CHAPTER 4

Photoemission from nanotips driven by grating-coupled surface plasmons

Metal nanotips are widely used as point-like emitters in electron-beam setups, such as electron microscope and diffraction experiments [156]. Lately, these fields benefit from the possibility of releasing electron bunches on the fs- and ps-timescale by illuminating a tip with intense laser pulses, thus facilitating time-resolved imaging and diffraction measurements [52, 54, 55, 147, 242–250]. The present chapter discusses an electron gun remotely driven by surface plasmon polaritons applicable in electron-beam instruments. In order to excite propagating SPPs a diffraction grating is milled into the tip surface by a focused ion beam a few tens of micrometer apart from the apex (cf. sec. 2.1.4 for the excitation mechanism). Subsequently, the SPPs are nanofocused into the apex region (cf. sec. 3.1) where the emission occurs due to the enhanced near-field (see sketch in Fig. 4.1). To provide a precise control of the emission site and lateral spatial spread of the emerging electron-beam, we inserted the gold tips into a modified field emitter assembly allowing for the manipulation of the electrostatic environment (sec. 4.1). Our experimental findings and analysis have been published in Ref. [67] with the title "An ultrafast nanotip electron gun triggered by grating-coupled surface plasmons" and are reprinted in sec. 4.2.

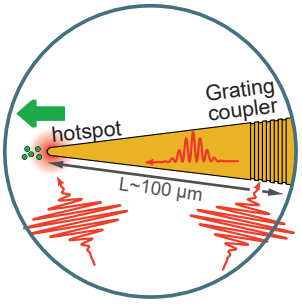

Fig. 4.1: Sketch of the experiment.

4.1 Experimental setup: site-specific photocurrent detection

As a part of the measurements discussed in the following section, an experimental setup including automated data acquisition and analysis has been established. Figure 4.2 illustrates the central aspects of the setup[1].

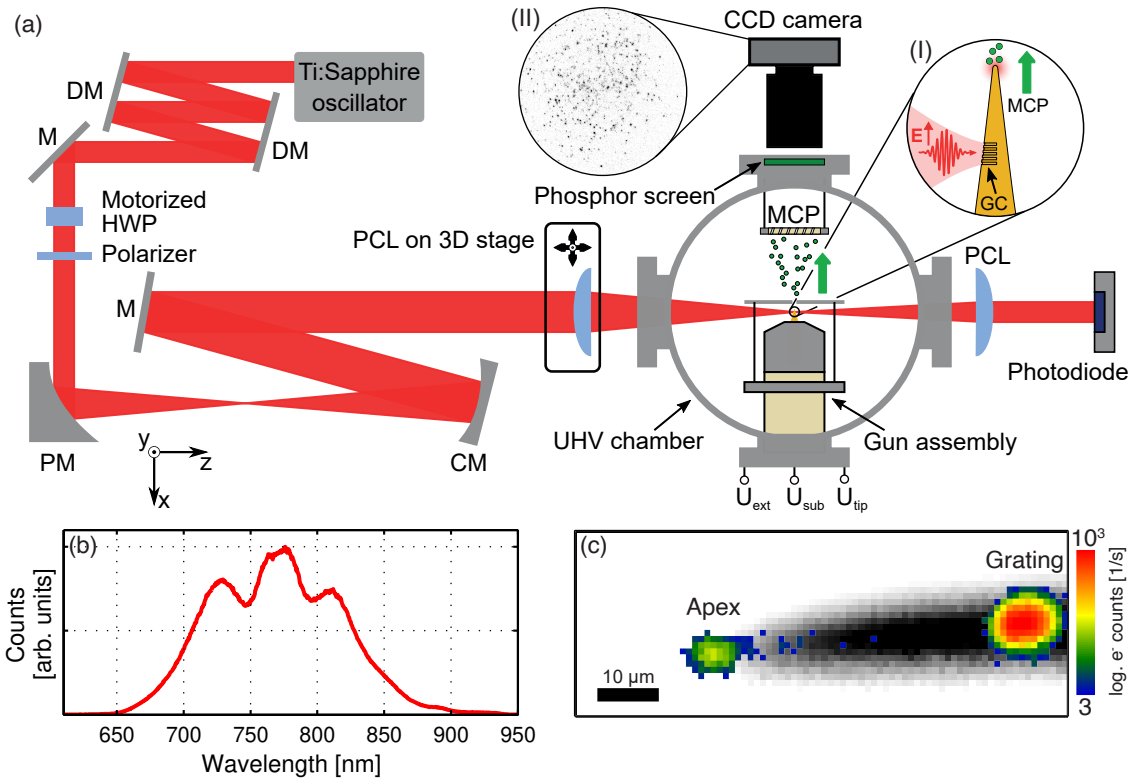

Fig. 4.2: Experiment of SPP-driven photoemission from gold nanotips. (a) Schematic illustration of the experimental setup established for the measurements. Femtosecond-pulses are guided on a gold tip with grating coupler (zoom-in in (I)) resulting in photoemission. The electron distribution is recorded with a micro channel plate (MCP) detector and camera. A typical example is shown in the inset in (II). A modified field emitter gun is used to control the electrostatic environment of the gold tips. The photodiode records the transmitted intensity (cf. shadow image in (c)). Experimental details are found in the text. Used abbreviations: silver mirror (M), dispersion compensating mirror (DM), half-wave plate (HWP), 90°-off-axis parabolic mirror (PM), concave mirror (CM), plano-convex lens (PCL), charge-coupled device (CCD), grating coupler (GC), micro channel plate (MCP), and ultrahigh vacuum (UHV). (b) Broadband laser output spectrum centered around 780 nm with a width of ~ 120 nm. (c) Shadow image of the tip (gray scale) recorded as a function of xy-focal position overlaid with the simultaneously measured electron count rate (color-coded data, logarithmic scale). This allows for a clear correlation of both signal features to the apex and grating, respectively (same data as presented in Fig. 4.5).

Ultrashort pulses with a bandwidth of ~ 120 nm are generated with a Titanium:Sapphire mode-locked laser oscillator operating at 78 MHz repetition rate (Figs. 4.2(a) and (b)). Since the photoemission yield depends critically on the pulse duration, we compensate the dispersion due to propagation in air and through optical components by using a pair of chirped mirrors (a pulse duration of 20 fs at the tip apex is estimated). The beam polarization

[1]For the sake of readability some information overlap with the brief description given in Ref. [67] (sec. 4.2).

and the laser mean power are adjusted with a half-wave plate followed by a broadband film polarizer. Unless otherwise stated, the polarization is chosen to be *p*-polarized, which corresponds to an electric field oscillating parallel to the tip's symmetry axis – a zoom-in of the tip area can be seen in the inset (I) of Fig. 4.2(a). The half-wave plate is mounted to a remote rotation stage allowing for computer controlled measurements as a function of laser power or polarization angle. In order to reduce the final spot size to a minimum of 12 µm in diameter, the original beam width is expanded by a factor of five with an off-axis parabolic and a concave reflection mirror. The focusing plano-convex lens (focal length: 100 mm) is mounted on a motorized 3D-translation stage, providing automated focal raster scans (as presented in Fig. 4.2(c) and Figs. 4.5(b) and (c)).

The laser is focused into a home-built ultrahigh vacuum (UHV) chamber equipped with four access ports (Fig. 4.2(a)): A viewport for laser beam in-coupling, an imaging micro channel plate (MCP) with phosphorus screen and camera, a photodiode in beam direction, and a gold tip integrated in a field emission gun. Electrons emitted from the nanostructure propagate to the MCP and cause an electron cascade. These electrons generate an image on the phosphorus screen that is recorded by the camera connected to the computer. A typical pattern is shown in the inset (II) of Fig. 4.2(a). Each recorded point-like spot is identified as a single electron impact event. The algorithm used to count the electron events in a dataset is briefly discussed below. During the experiments, the transmitted laser intensity is measured by a photodiode. When the focus is raster scanned across the tip area the transmitted laser intensity is reduced due to the shading by the structure. By overlaying the resulting shadow image with the position-dependent electron yield, we can identify the different emission sites (Fig. 4.2(c)). In particular, a clear assignment of the electron emission pattern to the apex and the grating is possible.

For counting the electrons distributed in the recorded images (cf. inset (II) of Fig. 4.2(a)) a computer based routine is used. The algorithm corrects the images for dead pixels and the background signal according to a reference measurement. Subsequently, an image filter with adjustable threshold value is applied that elevates the signal-to-noise ratio. Finally, the remaining light spots which have a certain pixel width given by a second threshold are counted. This ensures that only real and distinctly isolated events are detected. However, for high laser fluences and thus for dense electron distributions the algorithm is not capable to isolate the single events. Under this condition, the routine switches to an intensity integration to determine the electron count rate. The conversion factor – how much intensity corresponds to one electron – is determined via a reference measurement.

The key element of the experiment is the gun assembly, since it allows to control the active emission sites along the tip by manipulating the electrostatic environment of the nanostructure. Gold tips with a grating coupler are integrated in a modified TEM field emitter (main components are indicated in Fig. 4.3(a) and the left panel of (e)). An optical microscope is used during the delicate installation of the tip in the suppressor ((b) and (c)). Subsequently,

the integrity and centricity are checked with scanning electron microscopy imaging (d).

The suppressor and the tip electrostatic potentials are adjusted by computer controlled high voltage supplies (throughout the experiments, the extractor electrode is grounded, $U_{\mathrm{ext}} = 0\,\mathrm{V}$). We can precisely control the photoemission along the tip axis by varying the static fields in the emitter assembly. To discuss this mechanism, we deploy a simple model in which the suppressor, the apex, and the extractor electrodes are represented by parallel capacitor plates (Fig. 4.3(e), cf. also Ref. [251]). In this framework, we can distinguish an electrostatic field extracting charge carriers from the tip towards the detector and a field that suppresses the charge carriers back into the nanostructure (two different field scenarios are illustrated in Figs. 4.4(b) and (c)).

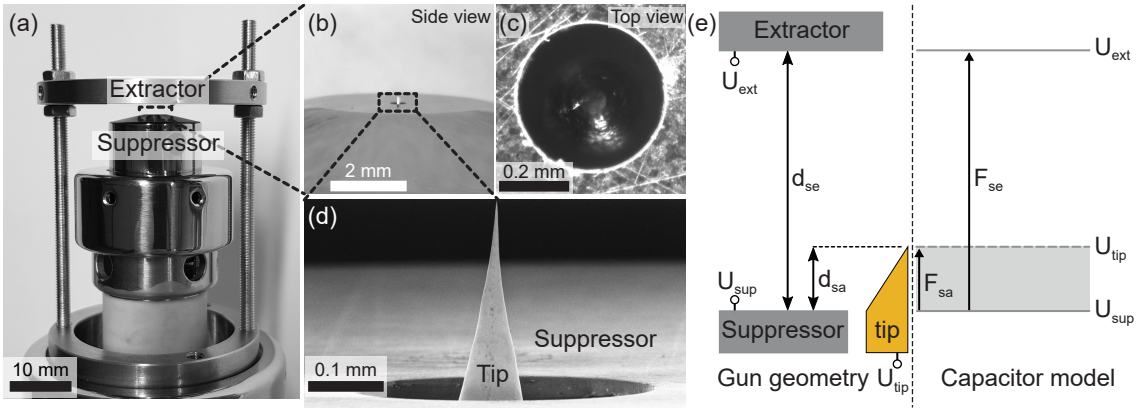

Fig. 4.3: Electron gun assembly for emission control. (a) Photograph of the modified TEM field emitter with the suppressor unit and extractor electrode. A concentric 3 mm aperture (not visible) allows for the electron transmission through the extractor. (b,c) Optical micrographs of the side (b) and top view (c) of the suppressor unit during the tip installation. In order to thread in the 250 µm gold tip into the 400 µm suppressor aperture a centering device was used. (d) Scanning electron micrograph demonstrating the tip integrity after the tip installation. (e) Schematic of the geometry of the field emitter (left panel) and plate capacitor model (right panel) with the respective applied voltages.

The applied voltages determine the field-reversal point, which is the transition from extraction to suppression of photo emitted electrons. It can be characterized by the dimensionless parameter Γ [252], i.e., the ratio of the virtual forces F_{sa} and F_{se} acting on electrons emitted from the tip (gray shaded area in the right panel of Fig. 4.3(e)):

$$\Gamma = \frac{F_{\mathrm{sa}}}{F_{\mathrm{se}}} = \frac{(U_{\mathrm{tip}} - U_{\mathrm{sup}})d_{\mathrm{se}}}{(U_{\mathrm{ext}} - U_{\mathrm{sup}})d_{\mathrm{sa}}},$$

where d_{se} and d_{sa} are the distances indicated in (e). According to the value of Γ, we distinguish three domains. For values of $\Gamma < 1$ the field reversal-point is shifted along the tip axis and photoelectrons between its position and the apex are extracted ($F_{\mathrm{se}} > F_{\mathrm{sa}}$). At $\Gamma \approx 1$ the emission site is restricted to the tip end and for $\Gamma > 1$ photoelectron emission is completely suppressed ($F_{\mathrm{se}} < F_{\mathrm{sa}}$).

4.2 An ultrafast nanotip electron gun triggered by grating-coupled surface plasmons

Benjamin Schröder, Murat Sivis, Reiner Bormann, Sascha Schäfer, and Claus Ropers
Applied Physics Letters **107** (2015), 231105[2]
DOI: 10.1063/1.4937121

Abstract We demonstrate multiphoton photoelectron emission from gold nanotips induced by nanofocusing surface plasmons, resonantly excited on the tip shaft by a grating coupler. The tip is integrated into an electron gun assembly, which facilitates control over the spatial emission sites and allows us to disentangle direct grating emission from plasmon-triggered apex emission. The nanoscale source size of this electron gun concept enables highly coherent electron pulses with applications in ultrafast electron imaging and diffraction.

The field of plasmonics has established a wide range of approaches to cast a free electron gas in designed geometries for a controlled collection, guiding and concentration of light on the nanoscale [21, 22, 25, 37, 73]. As a prominent example, nanofocusing harnesses both the waveguiding and sub-wavelength localization capabilities of plasmonic excitations, by converging propagating surface plasmon polaritons (SPPs) on tapered conical structures in an intense near-field at the cone apex [35, 36, 41, 45, 65, 110, 128, 129, 183, 188, 190, 191, 203, 204, 208]. This optical hot spot locally drives multiple linear and nonlinear processes [110, 128, 129, 203], which have given rise to applications in near-field scanning optical microscopy (NSOM) and spectroscopy [36, 41, 45, 188, 203, 204, 208]. Grating-coupling has proven as a very efficient means to launch surface plasmons on metal nanotips [128], and it allows for a spatial separation of the in-coupling location from the plasmonic focus. Initially designed to reduce background signals in NSOM and to avoid direct sample excitation, the scheme is particularly suited for inducing highly nonlinear optical processes, such as multiphoton photoemission [104, 163]. Localized photoelectron emission from a nanoscale apex [104–106, 163, 165–172, 177, 253, 254] is of great importance for future developments in the field of time-resolved electron imaging and diffraction [248, 255–262]. First applications have utilized the unique beam properties of tip-based photoelectron sources [263, 264] in ultrafast transmission electron microscopy (UTEM) [146], ultrafast low-energy electron diffraction (ULEED) [55] and femtosecond point-projection microscopy (fs-PPM) [249, 265], with a recent PPM implementation based on plasmonic nanofocusing [50]. Whereas lensless imaging approaches make use of nanoscale source sizes, the full capabilities of coherent electron pulses, including nanoscale probing and phase contrast imaging, can be most efficiently harnessed in a UTEM setting. Thus, it is highly desirable to combine a plasmonic

[2]Reprinted from Appl. Phys. Lett. **107**, 231105 (2015), with the permission of AIP Publishing.

nanofocusing source with a gun environment compatible with electron microscopy.

Here, we demonstrate multiphoton photoemission from the apex of a gold nanotip driven by resonant femtosecond excitation of surface plasmons in a grating coupler on the tip shaft. The emitter is integrated in a modified field emission gun allowing for a detailed characterization and control of the active emission sites. In this setup, by tailoring the electrostatic field around the tip, electron emission from the apex, grating and shaft can clearly be distinguished. The ultrafast electron source developed here will be applicable in a variety of time-resolved electron imaging approaches.

In the experiments (schematic of the setup shown in Fig. 4.4), optical excitation is provided by a mode-locked Ti:Sapphire laser oscillator (center wavelength 800 nm, pulse duration 10 fs, repetition rate 78 MHz). The laser beam is focused onto the gold nanotip (spot diameter of 12 µm) by a plano-convex lens mounted on a three-dimensional translation stage. The power and polarization of the laser beam are controlled by a $\lambda/2$-waveplate and a broadband polarizer. Sharp gold tips are fabricated by electrochemical etching of thermally annealed gold wires (0.25 mm diameter) in hydrochloric acid (for a detailed description of the fabrication process, see, e.g., Refs. [41] and [45]). To facilitate efficient SPP excitation, a resonant grating structure is milled into the shaft by focused ion beam etching. The grating is placed 45 µm from the apex, allowing for a separate excitation of both regions. Figure 4.5(a) displays a scanning electron micrograph of one of the measured gold tips with an apex radius of curvature of 22 nm and a grating periodicity of 800 nm. The nanostructured tip is built into a field emission gun comprising a suppressor and extractor unit installed in an ultrahigh vacuum chamber (operating pressure in the 10^{-9} mbar range). Distributions of emitted electrons are recorded by an imaging micro channel plate (MCP) detector and a charge-coupled device (CCD) camera.

We have observed grating-induced multiphoton photoemission from multiple nanostructured tips. Both the high nonlinearity of the emission (a four-photon process is expected from the excitation wavelength and the gold work function [104]) as well as the polarization dependence of the grating coupler are evident from a measurement of the photocurrent as a function of waveplate angle $\alpha/2$ (Fig. 4.4(d)). We find maximum emission for p-polarization (electric field perpendicular to grooves), in agreement with recent observations [50], and the shape of the polar plot exhibits an effective nonlinearity in intensity of $n = 3.4$ (red line corresponds to a $\cos^{2n}(\alpha + \phi)$ dependence with $\phi = 4°$). A more direct measurement of the effective nonlinearity of the emission process will be presented below.

Recording electron emission patterns yields information about the total current generated by optical excitation at the focal position. The present structure is designed to produce electron emission in the apex region, which is substantially removed from the optical excitation position at the grating. In order to distinguish direct photoemission at the focal position from plasmon-mediated emission, we manipulate the electrostatic environment of the field emitter geometry. As we will demonstrate, this allows for the suppression of emission di-

rectly from the grating while retaining apex emission induced by grating-coupled surface plasmons.

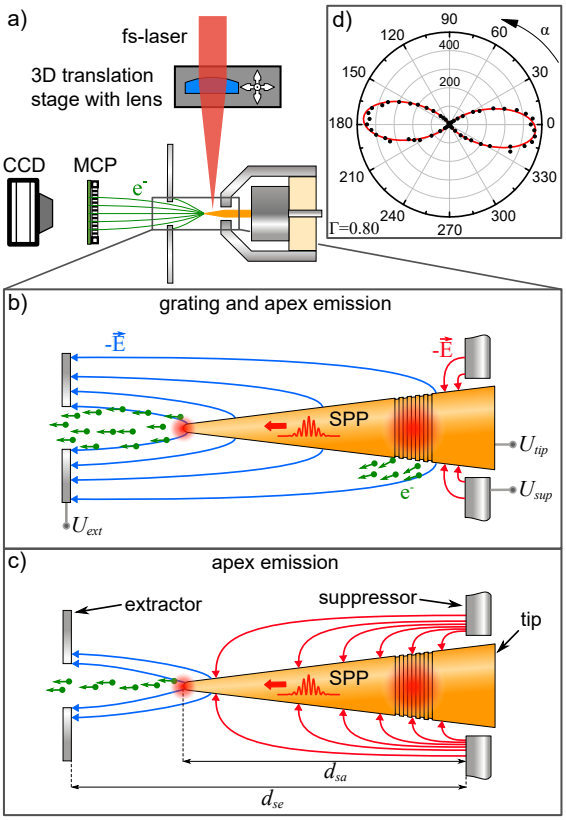

Fig. 4.4: Schematic of the experimental setup. (a) The excitation laser is focused onto the nanostructure by a plano-convex lens (focal length: 100 mm) mounted on a translation stage. Emitted electrons are detected by an MCP and CCD camera. The gold tip is inserted into a suppressor-extractor-geometry allowing for separate tuning of the static potentials of the tip (U_{tip}), suppressor (U_{sup}) and extractor (U_{ext}) electrodes. (b) Schematic field line distribution for a voltage setting resulting in electron extraction from the entire tip (blue lines). (c) A more negative suppression voltage prevents emission (red lines) from the grating and shaft. Any electron emission observed under these conditions, e.g., upon grating excitation, must stem from regions close to the apex. (d) Electron rate (s^{-1}) as a function of polarization angle α upon grating illumination (average power: 14.5 mW, waveplate is rotated between 0° and 180°). ($d_{\mathrm{se}} = 1.44$ mm and $d_{\mathrm{sa}} = 0.29$ mm, distance between MCP and tip apex: 36 mm, MCP diameter: 26 mm, extractor aperture diameter: 3 mm)

Specifically, for given tip (U_{tip}) and extractor (U_{ext}) voltages, the suppressor voltage (U_{sup}) defines a point along the tip axis, at which the electric field changes its sign. On the left side (towards the apex) of this field-reversal point or cut-off position, electrons are effectively extracted, whereas emission is suppressed towards the shaft (compare Figs. 4.4(b) and (c)). By variation of the suppressor voltage, the field-reversal point can be continuously shifted across the grating and shaft. Note that the static extraction fields always remained below the onset of field emission (finite element simulations yielded fields of $0.1 - 0.4\,\mathrm{V/nm}$).

Figures 4.5(b) and (c) show color-coded maps of the electron count rate as a function of the laser focus position in the xy-plane (same area as shown in Fig. 4.5(a)), obtained by raster scanning the lens position. Here, Fig. 4.5(c) corresponds to a voltage setting with suppression of direct emission from the grating (cut-off point between apex and grating), whereas grating emission is permitted in Fig. 4.5(b) (cut-off point on the right of the grating). In both measurements, two clear positions of enhanced electron count rates are recorded, corresponding to an excitation either on the apex or on the grating. Illumination on smooth parts of the shaft results in smaller rates with a Γ-dependent spatial distribution.

The precise location of the field-reversal point is identified by measuring line scans in the xy-plane (dashed line in Fig. 4.5(c)) for a range of suppressor voltages, as demonstrated in Fig. 4.6. In this figure, the variation of the suppressor voltage (vertical scale) is represented

by using a dimensionless parameter Γ, defined as [252]

$$\Gamma = \frac{(U_{\mathrm{tip}} - U_{\mathrm{sup}})}{(U_{\mathrm{ext}} - U_{\mathrm{sup}})} \frac{d_{\mathrm{se}}}{d_{\mathrm{sa}}}.$$

Here, d_{sa} and d_{se} are the distances from the apex and extractor to the suppressor, respectively (cf. Fig. 4.4(c)). Complete suppression of photoelectrons from the tip is given for a Γ value on the order of unity (field-reversal point crosses the apex) with a precise value depending on the specific geometry. For decreasing Γ, the field cut-off is shifted from the apex towards the suppressor, widening the region where photoelectrons can be extracted. Figure 4.6(b) shows a Γ-dependent map of line scans exhibiting various features, which are assigned to particular emission regions in the schematic shown in Fig. 4.6(a).

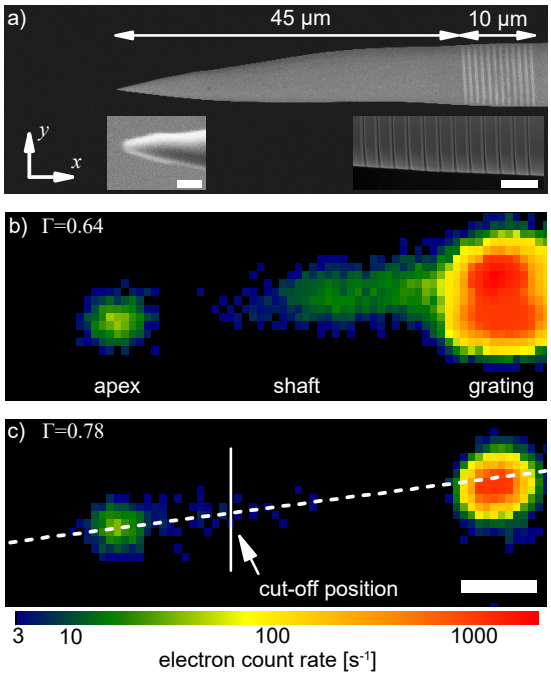

Fig. 4.5: (a) Scanning electron micrograph of the tip including the nanofabricated grating (12 grooves, 200 nm width, 500 nm depth). Insets: (left) apex region (scale bar: 100 nm), (right) closeup of the grating region (scale bar: 2 µm). (b,c) Color-coded maps of the detected electron count rate (logarithmic scale) as a function of the focal position in the xy-plane, obtained by raster scanning the lens (polarization parallel to tip axis ($\alpha = 0$), average laser power: 17 mW). (b) A suppressor voltage of $U_{\mathrm{sup}} = -460$ V ($\Gamma = 0.64$) allows for electron emission from the apex, shaft and grating regions (compare Fig. 4.4(b)). (c) A more negative suppression voltage ($U_{\mathrm{sup}} = -475$ V, $\Gamma = 0.78$) leads to a cut-off position between the apex and grating, as indicated by the white vertical line. The measurement shown in Fig. 4.6(b) is recorded along the white dashed line in (c). Scale bar: 10 µm. Throughout all measurements, the tip and extractor voltages are kept constant at $U_{\mathrm{tip}} = -400$ V and $U_{\mathrm{ext}} = 0$ V, respectively.

The photoemission map reveals three prominent contributions: Two vertical lines with the excitation positioned at the apex and the grating, respectively, and a diagonal stripe extending throughout the shaft and grating regions. The signal from direct apex excitation is nearly constant as a function of Γ. For $\Gamma_a = 0.83$, the field-reversal point reaches the apex position ($x = 0$) and suppresses the emission. Consistently, a linear trend of the upper edge of the diagonal shaft feature is observed: It marks the Γ-dependent shift of the cut-off position $x_{\mathrm{cut}}(\Gamma)$, which jointly terminates with the apex signal, i.e., $x_{\mathrm{cut}}(\Gamma_a) = 0$. Most importantly, upon grating excitation (vertical line on the right), electrons are also detected up to values of $\Gamma = \Gamma_a$, although direct photoemission from the grating region is suppressed for $\Gamma \geq 0.7$, the value at which the cut-off position reaches the grating. We can therefore conclude that grating illumination results in electron emission from the apex, mediated by resonant SPP excitation.

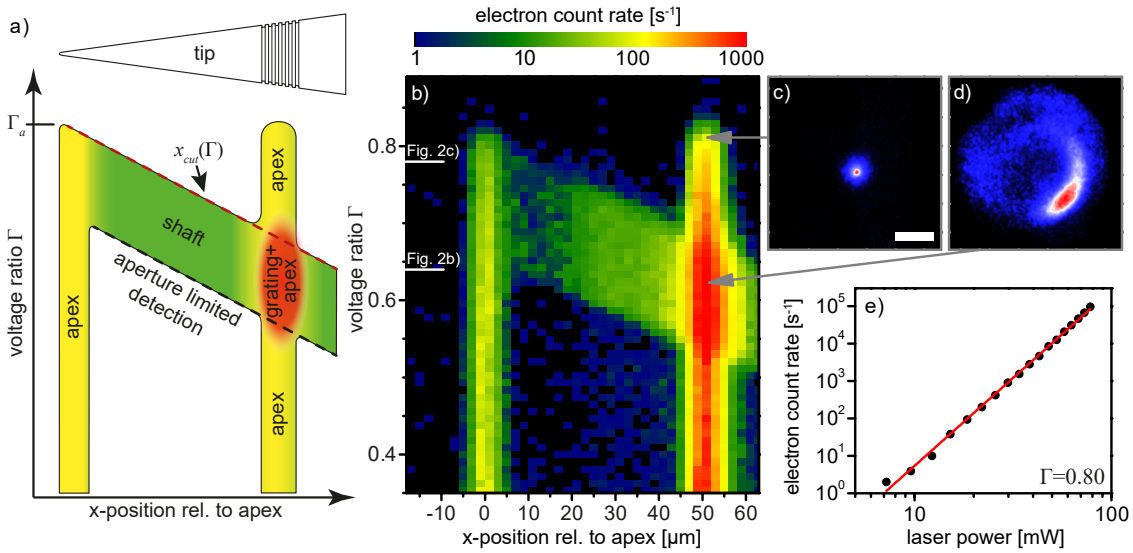

Fig. 4.6: (a) Schematic assignment of features in position- and Γ-dependent electron emission (see experimental data in (b)) to specific regions of emission. (b) Color-coded map of the electron count rate (logarithmic scale, integrated over detector area, average laser power: 17 mW) as a function of Γ and focal spot position (scan line: cf. Fig. 4.5(c)). Vertical lines correspond to excitation on the apex ($x = 0$) and grating ($x = 50$ µm). The Γ-dependent shift of the cut-off position on the shaft causes the diagonal stripe. Direct emission from positions to the right of the cut-off line (see $x_{\mathrm{cut}}(\Gamma)$ in (a)) is suppressed. The observation of strong emission for grating excitation and at large Γ (up to apex suppression at Γ_a) thus demonstrates that these electrons are emitted at the apex. (c) Recorded electron image for $\Gamma \approx \Gamma_a$ exhibiting a focused spot (diameter 0.7 mm (full-width-half-maximum), scale bar: 5 mm). (d) For $0.55 < \Gamma < 0.7$, the pattern is composed of a largely uniform distribution from the apex, and shaft/grating electrons forming an arc-shape (bottom right). The electron images correspond to planes perpendicular to the tip axis. From this viewing direction, the grating is located on the right. (e) Nonlinear power-dependence of the electron current. Approximately 10^5 electrons/s are detected at an incident power of 78 mW. An effective nonlinearity of 4.7 (red line) is observed.

Besides the selection of possible emission regions, it should be noted that Γ also has a pronounced effect on the trajectories of emitted electrons. In particular, for increasing Γ-values, the electrostatic field close to the apex acts as a focusing lens, which can be demonstrated by considering the spatial emission patterns for different conditions. Figures 4.6(c) and (d) display recorded images under grating excitation and for Γ values below (d) and near (c) the apex cut-off Γ_a (see arrows in Fig. 4.6(b)). In Fig. 4.6(d), two contributions are found, namely an arc-shaped distribution of electrons directly emitted from the grating and a largely uniform distribution from apex electrons. Increasing Γ towards Γ_a reduces the radius of the arc feature until it vanishes (near $\Gamma = 0.7$). Upon approaching Γ_a, also the apex contribution is focused to a narrow spot (see Fig. 4.6(c)). The present setup is not able to quantitatively determine beam parameters such as brightness and emittance [252]. These quantities will be subject to investigation in the tip-based ultrafast transmission electron microscope we recently developed [146]. (The Supplemental material[3] provides a movie of the spatial electron patterns for grating illumination, recorded as a function of Γ.) The

[3] See Supplemental material at http://dx.doi.org/10.1063/1.4937121 for a movie of the electron distributions upon grating illumination, recorded as a function of Γ.

focusing action of the suppressor additionally causes the lower edge of the diagonal stripe feature. Specifically, for a given emission position, a certain focusing and thus a threshold value of Γ is required to collect the electrons by the finite solid angle of detection. Below this threshold, electron paths are cropped by the MCP aperture. For completeness, in Fig. 4.6(b), we label those Γ values at which the two-dimensional scans in Figs. 4.5(b) and (c) are recorded.

As photoemission currents from the tip end are generated for both direct apex illumination and grating illumination (currents denoted by I_{ap} and I_{gr}, respectively), it is interesting to consider the relative electron yields $I_{\mathrm{gr}}/I_{\mathrm{ap}}$ for these two forms of excitation. In all our experiments, we obtained substantially higher emission upon grating excitation. At the conditions from Fig. 4.5, which were chosen to show both direct apex emission and grating-mediated emission, about 20 times more electrons from the apex are emitted upon grating illumination, similar to recent results [50]. However, it should be noted that the specific focusing conditions, including wavefront tilt and curvature, strongly influence the mode overlap and thereby the specific relative emission yield. For optimized grating coupling, we achieved a ratio of $I_{\mathrm{gr}}/I_{\mathrm{ap}}$=150. This enhancement clearly results from superior mode-matching between the far-field radiation and the extended grating [266], as compared to direct apex excitation, and it may be used to estimate the resulting local intensities in both scenarios. To this end, we first have to determine the effective nonlinearity of the photoemission process. Figure 4.6(e) shows in a double-logarithmic plot the photocurrent from the apex as a function of laser power incident on the grating. A current of $I_{\mathrm{gr}} \approx 10^5$ electrons/s is obtained for a power of $P = 78\,\mathrm{mW}$, and the current scales with an effective nonlinearity $n = 4.7$, i.e., $I_{\mathrm{gr}} \propto P^n$ (solid red line), close to the expected value of 4. Thus, the field strength obtained at the apex for grating illumination exceeds that for direct illumination by a factor $(150)^{1/2n} \approx 1.7$ (a value of 1.32 was given in Ref. [50]). Employing the emission current from the smooth shaft as a reference, field enhancement factors (defined as local apex field strength over incident field strength) for both excitation conditions can be estimated, and we find apex field enhancements of 6.4 and 3.8 for grating and direct illumination, respectively. In order to derive a normalized quantum efficiency of the nonlinear photoemission process from the measurements, we describe the total emitted charge as $Q = A\tau(s_n I_\omega)^n$, where A is the apex area, τ is the pulse duration at the apex (estimated to about 20 fs on the apex, influenced by some resonance narrowing [128] and minor SPP group-velocity dispersion [45, 224]), I_ω is the local intensity, and s_n is a coefficient containing the quantum efficiency of the multiphoton process at the measured effective nonlinearity n. Using this relation and the experimental parameters, we obtain a value[4] of $s_n = 2.3 \times 10^{-15}\,(\mathrm{A/nm^2})^{1/n}\,\mathrm{cm^2/W}$ for $n = 4.7$.

In conclusion, we demonstrated site-sensitive multiphoton photoemission from a sharp

[4] We obtain similar values of $s_n = 2.7 \times 10^{-15}\,(\mathrm{A/nm^2})^{1/n}\,\mathrm{cm^2/W}$ with $n = 4.5$ and $s_n = 2.8 \times 10^{-15}\,(\mathrm{A/nm^2})^{1/n}\,\mathrm{cm^2/W}$ with $n = 5$ for the data reported in Refs. [50] and [105], respectively, although this may not be expected for Ref. [50] given the very different photon energies used.

gold nanotip equipped with a resonant grating structure. In the experiments, the tip was integrated into an extractor-suppressor-type gun assembly, which is fully compatible with existing transmission electron microscope geometries and allows for manipulating the electrostatic environment of the tip. In this way, a confinement of the photoemission to a very small apex region and a complete suppression of electron emission from the grating is achieved. Concerning future applications of the presented source concept in ultrafast electron microscopy and diffraction, this control over both the transversal beam properties and the local extraction fields will be highly beneficial, e.g., by electron-beam collimation and by alleviating space charge problems from non-localized shaft emission. More generally, we believe that the photoemission induced by tailored plasmonic fields presents a powerful new degree of freedom to shape complex electronic wavefronts with well-defined linear and angular momentum distributions.

We gratefully acknowledge funding by the Deutsche Forschungsgemeinschaft (DFG) (SFB-1073, projects A5 & C4). We thank Karin Ahlborn for help in tip fabrication.

CHAPTER 5

Photoelectron transfer in an STM tunnel contact

A nanotip located at a (sub)-nanometer distance to a sample surface (tip-sample contact) represents a widely applicable model system that comprises scanning tunneling and atomic force microscopy (STM and AFM) including their diverse atom-level imaging and spectroscopy modes [267]. The combination of these scanning probe techniques with a (pulsed) laser excitation may join atomic resolution with light-based schemes (e.g., pump-probe approaches and nonlinear responses), thus consolidating to a powerful toolbox containing current, field and photon excitations. Indeed, several promising approaches have been addressed, such as time-resolved modes of STM and AFM operating far beyond the electronic bandwidth of these systems [60–62, 268–270], apertureless near-field scanning optical microscopy (A-NSOM) [43, 44, 102, 183, 271, 272], or tip enhanced Raman spectroscopy (TERS) [47–49]. In this context, laser-driven plasmonic near-fields present in a metal-metal junction play an outstanding role due to their ability to strongly concentrate and enhance the light in the gap region between the tip and the sample (see sketch in Fig. 5.1) [33, 273, 274]. Hence, an optical excitation of isolated features on the substrate surfaces and the investigation of their dynamics and nonlinear energy pathways (for example, multiphoton absorption) may be possible [29, 30, 275].

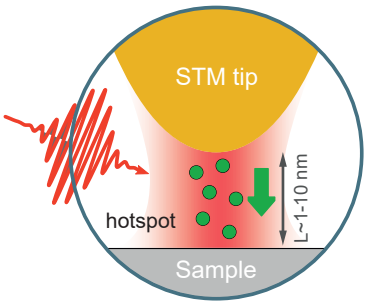

Fig. 5.1: Sketch of the experiment.

In this chapter, we analyze nonlinear electron transport channels opened by fs-laser illumination of the nanometric tunnel contact in an STM. Specifically, the exceptional precision of the gap width (tip-sample distance) provided by the STM allows to measure current-distance dependencies ($I(z)$ curves) which reveal characteristic photocurrents driven by the near-field *and* distinctly depending on the specific potential barrier in the tunnel gap. In the following section, we start with a classical description of a coupled dipole model (CDM) that provides a general picture of the surface plasmon mode formed in the STM contact region. In particular, the gap width dependency of the near-field and its lateral locality is discussed. We also address the limits of the classical CDM when approaching gap distances on a nanometer scale as present in the STM. Subsequently, an electron transport model based on the Bardeen tunnel theory is introduced that explicitly includes the electron wave functions (sec. 5.2). Both – the CDM and the Bardeen model – are used in sec. 5.3 to disentangle the different (near-field-driven) contributions to the measured $I(z)$ curves and to provide insights into the underlying physical mechanisms. The results have been published in Ref. [68] with the title "Controlling photocurrent channels in scanning tunneling microscopy". The final section 5.4 presents valuable aspects of the technically challenging realization of the combination of an STM with a fs-laser.

5.1 Plasmonic near-field coupling in a tip-sample gap

The near-field of a tip interferes with the optical response of the sample forming a plasmonic gap mode with a pronounced dependency on the tip-sample distance z_{gap} and tip apex radius R_T [276]. A commonly applied approximation bases on a simple coupled dipole model. Figure 5.2(a) schematically shows the CDM applied to a tip-sample system.

The light excites an oscillating dipole moment $\mathbf{p}_t$ in the tip apex approximated as a sphere, which in turn generates a polarization in the semi-infinite material represented by the image dipole moment of the sample, $\mathbf{p}_s = (\varepsilon_s - \varepsilon_d)/(\varepsilon_s + \varepsilon_d)\mathbf{p}_t = \beta_s \mathbf{p}_t$. The back action on the tip results in the total near-field given by the superposition of the incident and dipolar fields [72, 277]. Referring to sec. 2.1, we stay in the quasi-static approximation (tip radius R_T and tip-sample distance z_{gap} are small compared to the excitation wavelength $\lambda = 2\pi c/\omega$) and use an excitation wave polarized in the z'-direction, $\mathbf{E}_0 \exp(-i\omega t)$. The superposition of both – the external and the image field at the position of the sphere center – leads to the total dipole moment of the tip-sample system, $\mathbf{p}(t) = \varepsilon_0 \varepsilon_d \alpha_\omega^{\mathrm{eff}} \mathbf{E}_0 \exp(-i\omega t)$, expressed by the effective polarizability [278],

$$\alpha_\omega^{\mathrm{eff}} = \alpha_\omega (1 + \beta_s) \left(1 - \frac{\alpha_\omega \beta_s}{16\pi (R_T + z_{\mathrm{gap}})^3} \right)^{-1} . \tag{5.1}$$

The polarizability of a sphere α_ω is given by Eq. 2.2. Dipole near-fields $\mathbf{E}_{\mathrm{nf}}^t$ and $\mathbf{E}_{\mathrm{nf}}^s$ of the tip and the spherical image charge in the sample calculated with Eq. 5.1 superimpose to the

total field for $z' > 0$ [72],

$$\mathbf{E}^{\text{out}}(\mathbf{r},t) = \mathbf{E}_0 e^{-i\omega t} + \mathbf{E}^t_{\text{nf}}(\mathbf{r},t) + \beta_s \mathbf{E}^s_{\text{nf}}(\mathbf{r},t). \tag{5.2}$$

Using the CDM for a gold particle with a radius $R_T = 10\,\text{nm}$ in front of a copper surface ($\lambda = 800\,\text{nm}$) shows a monotonically increasing field enhancement,

$$F = \frac{|\mathbf{E}^{\text{out}}|}{|\mathbf{E}_0|} \sim (z_{\text{gap}} + R_T)^{-3},$$

in the gap region with a decreasing tip-sample distance z_{gap} (Fig. 5.2(c)). For a very close proximity, the field at the apex (solid red line) and at the sample surface (dashed red line) are the same ($F \approx 12.7$), whereas larger gap distances lead to much higher fields at the apex ($F \approx 6.1$) compared to the surface ($F \approx 2.3$).

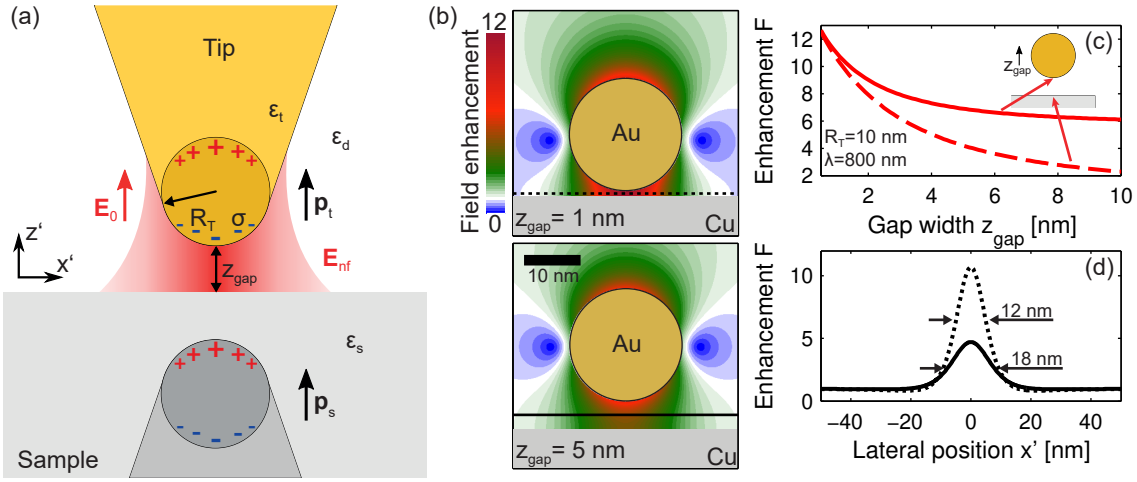

Fig. 5.2: Coupled dipole model (CDM). (a) Schematic illustration of a tip apex (ε_t) modeled as a sphere of radius R_T in proximity to a flat sample surface (ε_s) (gap distance z_{gap}, dielectric environment (ε_d)). The illumination with a plane wave $\mathbf{E}_0$ polarized in the z'-direction induces a dipole $\mathbf{p}_t$ in the tip which in turn induces an image dipole in the sample $\mathbf{p}_s$. A near-field $\mathbf{E}_{\text{nf}}$ follows from the back action of $\mathbf{p}_s$ on the tip (details in the text). (b) Field enhancement maps $F = |\mathbf{E}^{\text{out}}|/|\mathbf{E}_0|$ calculated with the CDM for $z_{\text{gap}} = 1\,\text{nm}$ (top panel) and $z_{\text{gap}} = 5\,\text{nm}$ (bottom panel) demonstrate a strongly increased field in the gap region for the smaller tip-sample distance. (c) F as a function of gap width for the two $x'z'$-locations (0,0) (dashed red line) and $(0, z_{\text{gap}})$ (solid red line). The inset illustrates these positions and the change of the gap width by retracting the sphere. (d) Field enhancement for the constant gap widths of 1 nm and 5 nm along the dashed and solid black lines in (b), respectively. The lateral confinement is indicated as the spread at full-width at half-maximum. Dielectric functions of gold (Au) and Copper (Cu) are taken from Ref. [82] at $\lambda = 800\,\text{nm}$ (1.55 eV) ($\varepsilon_d = 1$).

Furthermore, the tip-sample interaction has a striking impact on the field localization in the gap region (Figs. 5.2(b,d)). The lateral spread of the field along the x'-axis in the gap center (indicated by the black lines in (b)) decreases from 18 nm ($z_{\text{gap}} = 5\,\text{nm}$) to 12 nm ($z_{\text{gap}} = 1\,\text{nm}$) full-width at half-maximum. This is accompanied by an intensity localization proportional to $\sqrt{R_T \cdot z_{\text{gap}}}$ [279] and enables a lateral resolution of $\lesssim 10\,\text{nm}$ in A-NSOM experiments [43–46]. Similar to the Fröhlich equation in sec. 2.1, a resonance condition can

be derived for the coupled system as a function of the gap width demonstrating a red-shift when the sphere approaches to the surface [280, 281]. In comparison to a single sphere (cf. Figs. 2.2(b) and (c) in sec. 2.1), we can conclude that the field enhancement and field localization are higher in the gap region for coupling dipoles.

There is a wide range of theoretical studies exploring more realistic tip-substrate systems compared to the CDM (e.g., Refs. [89, 92, 96, 277, 280, 282–287]). Most importantly, the algebraic relation for the near-field as a function of the tip-sample distance and the apex radius found with the CDM (Eq. 5.1 and Eq. 5.2) is also demonstrated with finite-element nanotip-substrate simulations [96, 285, 287]. However, according to these classical calculations F can reach a number of several hundred for gap widths in the nanometer range [96]. In fact, the near-field is infinitely enhanced when z_{gap} converges to zero; this unrealistic situation is prevented by considering quantum effects for small values of z_{gap}.

Quantum effects in nanometric tip-sample gaps

Gap dimensions in the (sub)-nanometer regime are affected by the quantum nature of the conduction electrons [288, 289]. Specifically, this limits the field enhancement for gap distances approaching zero [290]. The probability density of the electrons at the transition from matter to vacuum does not vanish abruptly, rather it decays exponentially into the vacuum – the so-called spill-out [288]. A wave function overlap of both electrodes in the gap causes electron transport due to finite quantum tunneling probabilities, hence reducing the screening surface charge distribution. This effect strongly suppresses the near-field enhancement and modifies the resonance structure in comparison to the classical prediction. For a pair of spheres in close proximity (dimer), Esteban et al. performed ab-initio calculations with time-dependent density functional theory and developed a semi-classical quantum corrected model [291]: Both approaches derive the formation of charge transfer plasmon (CTP) modes with different resonance frequencies and widths compared to the classical CDM. Importantly, the near-field enhancement factor has a global maximum limited to $F \approx 100$ at gap distances of a few Ångström [291]. Experimental evidence of the correct prediction of the CTPs has been found in the Refs. [114, 292, 293].

The prototypical system of two approaching nanostructures provides valuable, qualitative insights for the tip-surface system important in this chapter. In the following section, we discuss an alternative approach to the CTP based on the modified Bardeen theory for electron tunneling in an STM. Although it relies on a static formalism, this allows us to determine an effective electron population that results in the charge transfer driven by multiphoton absorption from the plasmonic near-field in the tunnel contact.

5.2 Electron transport in a tunnel contact

Single electron transport essentially depends on the potential energy landscape $V(\mathbf{r})$ in which the electron is moving, as schematically shown in Fig. 5.3(a). Regions where the electron energy E is smaller than the wall (hatched area) are considered as potential barriers and a transfer is prohibited in a classical picture. In the quantum description, however, the wave nature of the charge carrier represented by the wave function $\Psi(\mathbf{r}, t)$ allows for tunneling through this barrier. In other words, the electron is scattered by the barrier with specific probabilities of being transmitted or back scattered (reflected) [294].

In STM, the transmission probability T for an electron to transfer through the vacuum gap of width z_{gap} is controlled by the potential difference between both electrodes (tip and sample), i.e., the bias voltage U_B. Generally, direct analytical solutions are not available and approximations have to be developed. One prominent theoretical treatment of the quantum mechanical problem of an STM contact is provided by the modified Bardeen perturbation model that calculates the tunnel current $I(z_{\text{gap}}, U_B)$ [295]. We restrict the treatment to the one-dimensional case[1].

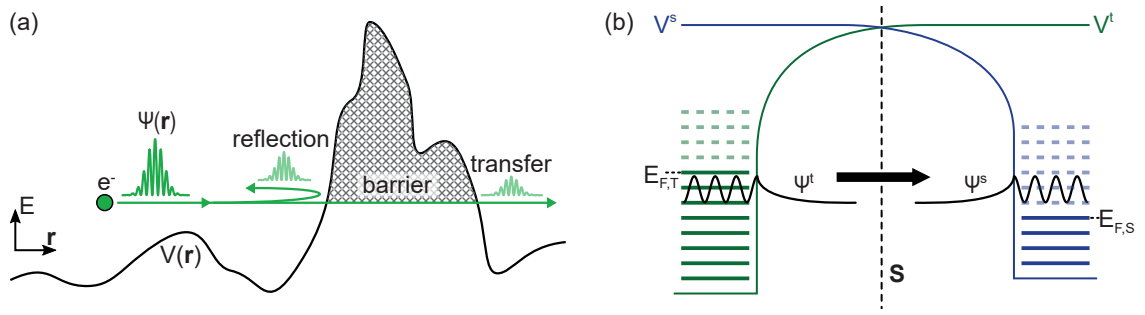

Fig. 5.3: Electron transfer through a potential barrier and Bardeen approach for tunneling. (a) An electron (e^-) represented by a wave function $\Psi(\mathbf{r}, t)$ with energy E moves in the energy landscape $V(\mathbf{r})$. Once the electron approaches a potential barrier ($V(\mathbf{r}) > E$, hatched area) it is either reflected at the barrier or transmitted through the barrier (tunneling). The transfer probability is a function of $V(\mathbf{r})$ and E. (b) For a tunnel junction in an STM, this concept can be quantitatively treated in the Bardeen approach in which the system is divided by the surface $\mathbf{S}$ into the two subsystems tip and sample that are characterized by the potentials $V^s(z')$ and $V^t(z')$. The electronic states in the tip Ψ^t and sample Ψ^s are occupied up to the the Fermi edges $E_{F,T}$ and $E_{F,S}$ (horizontal lines). A current (black arrow) can only exist for electrons from occupied to unoccupied states (dashed horizontal lines).

Electronic transport through a tunnel junction is described as the change of the initial state $\Psi_i(z', t)$ in one electrode (tip) to the final state $\Psi_f(z', t)$ in another electrode (sample). This is presented in the scheme in Fig. 5.3(b). Both are identified by their eigenvalues E_i and E_f and the transport is governed by the transfer rate $w_{if} \propto T$ (number of electrons per time). In order to calculate w_{if} and thus the total current, Bardeen splits the complete electrode-gap-electrode composite into two subsystems: the tip-gap and gap-sample system separated by a barrier surface $\mathbf{S}$. The solutions of the stationary Schrödinger equation of

[1] A detailed discussion including the generalization to the three-dimensional case can be found in Ref. [296] or Ref. [267].

the isolated subsystems with potentials V^t and V^s deliver wave functions Ψ^t and Ψ^s, which exponentially decay into the gap (schematic wave functions in Fig. 5.3(b)) [296].

A coupling of the electrodes is established by adiabatically introducing the sample in the presence of the tip by means of a time-dependent perturbation theory ansatz leading to a variant of Fermi's golden rule [267],

$$w_{if} = \frac{2\pi}{\hbar}|M_{if}|^2\delta(E_f - E_i). \tag{5.3}$$

The Dirac delta distribution $\delta(E_f - E_i)$ ensures elastic scattering from the initial into the final state (energy conservation). Essentially, the transfer rate depends on the transition matrix element M_{if}, which can be expressed as the overlapping wave functions Ψ^s and $V^s\Psi^t$ (see Appendix 7.3 for further information). In principle, the current I is calculated from Eq. 5.3 by summing over all initial-final state combinations, $I \propto \sum_{i,f}|M_{if}|^2\delta(E_f - E_i)$ [267].

The elements M_{if} depend on the energy eigenvalues and potential, thus allowing for a more practical representation provided by an energy integration ($|M_{if}|^2 = (|M(E)|\mathrm{d}E)^2 = T(E)$). In this case, the discrete states Ψ^t and Ψ^s are viewed as a continuous distribution given by the product of the density of states $\rho^j(E)$ and the electron occupation $f^j(E)$ in the tip ($j = t$) and the sample ($j = s$). ρ^j denotes the number of available electronic states in an energy interval $[E, E + \mathrm{d}E]$, whereas f^j and $(1 - f^j)$ determine the population of occupied and unoccupied states, respectively. The total current,

$$I = \frac{4\pi e}{\hbar}\int_{-\infty}^{+\infty}\mathrm{d}E\ \left(f^t - f^s\right)\cdot\rho^t\rho^s\cdot T(E), \tag{5.4}$$

is derived by including a factor of two due to the two-fold spin degeneracy of the electrons and by considering the current in both directions (tip→sample, sample→tip) [267].

In thermodynamical equilibrium, the Fermi function $f^j(E) = \left(\exp\left[(E-E_F^j)/k_BT^j\right] + 1\right)^{-1}$, governs the occupation with respect to the Fermi energy (E_F^j) and temperature T^j. However, laser transients illuminating the tunnel gap may cause a non-equilibrium electron population (cf. sec. 2.2). In this scenario, the current in Eq. 5.4 might be modified because of the excitation of the electron gas (changed occupations f^t and f^s).

In the following section, we use Eq. 5.4 to analyze the measured $I(z)$ curves ($z \sim z_{\mathrm{gap}}$). Therefore the transmission probability T is calculated for a specific barrier potential $V(z')$ in the STM gap. We use a one-dimensional scattering approach inserted into the Schrödinger equation that is numerically solved with the Numerov method [297, 298]. The Appendix 7.4 provides the technical details of this approach including the Numerov method itself and the computation of T.

5.3 Controlling photocurrent channels in scanning tunneling microscopy

Benjamin Schröder, Ole Bunjes, Lara Wimmer, Katharina Kaiser, Georg A. Traeger, Thomas Kotzott, Claus Ropers, and Martin Wenderoth

New J. Phys. **22** (2020), 033047
DOI: 10.1088/1367-2630/ab74ac

Abstract We investigate photocurrents driven by femtosecond laser excitation of a (sub)-nanometer tunnel junction in an ultrahigh vacuum low-temperature scanning tunneling microscope (STM). The optically driven charge transfer is revealed by tip retraction curves showing a current contribution for exceptionally large tip-sample distances, evidencing a strongly reduced effective barrier height for photoexcited electrons at higher energies. Our measurements demonstrate that the magnitude of the photo-induced electron transport can be controlled by the laser power as well as the applied bias voltage. In contrast, the decay constant of the photocurrent is only weakly affected by these parameters. Stable STM operation with photoelectrons is demonstrated by acquiring constant current topographies. An effective non-equilibrium electron distribution as a consequence of multiphoton absorption is deduced by the analysis of the photocurrent using a one-dimensional potential barrier model.

5.3.1 Introduction

The combination of ultrafast laser pulses with scanning tunneling microscopy (STM) promises advancements in surface science by connecting sub-nanometer resolution with light-driven dynamics [60–62, 275, 299]. Various optically induced phenomena have been investigated on an atomic level, such as surface photochemical reactions [300–307], photo-induced molecular motion [269, 308–312], charging of individual molecules, defects, dopants and nanostructures [270, 313–318], and tip-enhanced Raman scattering by nanostructures and single molecules [47, 48, 281, 319–321]. Time-resolved STM operation gains particular attention in the form of pump-probe excitation of dynamical processes, which can reach the femtosecond (fs) domain [182, 268–270, 303, 314–316, 322–326].

Light emission from the tunnel gap is exploited to investigate inelastic electron transport across the tip sample contact, such as the radiative decay of localized plasmons [327–331], mapping of molecular orbitals [332], as well as time-resolved and time-correlated electroluminescence [333–335]. The inverse process—exciting the tunnel junction by photons—involves several experimental complications. Particularly, the temperature modulation accompanied by pulsed illumination results in junction instabilities, often obscuring the signals or preventing atomic resolution, as investigated in [60, 336]. Recent technological developments, including the application of THz transients [269, 322], shaken pulse-pair excitation (SPPX)

[337, 338], two-color SPPX [64, 339], two-pulse picking [315, 316] and cross-polarized double beat methods [340, 341] have led to a reliable laser coupling to STM. Further near-field schemes, such as plasmonic nanofocusing, have the potential to further enhance the coupling to the tunneling gap [41, 45, 65, 67, 128].

Alongside this instrumental progress, a detailed understanding of the properties of a tunnel contact during and after fs-laser illumination remains of interest, involving linear and nonlinear absorption mechanisms, transient modifications of the local field distribution, and the diverse pathways of excited charge carriers. Specifically, the energetic distribution of the tunneling electrons due to the optical excitation and the roles of different photocurrent channels is of particular relevance.

In this work, we study the generation of photocurrents by fs-laser pulses in an ultrahigh vacuum (UHV) low temperature STM. The light-driven electron transport manifests itself in modified current-distance dependencies characterized by a much larger decay length compared to regular tunneling. While the magnitude of the photocurrent can be controlled by the incident laser power and the bias voltage, its decay length is largely unaffected by these parameters. Thus, the size of the tunneling gap can be used to vary the ratio of regular tunneling to optically driven electron transfer which allows for stable laser based constant-current imaging of a Cu(100) surface. The observed decay lengths of the photocurrent cannot be directly attributed to the spatially dependent field enhancement of a plasmonic gap mode. In order to identify the mechanism underlying of these enhanced photocurrents, we performed simulations based on a one-dimensional transport model and an effective electron occupation. From these simulations, we identify the major contribution to the photocurrent with transfer channels for hot electrons with energies near the potential barrier maximum.

5.3.2 Methods

The experiments were performed with a home-built UHV low-temperature STM at a base pressure of $5 \cdot 10^{-11}$ mbar and a base temperature of 80 K. Depending on the chosen bandwidth of the measurement electronics and the stability of the tip-sample contact, a current resolution of $50 - 200$ fA is achieved in our setup. The bias voltage U_B is applied to the sample while the tip is virtually connected to ground via the current amplifier. Electrochemically etched gold tips and a Cu(100) crystal have been utilized as the probe and surface material, respectively (Fig. 5.4(a)).

A mode-locked Ti:Sapphire laser oscillator with a center wavelength of 785 nm and 80 MHz repetition rate is used for optical excitation. Pulse duration and focus diameter in the STM chamber are estimated to 70 fs and 18 µm full-width at half-maximum (FWHM) (see Supplemental material 5.3.9 'Interferometric autocorrelation'). The light polarization was chosen to be aligned along the tip's symmetry axis (unless otherwise stated). An overlap of the tunnel contact and the laser focus is achieved by a plano-convex lens (focal length: 200 mm)

mounted outside the STM chamber on a 3D-translation stage (see focal raster scan in the left inset of Fig. 5.4(c)). The optical table and floating STM platform are mechanically decoupled; relative movements of the focus to the tunnel gap are compensated by an active beam stabilization system. Experimental details are found in the Supplemental material 5.3.9 'Methods'.

5.3.3 Experiments

The fundamental ability of resolving single atoms in STM is based on the exponential decay of the tunnel current I upon retracting the tip by the displacement z from the sample. For our system — without illumination — a standard $I(z)$ curve is plotted in Fig. 5.4(b) (black line)[2] showing a slope of 0.8 decades per Ångström, corresponding to an apparent barrier height (ABH) of 3.2 eV for the tunneling electrons (for a definition of the ABH see Supplemental material 5.3.9 'Apparent barrier height'). With a setpoint current of $I_{\mathrm{SP}} = 500\,\mathrm{pA}$, the tunnel current drops below a noise level upon retracting the tip by $\sim 0.5\,\mathrm{nm}$.

A striking change of the retraction curves is observed when the junction is illuminated with fs-laser pulses (Fig. 5.4(b), red to yellow lines). Whereas the current closely follows the (unilluminated) reference at small distances, illumination of the gap greatly enhances the current for increasing displacements. For these larger displacements, the curves again decay as a single exponential. Increasing the laser power to 4.3 mW the photo-driven contribution raises to the 100 fA level up to a distance of 2.3 nm.

We describe the distance-dependent current as the sum of a regular tunneling contribution and a photocurrent, fitting the expression

$$I_{\mathrm{total}}(z_0 + z) = I_{\mathrm{SP}} \cdot \exp(-2\kappa_{\mathrm{tc}} z) + I_{\mathrm{pc}} \cdot \exp(-2\kappa_{\mathrm{pc}} z)$$

to the experimental data, where z_0 is the tip-sample distance at which the setpoint is reached without laser illumination. We extract the photo-driven current fraction ($I_{\mathrm{pc}}/I_{\mathrm{SP}}$), regular tunnel current ABH $\Phi_{\mathrm{tc}} = \hbar^2\kappa_{\mathrm{tc}}^2/2m_e$ and photocurrent ABH $\Phi_{\mathrm{pc}} = \hbar^2\kappa_{\mathrm{pc}}^2/2m_e$ from the obtained decay constants (m_e is the electron mass).

For the regular tunneling contribution, we find the ABH to be independent of the applied laser power; the value of $\Phi_{\mathrm{tc}} \sim 3.2\,\mathrm{eV}$ agrees well with that of the reference curve. In contrast, the ABH of the photo-induced current is $\Phi_{\mathrm{pc}} \sim 0.2\,\mathrm{eV}$. Interestingly, it also shows no dependency on the laser power. The 16 fold reduction of the ABH is an indication of tunneling electrons excited to higher energy levels, close to the vacuum edge. The fraction of the photocurrent prefactors $I_{\mathrm{pc}}/I_{\mathrm{SP}}$ changes from $< 1\%$ for the lowest to 60% for the

[2] Note that throughout this paper, the given displacements z are relative to a starting point $z_0(U_B = 2\,\mathrm{V}, I_{\mathrm{SP}})$, i.e., the initial tip-sample distance, defined by the bias voltage U_B (set to 2 V) and the set point current I_{SP} without laser illumination. Usually, z_0 attains values between 0.7 nm and 0.9 nm for typical tunnel parameters [296]. Additionally, z_0 must be modified by $\Delta z(U_B, P)$ when changing the bias voltage or laser power (see Supplemental material 5.3.9 'Start point correction').

highest measured laser power. Due to the additional photocurrent, for laser illumination, the setpoint is established at an offset distance $\Delta z(P) > 0$ from z_0, determined from the condition $I_{\text{total}}(z_0+\Delta z(P)) = I_{\text{SP}}$ (see Supplemental material 5.3.9 'Start point correction'). Note that these offsets are of minor magnitude.

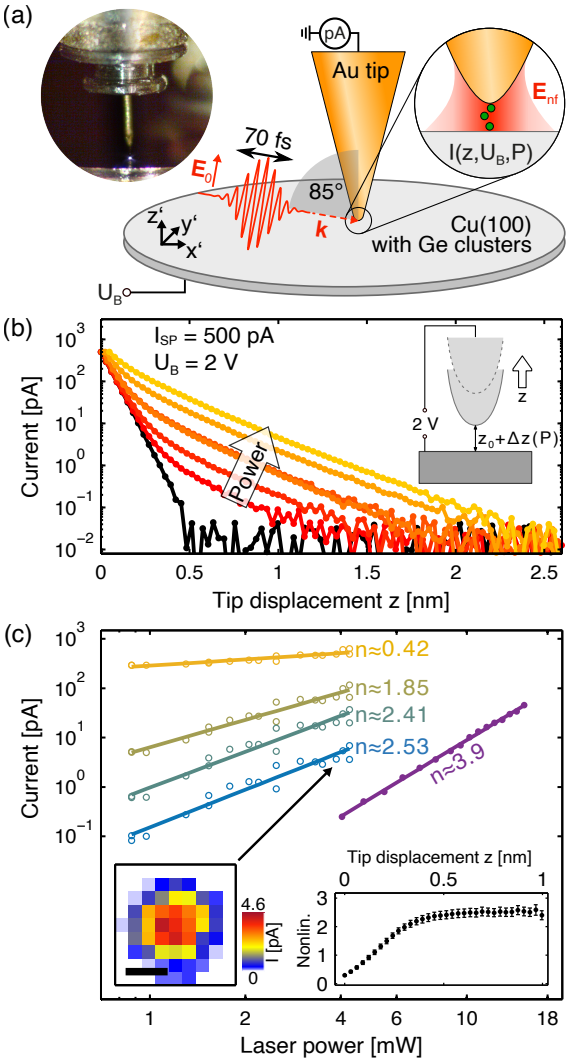

Fig. 5.4: (a) Schematic illustration of the experimental setup. A gold tip and Cu(100) surface are used as probe and sample, respectively. The p-polarized laser field ($\mathbf{E}_0$) propagating with the wave vector $\mathbf{k}$ is focused onto the tunnel contact (see photo). Generally, the measured current is a function of gap width, bias voltage and laser power (indicated in the zoom-in). Laser illumination leads to an enhanced near-field $\mathbf{E}_{\text{nf}}$ in the tunnel junction. (b) Current-distance dependencies without (black dots) and with gap illumination (increasing power from red to yellow dots: 1.0, 1.3, 1.8, 2.5, 3.3 and 4.3 mW) (logarithmic scale). The inset schematically demonstrates the measurement: Starting from the setpoint of 500 pA reached at $z_0 + \Delta z(P)$, the tip is retracted while measuring the current. (c) Double-logarithmic plot of the current as a function of average laser power for different tip displacements (0.03, 0.3, 0.5, and 0.9 nm (yellow to blue)). The effective nonlinearities n resulting from linear fits (solid lines) are indicated near the curves. For comparison, the current-power dependency of the tip retracted ~ 1 µm from the surface is plotted in purple. (Right inset) Nonlinearity as a function of tip displacement. For z > 0.5 nm the nonlinear order attains a nearly constant value of $\sim$ 2.5. (Left inset) Focal raster scan across the tunnel gap for a tip displacement of 0.9 nm (scale bar: 5 µm) demonstrating a more strongly confined photocurrent ($\sim 20\ \mu\text{m}^2$) than the focus spot size ($\sim 250\ \mu\text{m}^2$).

The high stability of our setup allows for an investigation of the nonlinearity of the photocurrent (Fig. 5.4(c)). As reference, we measured the photo-emitted current for the retracted tip (~ 1 µm distance to the sample). Laser-driven electron currents from free-standing gold tips previously revealed multiphoton photoemission (MPPE) processes [50, 51, 67, 104, 105, 167]. This is described by a generalized Fowler–DuBridge theory connecting the current with the average laser power P by a power law, $I \sim P^n$ [161]. The effective nonlinear order n is a measure of the number of photons per electron involved in the photoemission process. We observe a nonlinearity of 3.9 (purple dots), close to the expected value for an Au tip with a work function of ~ 5 eV. For different tips, we find values of n between 3.5 and 4.5, consistent with earlier results for free-standing tips [67, 104, 105]. For the tip-sample

contact, the nonlinear order is greatly suppressed: n attains a constant value of ~ 2.5 for all displacements $z > 0.5\,\mathrm{nm}$ (right inset in Fig. 5.4(c)), which is in accordance with a previous result [182]. Importantly, this nonlinearity indicates lower-order emission processes for the photon-driven current contribution compared to the free-standing tip. For $z < 0.5\,\mathrm{nm}$ (green and yellow line), the found values are further reduced by the additional regular tunneling, which starts to dominate upon approaching the setpoint. Hence, this reduction in nonlinearity is not linked to a change of the electron transfer process. Interferometric autocorrelation measurements of the photocurrents emitted from a free-standing tip and in the tunnel contact confirmed the general trend of a reduced nonlinear order for the gap illumination (see Supplemental material 5.3.9 'Interferometric autocorrelation').

The reduced barrier involved in the photo-induced electron transfer suggests a further investigation of the photocurrent dependency on the barrier shape and height, which can be adjusted by the bias voltage (Fig. 5.5(a)).

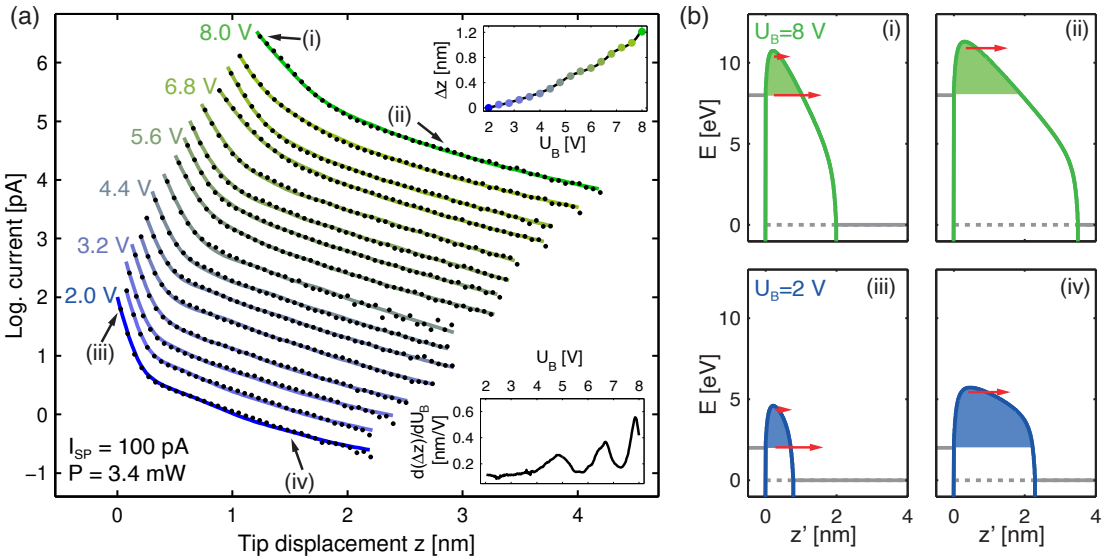

Fig. 5.5: (a) Measured current-distance dependencies $I(z)$ for different bias voltages from 2 V to 8 V (black dots) under constant gap illumination with 3.4 mW power and a setpoint current of 100 pA. The curves are plotted on a semi-logarithmic scale and are vertically shifted for clarity (data points below the noise level of 200 fA are excluded). Horizontally, the curves are shifted due to start distance changes $z_0 + \Delta z(U_B)$ upon ramping the bias voltage according to a separate $\Delta z(U_B)$ measurement (top inset and Supplemental material 5.3.9 'Start point correction'). Solid lines are the simulation results based on a one-dimensional potential model (details in the text). Upon changing the bias voltage, different field emission resonances become accessible by the electrons, as demonstrated by peaks occurring in the derivative of the $\Delta z(U_B)$ dependency (bottom inset). (b) Modeled potential barriers for 2 V (iii, iv) and 8 V (i, ii) at gap widths indicated in (a). The major current channels are indicated by the red arrows with different magnitudes (arrow length is not to scale). Color shaded areas assign to the relevant barrier. The Fermi energy levels of the tip and sample are given as horizontal lines on the left and right side of the potential barrier.

While the data at a low bias voltage ($U_B < 5\,\mathrm{V}$) can be described by the above-mentioned bi-exponential behavior, additional features are observed for $U_B > 5\,\mathrm{V}$. These are attributed to field emission resonances (FER), also evident as peaks in the $\mathrm{d}(\Delta z)/\mathrm{d}U_B$ spectrum [342–345] (bottom inset of Fig. 5.5(a)) (details are found in the Supplemental material 5.3.9 'Field

emission resonances'). For measurements in the interval from 2 V to 8 V, we extract regular tunneling ABHs ranging from 3.0 eV down to 0.5 eV, respectively. These values match to the found Φ_{tc} without illumination (a comparison of dark versus illuminated data is given in Fig. 5.11 in the Supplemental material). Interestingly, the determined ABHs of the photocurrents do not exhibit such a trend, with values weakly varying around a few to a few tens of meV.

The transition to the negative bias voltages regime ($-1\,\mathrm{V} \leq U_B \leq 0\,\mathrm{V}$) reveals positive, photo-driven currents (Fig. 5.12 in the Supplemental material): Although the negative setpoint results in a negative regular tunneling (from the sample to the tip) for very small displacements, we find optically driven electron transfer reverse to the static electric field (from the tip to the sample) for larger tip displacements. Note that for $U_B \lesssim -1\,\mathrm{V}$ the positive photocurrent is compensated by negative photo-driven currents from the surface.

5.3.4 Laser-driven STM

Controlling the photocurrent fraction $I_{\mathrm{pc}}/I_{\mathrm{SP}}$ allows for a transition from regular to photon based imaging. To investigate the impact of surface features on the photocurrent and on topographic information, we measured constant-current topographies of a Cu(100) surface covered with 0.1–0.2 monolayers of Ge clusters (Fig. 5.6). By controlling the setpoint current and laser illumination,we can change the ratio $I_{\mathrm{pc}}/I_{\mathrm{SP}}$ (Fig. 5.6(d)). Interestingly, both measurements with laser excitation for $I_{\mathrm{pc}}/I_{\mathrm{SP}} = 8\%$ (b) and $I_{\mathrm{pc}}/I_{\mathrm{SP}} = 98\%$ (c) resolve all features present in the reference topography without illumination (a) (there is a small thermally induced drift). Some blurring in (c) is attributed to the increased tip-sample distance (broader transfer function of the tip). Figure 5.6(e) demonstrates for all three scenarios (standard tunneling, $I_{\mathrm{pc}}/I_{\mathrm{SP}} = 8\%$, and $I_{\mathrm{pc}}/I_{\mathrm{SP}} = 98\%$) a quantitative agreement of the topographic heights of the Cu step edge and the Ge clusters.

We note that multiple sequentially measured topographies with and without laser illumination show no indication of a tip- or laser-induced surface modification.We can therefore rule out previously observed changes in surface morphology [346], induced by thermal tip expansion and penetration into the surface [60, 347, 348].

5.3.5 Modeling

In the following, we address the mechanism underlying the observed current-distance characteristics $I(z)$ for the optically excited tunnel junction. Generally, the electron transport is determined by two major quantities. Firstly, the charge carrier has a transfer probability T to transmit from one electrode to the other. Specifically, T is determined by the potential barrier formed between both electrodes. Hence, it is a function of the electron energy E, the gap width $z_{\mathrm{gap}} \sim z$ and the bias voltage U_B. Secondly, the number of transmitting charge carriers is given by the initial occupied and by the final empty states. In an elastic process, this number is a function of the occupation distribution and density of states of the tip and

sample at the energy E [296].

Under fs-laser excitation both the transmission probability and the electron population can be transiently changed due to photon absorption or local field modifications. However, for moderate excitation intensities (perturbative regime), we can exclude strong-field effects on the potential landscape determining the transmission probability (see discussion) [105, 182]. Therefore, the impact of the laser excitation on the electron population can be modeled by an effective time-averaged occupation function f_{eff} [104, 171].

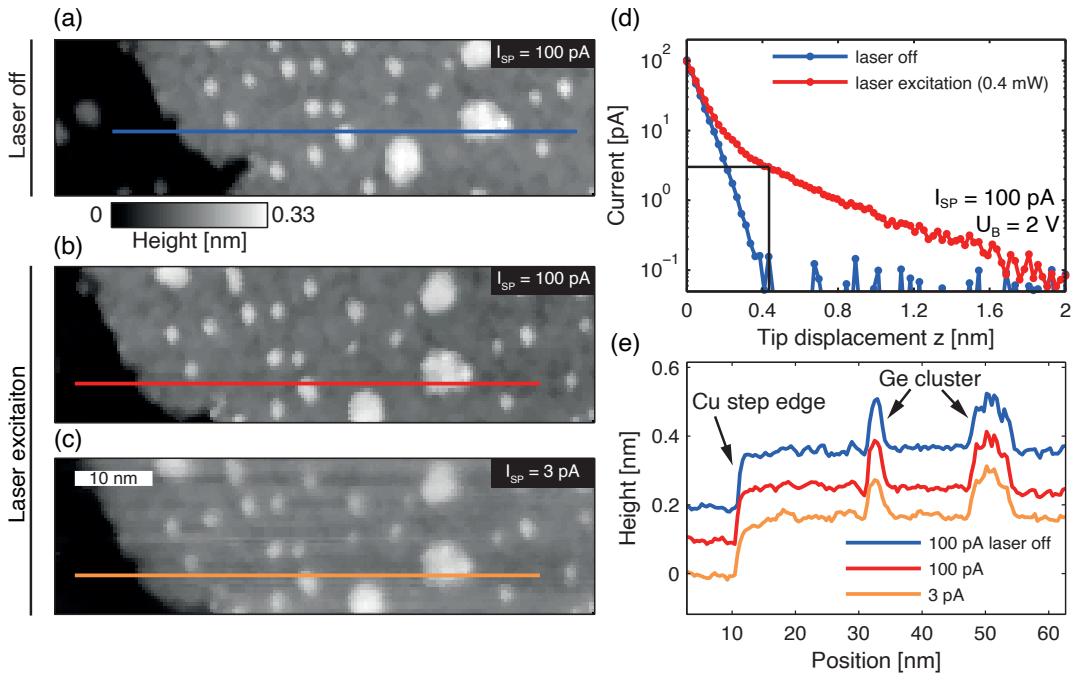

Fig. 5.6: (a)–(c) Constant-current topographies of the Cu(100) surface with Ge clusters (white regions) including a Cu step edge (located on the left) for different excitation conditions and setpoint currents ($U_B = 2\,\text{V}$). The colored lines represent the line profiles plotted in (e). Note that the topography section of (a) is slightly shifted compared to (b) and (c) due to thermal drift. (a) Reference topography with $I_{\text{SP}} = 100\,\text{pA}$ without laser excitation. (b), (c) topographies measured with laser excitation ($P = 0.4\,\text{mW}$) for a setpoint current of 100 pA (b) and 3 pA (c). The latter current is composed by $> 98\%$ of laser-driven electrons (compare the associated $I(z)$ curve (red dots) in (d) with the dark reference curve (blue dots)). The chosen setpoint used in (c) and the respective tip displacement are indicated by the black line as a guide to the eye. (e) Line sections along the lines indicated in (a), (b), and (c) for the three conditions of $I_{\text{SP}} = 100\,\text{pA}$ without laser (blue), $I_{\text{SP}} = 100\,\text{pA}$ with light excitation (red), and $I_{\text{SP}} = 3\,\text{pA}$ with light excitation (orange). The lines are vertically shifted by 0.1 nm for clarity. Evidently, the matching of the three profiles, including the Cu step edge and Ge clusters, demonstrate the conformity of standard and laser-driven topographic imaging in our experiment.

Based on the Bardeen model for tunneling, we calculate the current I by an energy (E) integral over the product of the electron occupation f_{eff} and the transmission probability T [296]:

$$I(z, U_B, \mathbf{E}_{\text{nf}}) \sim \int_0^\infty \mathrm{d}E \; f_{\text{eff}}(E, \mathbf{E}_{\text{nf}}(z)) \cdot T(E, z, U_B), \tag{5.5}$$

assuming a constant density of states for the tip and the sample. The temperature of the

sample is set to 0 K, hence, the electron occupation is unity up to the Fermi level on the sample side. Importantly, the electron population in the tip f_{eff} is given by the absorption of photons from the enhanced near-field $\mathbf{E}_{\mathrm{nf}}$ in the tunnel gap (see zoom-in in Fig. 5.4(a)), which depends on the laser power, the tip-sample geometry and the dielectric response of the materials. Especially, for gold nanostructures excited with near-infrared light, we expect a strong enhancement of $\mathbf{E}_{\mathrm{nf}}$ due to a local surface plasmon (gap plasmon) [206, 281, 328, 349]. Explicitly, both the occupation f_{eff} and transmission T are functions of the tip-sample distance $z_{\mathrm{gap}} \sim z$, which is given by the tip displacement z in the experiment.

We first consider the possibility of the local field $\mathbf{E}_{\mathrm{nf}}(z)$ responsible for the measured photocurrent spatial decay. Since the plasmonic enhancement is a function of the system's geometry and the dielectric properties of the materials, a strong modification of $\mathbf{E}_{\mathrm{nf}}$ is expected when sharp features on the surface or different materials are present in the gap [45, 203, 204, 206, 341]. This should lead to different topographic heights when imaging the surface with photo-driven electrons compared to the regular tunneling. Yet, we find the same topographic profiles for both cases (see Fig. 5.6(c)).

Moreover, given the experimental geometry, the very short decay lengths render the gap plasmon z-dependency an unlikely explanation. Specifically, the expected field-distance dependency of the signal can be estimated by a coupled dipole approximation, with the tip apex modeled as a sphere (see Supplemental material 5.3.9 'Near-field enhancement') [277]. The associated electric field component in the z'-direction E_{nf} is given by an algebraic relation $E_{\mathrm{nf}} \sim (z_{\mathrm{gap}} + R_T)^{-3}$ with the tip radius R_T and gap width $z_{\mathrm{gap}} \sim z$ [281]. Estimating the distance dependency of a current driven by a nonlinear process $I(z) \sim |E_{\mathrm{nf}}(z)|^{2n}$ for different tip radii and $n = 2.5$ (Fig. 5.14 in the Supplemental material), the observed decay lengths in our experiment could only be achieved for unrealistically small tip radii ($\lesssim 5$ nm). However, such radii would lead to a strong deviation from an exponential law, in contrast to our experimental findings. We estimate a signal reduction by a factor of up to ~ 11 in the experimentally relevant regime of $0.7 - 3.2$ nm for a tip radius providing a nearly exponential decay of the near-field (the actual reduction factor is expected to be even lower, since plasmon-driven tunneling reduces the field enhancement for very low distances [138, 281]). In contrast, we find reduction factors of up to 10^4 in the related distance regime in our experiment (see Fig. 5.4(c)). Interestingly, a current-distance dependency measured for increased laser powers (~ 35 mW) strongly deviates from the low-power experiments (Fig. 5.15 in the Supplemental material). The setpoint current is purely laser-driven. Therefore, the tip-sample distance must be considerably larger[3]. In this case, it deviates from an exponential law with a decay length much larger compared to the curves in Fig. 5.4(b) and Fig. 5.5(a), and the current converges to a finite value of 0.4 pA at the distance of 10 nm. A tip radius of $R_T = 28$ nm and a nonlinear order of $n = 4.4$ is extracted from a fit of the coupled dipole model to the data in Fig. 5.15. We attribute these results to a four-photon process dom-

[3] A precise start distance cannot be given, since no reference in the form of a transition starting from regular tunneling is present in the data.

inating the intermediate distance regime with a current decay governed by $\mathbf{E}_{\mathrm{nf}}(z)$. Thus, another mechanism must be responsible for the observed decay length scale for the short distance regime and the near-field enhancement is assumed to be constant in the model discussed below. Consequently, the effective occupation distribution has only an explicit energy dependency, whereas the near-field enters as a parameter given by the laser power ($f_{\mathrm{eff}}(E, \mathbf{E}_{\mathrm{nf}}) = f_P(E)$).

We find the z-dependency of the transmission probability $T(E, z, U_B)$ to explain the observed photocurrent spatial decay. We calculate T with a one-dimensional representation of the potential landscape including image potentials for both electrodes (Fig. 5.7(a) and panels (i)–(iv) in Fig. 5.5(b)). Field emission resonances and their spectral change due to the Stark shift is covered by the model as well. For this potential, we numerically solve the Schrödinger equation with the Numerov method (see schematic wave function in Fig. 5.7(a)) and extract the transmission probability from the found scattering parameters [297, 350]. A detailed description is found in the Supplemental material 5.3.9 'Transport model'. From Eq. 5.5 the current with its tip-sample distance and bias voltage dependency is simulated as a function of the excited electron population $f_P(E)$,

$$I(z, U_B) = C \int_0^\infty \mathrm{d}E \; f_P(E) \cdot T(E, z, U_B), \tag{5.6}$$

with a scaling constant C. $f_P(E)$ is modeled as a parameterized sum over N Fermi–Dirac distributions of different magnitudes A_j, energy intervals E_j and energy widths ΔE_j [104, 171]:

$$f_P(E) = \sum_{j=0}^{N} A_j \Big/ \left(\exp\left[\frac{E - (eU_B + E_j)}{\Delta E_j} \right] + 1 \right),$$

whereas the tunnel current reveals the general distribution of electrons, it is not necessarily sensitive to the exact locations of the intervals E_j. Thus, for simplicity, we set the energy intervals of $f_P(E)$ to multiples of the photon energy $E_j = j \cdot \hbar\omega$ above the Fermi energy, with integer j and $\hbar\omega = 1.55\,\mathrm{eV}$. We find that one unexcited ($j = 0$) and two higher-energy contributions ($j = 1, 2$) are fully sufficient to describe the data.

We note that there is no one-to-one correspondence between the energy intervals and the respective one- or two-photon absorption process. Specifically, the observed nonlinear order of 2.5 indicates that other factors, including lower-lying initial states and energy redistribution by thermalization, significantly affect the resulting carrier distribution. The parameters adjusted are the amplitudes A_1 and A_2 relative to A_0 (set to unity), the energy widths ΔE_1 and ΔE_2, and the scaling constant C. The broadening $\Delta E_0 = 7\,\mathrm{meV}$ is set to correspond to the base temperature of 80 K.

5.3.6 Simulation results

The simulations yield a general agreement with the respective experimental curves demonstrating the broad applicability of the model (lines in Fig. 5.5(a) and 5.8(a)). One representative result is presented in Fig. 5.7(c) along with the respective occupation function in Fig. 5.7(b). Each individual current channel (black lines and colored areas) exhibits an almost ideal exponential decay over all displacements and justifies the previously applied multi-exponential fits. As found before, the short- and long-distance ranges are dominated to nearly 100% by the regular and high-energy contributions (I_2), respectively. The first photocurrent channel (I_1) contributes only in a narrow transition region with a few percent of the total current (Fig. 5.7(d)).

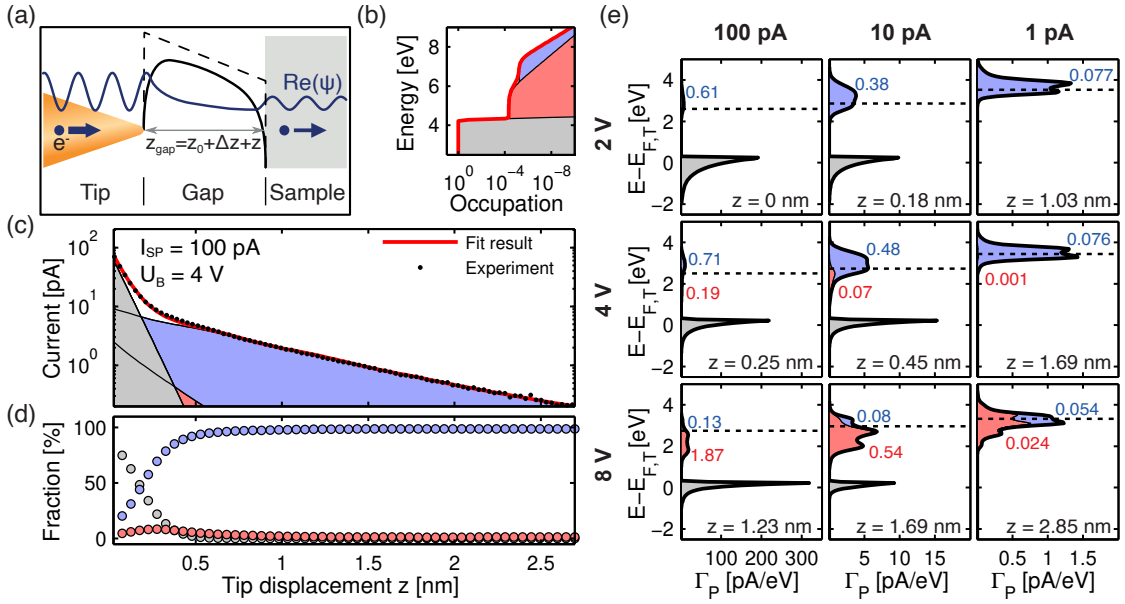

Fig. 5.7: (a) Schematic illustration of the one-dimensional potential barrier model used to calculate the electronic transmission probability. The triangular potential due to the bias voltage and the difference between the work functions (dashed black line) is superimposed with the image potentials of tip and sample resulting in the total potential (black solid line). A schematic electron wave function is plotted as the blue line. (b) The three-component electron occupation distribution associated with the simulation result shown in (c). (c) Experimental $I(z)$ curve (black dots), together with the sum of the three channels (red solid line). The colored areas beneath the curves assign the energy domains of the occupation in (b) to the resulting current in (c). (d) Current fraction at each tip displacement for the three channels. (e) Representations of the energetic composition of the current for three currents (100 pA, 10 pA and 1 pA columns) and for three bias voltages (2 V, 4 V and 8 V, rows). The corresponding displacements are indicated in the bottom right corners. Colors refer to the particular energy channel the electron is transferring from (as in (b)–(d)). Barrier potential maxima are indicated by the dashed black lines. The numbers specify the partial current in units of electrons per laser pulse for the first and second photocurrent channel. The integration along the energy axis gives the total current for a given distance and bias voltage. The energy axis is given relative to the bias voltage, i.e., the Fermi level in the tip.

We identify the electron energy regions from which the current channels are originating by calculating the product $\Gamma_P(E) = C f_P(E) \cdot T(E)$, i.e., the integrand of Eq. 5.6 (Fig. 5.7(e)). Several conclusions can be drawn: (1) While I_2 is the dominant photo-driven current for

all bias voltages, the relative fraction I_1/I_2 becomes more substantial at higher bias voltages. (2) The higher-energy contributions are always close to the potential barrier maximum (extracted from the simulation and indicated by dashed lines in Fig. 5.7(e)), which is consistent with the fitted ABH of a few tens of meV. However, there is always a significant above-barrier fraction (up to 80% (0.8 pA) for the 2 V case). (3) The energy bandwidth (FWHM) of the channels is of the order of 0.5 eV and $0.8 - 1.5$ eV for regular tunneling and photocurrent, respectively. (4) Field emission and scattering resonances enforce the appearance of a modulated contour evident by multiple peaks and shoulders around the potential barrier maxima for larger distances and higher bias voltages (compare, e.g., 4 V and 8 V for 1 pA).

Analyzing the current composition as a function of laser power[4] (Fig. 5.8(b)) shows that I_1 has a significant contribution for lower laser powers. The average charge transferred per channel can be increased up to a few tens of electrons per laser pulse by increasing the incident power (indicated as numbers in Figs. 5.7(e) and 5.8(b)).

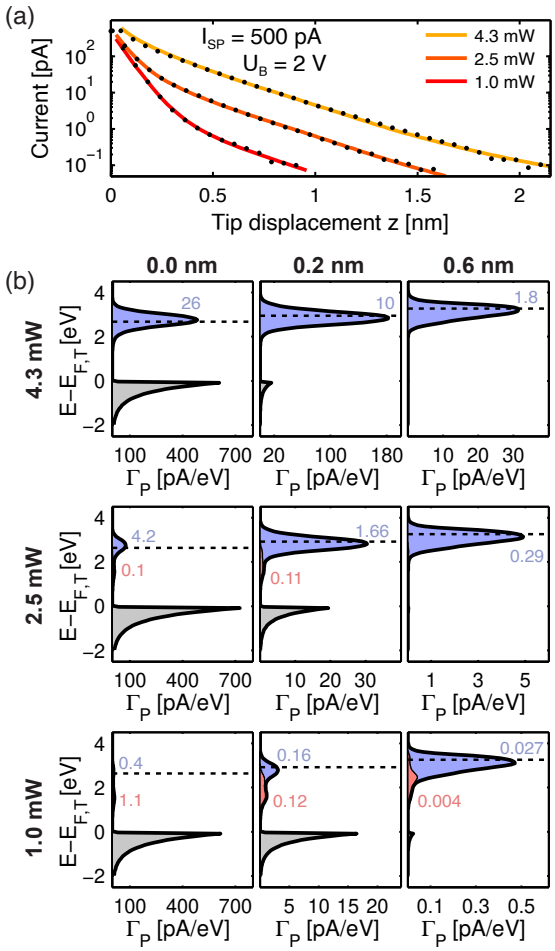

Fig. 5.8: (a) Three examples of the experimental $I(z)$ curves (black dots) for the average laser powers of 1.0 mW, 2.5 mW and 4.3 mW and the corresponding simulation results (solid lines). (b) Representations of the energetic composition of the current for three distances (0.0 nm, 0.2 nm and 0.6 nm, columns) and for the three average laser powers in (a) (rows). Note the changing of the x-axis scaling. As in Fig. 5.7(e) colors assign to the current channels: regular tunneling (gray), first (magenta) and second (blue) photocurrent contribution. Barrier potential maxima are indicated by the dashed black lines. The numbers indicate the partial current in the unit of electrons per laser pulse.

[4]Note that here we use constant displacements instead of constant currents (as in Fig. 5.7(e)). The z-shift corrections Δz are of minor magnitude and, therefore, currents at a constant tip displacement are comparable.

5.3.7 Discussion

The results presented in this paper, specifically the determination of the effective electron distributions, yield insights into the transport mechanism responsible for photocurrents in STM under fs-laser illumination. The main experimental features are reproduced, and the findings suggest multiphoton absorption processes leading to the population of higher-energy electron states (hot electrons) close to the potential barrier maximum. Open questions involve the possible participation of higher-order photon absorption, the role of lower-energy initial states (d-band), and transfer rate modifications due to quantum coupling of electronic states (quenching of radiative resonances).

As former studies demonstrated, thermally induced tip expansion due to the pulsed illumination have been a major issue for combining STM and fs-laser excitation, since they can obscure the electronic signal by the oscillatory altering of the gap width by a certain amount of $\delta z_{\mathrm{exp}}(t)$ and its strong impact on the exponential tunnel current [60]. The tip expansion can result in a mechanical tip-sample contact, which causes instabilities and tip and sample structuring [346]. However, for the low laser fluences used in this experiment, we can neglect any contact formation (as demonstrated in Fig. 5.6). The magnitude of $\delta z_{\mathrm{exp}}(t)$ can be estimated from theoretical and experimental studies, which demonstrate monotonically decreasing values for high repetition rates[5] [347, 348]. In addition, by assuming an exponential current-distance relation $I(z,t) \sim \exp(-2\kappa[z + \delta z_{\mathrm{exp}}(t)])$ we see that for the measured time-averaged signal,

$$< I(z,t) >_t = < \exp(-2\kappa \delta z_{\mathrm{exp}}(t)) >_t \, I(z) = c_{\mathrm{exp}} I(z),$$

only a modification of the amplitude by a constant factor $c_{\mathrm{exp}} \approx 1$ is present (assuming $\delta z_{\mathrm{exp}}(t)$ independent of z). Hence, an oscillatory tip expansion $\delta z_{\mathrm{exp}}(t)$ cannot explain the found reduced ABH.

We conducted several validation experiments that exclude a strong thermal impact on the observed current distance dependencies. First of all, the negative bias measurements (Fig. 5.12 in the Supplemental material) show a strong rectification effect, i.e., even for negative setpoint currents (electron transfer to the tip) we find a positive current contribution (electron transfer to the sample) when retracting the tip out of the regular tunneling regime. Secondly, we do not find any signal for laser s-polarization. Finally, the signal is confined to an area that is a factor of 5–6 smaller than the focal spot size (demonstrated by the focal scan in the left inset of Fig. 5.4(c)). This is a strong indication of the nonlinearity of the photo-driven current and contradicts a thermal expansion effect which, in contrast, is expected to be governed by linear absorption.

[5] Most of the presented data was measured with laser average powers between 1 mW and 10 mW. The resulting fluences are several magnitudes below the contact formation threshold given in [346]. Moreover, the amplitude of the oscillating tip expansion is expected to be in the sub-Ångström regime as estimated from theoretical and experimental studies [347, 348].

Our experiments have been operated in the perturbative regime with low-order nonlinear transitions. By contrast, strong-field effects are expected to play a major role for laser powers increased by about a factor of 10 compared to those in our experiments [105, 182]. Performing STM measurements under such conditions, laser power-dependent ABHs have been observed [341]. In the limit of much lower intensities, continuous-wave illumination may change the transfer mechanism to plasmon-assisted resonant tunneling, as recently demonstrated by FER shifts of one photon energy [351]. We do not observe such shifts, presumably due to a broader electron energy distribution and the smaller photo-driven contribution to the total current (see Fig. 5.13 in the Supplemental material).

Both the experimental and theoretical approach can be further extended. On the one hand, pump-probe schemes have the potential to give access to the temporal evolution of the electron distribution [153]. On the other hand, additional modeling, including the distance-dependent plasmonic field, electronic band structures, the three-dimensional transient field distribution as well as the relaxation dynamics (Landau damping, electron–electron and electron-phonon scattering) promise further information on the specific electronic pathways under fs illumination [133, 352].

5.3.8 Conclusion

In conclusion, we demonstrated photo-driven electron transfer through the tunnel junction of a scanning tunneling microscope. Under gap illumination, this current is evident by tip retraction curves with additional contributions distinguished by a strongly reduced apparent barrier height leading to a long decaying current compared to regular tunneling. The analysis of power-dependent measurements suggests a multiphoton absorption mechanism where the electrons are excited to levels a few 100 of meV around the potential barrier maximum. Neither the laser power nor the bias voltage strongly affects the ABH in the measured range. The electron excitation to the high energies is provided by the plasmonically enhanced field, albeit its distance dependency does not explain the observed decay length scales. Simulations based on a one-dimensional potential barrier model and a time-averaged effective electron occupation are able to reproduce the central features of the current-distance dependencies. By this, we identify the involved energy domains from which the transfer channels are established and find a high-energy distribution in the vicinity of the potential barrier maximum to be the dominant contribution. Prospectively, this could provide an ultrafast excitation procedure with high-energy electrons in a nearly field-free environment, e.g., to disentangle field- and particle-driven chemical reactions of molecules.

Acknowledgments We gratefully acknowledge the funding by the Deutsche Forschungsgemeinschaft through the SFB 1073 (Project C04) and Grant No. WE1889/8. We thank Karin Ahlborn for help in tip preparation and Tobias Claus for experimental support.

5.3.9 Supplemental material

Methods

Experimental setup Figure 5.9 illustrates the experimental setup. A Titanium-Sapphire laser oscillator (Coherent Vitara T-HP) provides laser pulses with 80 MHz repetition rate. The laser spectrum has a center wavelength of 785 nm and a bandwidth of 60 nm (see spectrum in the inset). A pair of a remotely rotatable half-wave plate and a film polarizer is used to set the laser polarization and average power. The polarization is chosen to be p-polarized (aligned along the tip's symmetry axis), unless otherwise stated. The beam width is increased by a factor of five with a telescope arrangement resulting in a focus diameter of 18 µm in the STM after passing a plano-convex lens (focal length: 200 mm). A precise positioning and raster scanning of the focus is achieved by remotely moving the focusing lens with a 3D-translation stage.

An active beam stabilization system consisting of a beam position detector on the STM platform and a piezo actuated mirror on the optical table is implemented to prevent pointing caused by the relative movement between both table and platform. Optionally a Michelson-type interferometer can be inserted into the beam line by replacing the central mirror with a 90° turned beam splitter (dashed section in Fig. 5.9). With this we estimated the pulse duration to be 70 fs in the STM chamber from autocorrelation traces (see Supplemental material. 5.3.9 'Interferometric autocorrelation').

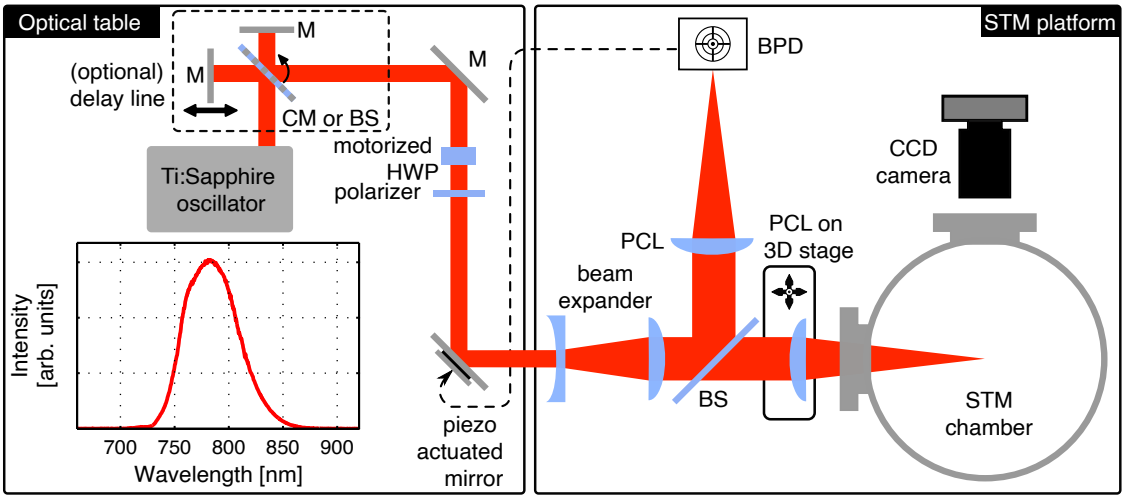

Fig. 5.9: Schematic illustration of the experimental setup. M: mirror, CM: central mirror, BS: beam splitter, HWP: half-wave plate, PCL: plano-convex lens, BPD: beam position detector, CCD: charge-coupled device. The inset shows the laser output spectrum.

We used a home-built UHV scanning tunneling microscope with $5 \cdot 10^{-11}$ mbar of base pressure for the experiments. The system is cooled with liquid nitrogen down to 80 K. Currents are converted to voltage signals by an I–V-converter (1 V/nA) with a bandwidth of 1 kHz. Hence, the STM feedback control is not affected by the 80 MHz modulation of the

laser oscillator and only a time averaged signal is recorded. The bias voltage is connected to the sample, while the tip is grounded. Viewports allow for an optical access for the laser illumination and the monitoring of the tip and focus position via a CCD camera (Fig. 5.4(a)).

Tip and sample preparation Gold wires (250 µm in diameter) are annealed in vacuum with 750 °C for several hours. This increases the mean grain size and leads to quasi-single-crystalline apex sections for the final tips. Afterwards a tapered end is achieved by electrochemical etching with 37% hydrochloric acid and subsequently the tips are cleaned with iso-2-propanol and distilled water. Shape and surface quality as well as apex radii are checked by scanning electron microscopy (details, e.g., in Refs. [45, 183]). Moderate annealing at 150 °C for 72 h is conducted to clean the tip surface in the UHV during a preparation chamber bake-out. Cu(100) treatment comprises multiple cycles of argon ion sputtering (700 V) and annealing (350 °C–400 °C) of single crystals. Finally, 0.1–0.2 monolayers of germanium have been evaporated by electron-beam evaporation.

Apparent barrier height

In general, the work function of a material is the central quantity defining the potential barrier for an electron that transfers from the cathode to the anode. For sub-nanometer gaps between both electrodes this barrier is strongly modified in its shape and height. In this case, the characteristic quantity of electron transport is the apparent barrier height (ABH) which is a measure of the effective potential:

$$\Phi_{\mathrm{ABH}}(z) = \frac{\hbar^2}{8m_e}\left(\frac{\mathrm{d}\ln I}{\mathrm{d}z}\right)^2,$$

where m_e is the electron mass [296]. For an exponential current representation ($I(z) \sim \exp(-2\kappa z)$) the ABH simplifies to $\Phi_{\mathrm{ABH}} = \hbar^2\kappa^2/2m_e$ with the decay constant κ.

Start point correction

In conventional STM, the absolute tip-sample distance z_0 is determined by the parameters bias voltage U_B and setpoint current I_{SP}. In our experiments, the start point is also a function of the laser power P, since the photo-driven signal has a pronounced tip-sample distance dependency. We take this circumstance into account by introducing a distance $\Delta z > 0$. Qualitatively, for a given distance, the current increases when increasing U_B or P and, in conclusion, the tip has to be retracted by Δz from the sample in order to keep the setpoint current constant.

In our experiments, we did power $I_P(z)$ and voltage $I_{U_B}(z)$ dependent measurements for given setpoint currents and corrected the data sets by extracting $\Delta z(P)$ from the bi-exponential fits and by using a separate $\Delta z(U_B)$ measurement for the power- and bias

voltage-dependent measurements, respectively (Fig. 5.4(b) and 5.5(a)). While a minor correction of 0.05 nm is determined for the highest laser power compared to the lowest one, $\Delta z = 1.2$ nm is found for a voltage change from 2 V to 8 V (see top inset of Fig. 5.5(a)).

Interferometric autocorrelation

We measured interferometric autocorrelation traces for the two scenarios of a free-standing tip (~ 1 µm tip-sample distance) and for tunnel contact (Fig. 5.10(a) and (b)) by utilizing double pulses with a variable delay provided by a Michelson-type interferometer (see Fig. 5.9). Both interferometer arms have the same laser average power and are collinearly interfering at the apex or at the tunnel junction. In order to measure only the photo-driven current, the tip is retracted at each delay step by 0.7 nm with respect to the setpoint (no regular tunneling) and the photocurrent is recorded. $I(z)$ curves demonstrate for a maximal pulse overlap and without a pulse overlap that the photocurrent is finite and regular tunneling is dominant providing a quasi-constant reference distance z_0 at each delay step (see inset in Fig. 5.10(b)). As in the power-dependent measurement in Fig. 5.4, the setpoint distance z_0 only varies in a sub-Ångström regime for different delays.

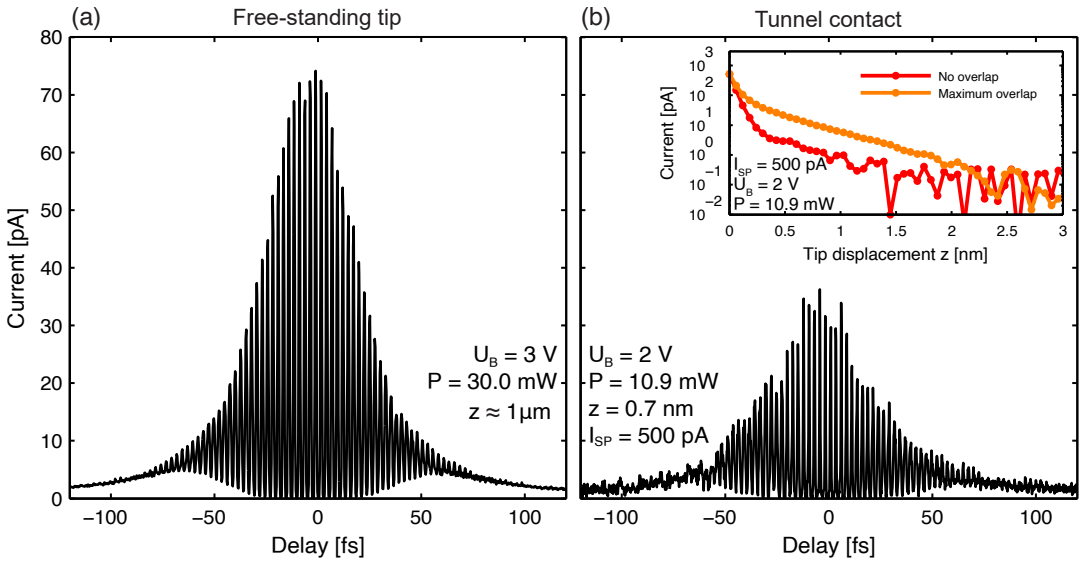

Fig. 5.10: Interferometric autocorrelation traces of the photo-induced current for the two scenarios of a free-standing tip (a) and a tip in tunnel contact (b). (a) The tip is retracted by roughly 1 µm from the surface. The two pulses are collinearly superimposed on the tip apex. From this autocorrelation the pulse length is estimated to be ~ 70 fs FWHM.(b) For each delay the STM feedback control is switched off and the tip is retracted by 0.7 nm to insure a pure optical signal as evident by tip displacement measurements for none and maximal pulse overlap (inset).

From the traces we found peak-to-background ratios (PBR) of ~ 68 and ~ 31 for the free-standing tip and for tunnel contact, respectively, which indicates the high nonlinearity n of both situations: under ideal experimental conditions the PBR is equal to 2^{2n-1}. This implies an effective nonlinearity of $n = 3.54$ for the free-standing tip and $n = 2.97$ for the

tunnel contact. These values are within the variations, which we observed in the power-dependent measurements and support that we have a lower nonlinear order in the tunnel contact compared to a free-standing tip. The value of $n \approx 3$ for the tunnel contact might be somewhat overestimated due to thermal tip expansion changes induced by the intensity oscillations in the interfering pulses.

Bias voltage-dependent measurements

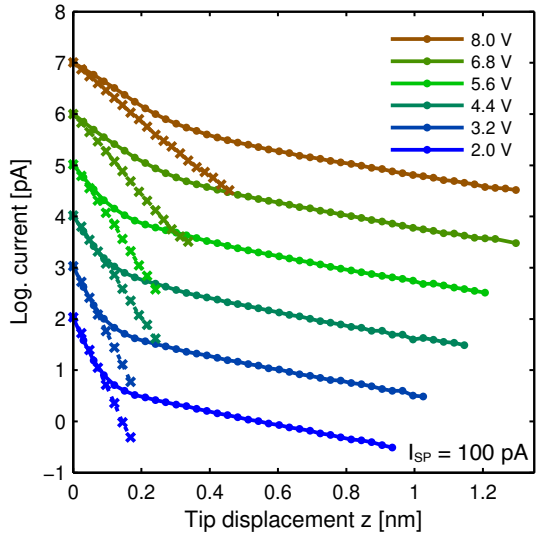

Fig. 5.11: Comparison of current-distance dependencies with (dots) and without (crosses) illumination of the tunnel junction for six different bias voltages. In the former case the average laser power is $P = 3.4\,\mathrm{mW}$ (same data as in Fig. 5.5(a)). The y-axis has a logarithmic scale. For clarity the curves are shifted vertically and only data points exceeding the noise level are plotted. For simplicity, no displacement correction due to different start points is applied.

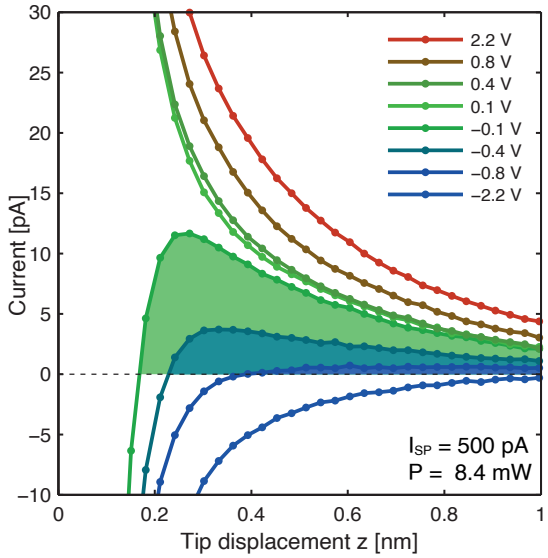

Fig. 5.12: Tip-distance dependencies for positive and negative bias voltages ranging from $-2.2\,\mathrm{V}$ to $2.2\,\mathrm{V}$. The data were measured with laser excitation ($P = 8.4\,\mathrm{mW}$) and a setpoint current of 500 pA. Importantly, $I(z)$ curves for negative bias voltages show a pronounced positive current regime (shaded areas) evidencing electron transport from the tip to the sample, despite the negative setpoint. This rectification effect is clearly observable for bias voltages down to $-1\,\mathrm{V}$. At some point, a negative photocurrent contribution originating from the sample surface conceals the positive current from the tip resulting in a negative net photocurrent. For visibility, only a segment of the actual measured range is shown (no displacement correction is applied).

Field emission resonances

A well-known phenomenon for large bias voltages U_B is the contribution of image states in front of the surface of a conducting sample to the tunneling current [342, 343, 345, 353] (see $\Delta z(U_B)$ spectra in Fig. 5.5(a) and Fig. 5.13). These field emission resonances (FER) are characterized by an increased conductivity for the bias voltage matching the FER energy [298]. Considering a V-shaped potential landscape, such as an image potential, the corresponding electronic states exhibit a hydrogen-like energy spectrum [354]. STM studies found a modification of the image potential energies due to the Stark shift caused by the static electric field between tip and sample [342, 344].

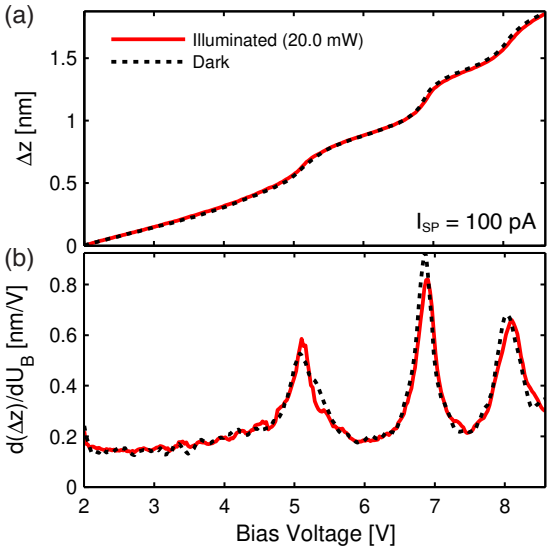

Fig. 5.13: (a) Tip retraction, i.e., start position change, as a function of bias voltage in the range of $2.0 - 8.6$ V with (solid red line) and without (dashed black line) optical excitation of the tunnel junction. The current was kept constant at 100 pA. (b) The derivative with respect to the bias voltage of the curves in (a). Image potential states are evident by the three peaks at 5.0 V, 6.9 V and 8.0 V. Apparently, the fs-laser pulses do not have a strong impact on the curves, especially, the position and shape of the field emission resonances are unaffected.

The FER appear at bias voltages of 5.0 V, 6.6 V, and 7.7 V, as evident from the peaks in the $\mathrm{d}(\Delta z(U_B))/\mathrm{d}U_B$ spectrum (bottom inset of Fig. 5.5(a)). The increased conductivity at the resonances causes slight deviations from the typical exponential form in the regular tunneling regime (e.g., 6.8 V and 8.0 V in Fig. 5.5(a)). The potential sensitivity of the FER spectrum (and as a consequence the dependency from the tip-sample distance) qualitatively explains the curve shape deviations.

Near-field enhancement

The electromagnetic field enhancement of a tip-sample system illuminated with a plane wave E_0 propagating in x'-direction and polarized along the z'-direction (inset of Fig. 5.14) can be modeled with a sphere of radius R_T representing the tip apex in front of a surface. The electromagnetic response of the sphere is described by a dipole moment. This, in turn, induces its image dipole in the sample from which an effective dipole moment can be calculated [277]. The superposition of both dipolar fields with the incident plane wave gives the total field distribution [72]. Evaluating the field at the tip apex ($x' = 0$, $z' = z_{\mathrm{gap}}$)

delivers an algebraic relation for the z'-component of the total field $E_{\mathrm{nf}} \sim (z_{\mathrm{gap}} + R_T)^{-3}$ [281]. Figure 5.14 presents the tip-sample distance dependency calculated with the coupled dipole model (CDM) for a nonlinear process ($\sim |E_{\mathrm{nf}}|^{2n}$) of the order of $n = 2.5$ and tip radii between 5 nm and 100 nm.

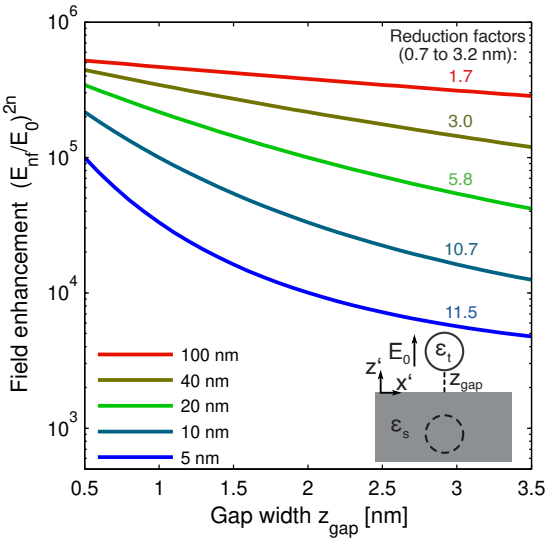

Fig. 5.14: Distance dependency of the plasmonic field enhancement (gap plasmon) $(E_{\mathrm{nf}}/E_0)^{2n}$ calculated with a coupled dipole approximation for tip radii between 5 nm and 100 nm. Dielectric functions for the gold tip (ε_t) and copper sample (ε_s) for a wavelength of 785 nm have been taken from [82]. Note that we incorporated the nonlinear order of $n = 2.5$ extracted from the experimental data. The numbers indicate the reduction factor between 0.7 nm and 3.2 nm, which is the experimentally investigated interval.

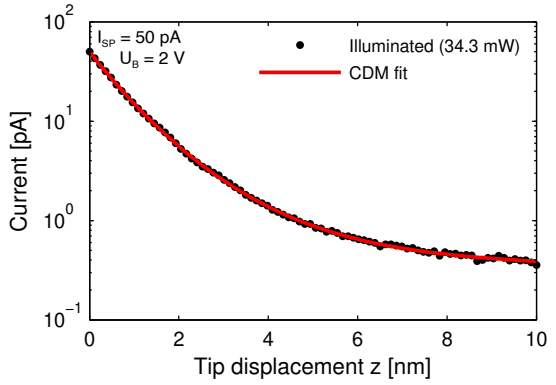

Fig. 5.15: Current-distance dependency (black dots) for higher-power gap illumination (34.3 mW). The observed current decay length is much longer compared to the low-power measurements in Figs. 5.4 and 5.5. At large displacements the current converges to an effective constant value of 0.4 pA. Importantly, there is no regular tunneling at the set-point value. The coupled dipole model (CDM) fits a nonlinear order of $n = 4.4 \pm 0.2$ and a tip radius of 28 ± 2 nm (red line).

Transport model

For the calculation of the transmission probability T, a one-dimensional barrier model, composed of the three regions (tip, gap and sample) is used (Fig. 5.7(a) and Fig. 5.16). The tip and sample are assumed to be field free, i.e., constant potentials of $U_{0,T} + eU_B$ and $U_{0,S}$ for the tip and sample ($U_{0,j}$ is the inner potential), respectively. The total potential $V(z')$ inside the gap is the result of the superposition of the image potentials for both tip and sample, and the linear potential drop due to the bias voltage and the work function differences. Effective surface positions for the tip and sample are applied to fulfill continuous boundary conditions at $z' = 0$ and $z' = z_{\mathrm{gap}}$ [298, 355]. Within a scattering approach, the Schrödinger equation is solved numerically by the Numerov method with the usual assumption of continuously differentiable wave function transitions [297, 298]. From the complex wave function ampli-

tudes the transmission probability is calculated [350]. A schematic illustration of the real part of a wave function is given in Fig. 5.7(a): regions with $E > V(z')$ (tip and sample) are characterized by an oscillatory waveform while the wave function inside the gap ($E < V(z')$) decays exponentially.

Both, tip and sample material, are assumed to have a constant local density of states. The sample temperature is set to 0 K.

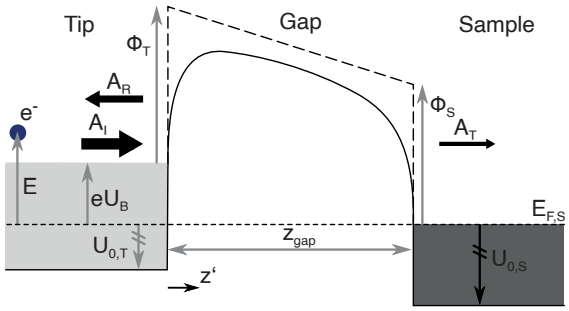

Fig. 5.16: Scheme of the one-dimensional potential barrier model used for the calculation of the electron transmission probability. The complex amplitudes of the incoming A_I, reflected A_R and transmitted A_T wave function are illustrated as black arrows. The applied values for the work functions and inner potentials of tip and sample are listed in Tab. 5.1.

Name	Symbol	Value
Sample work function	Φ_S	4.5 eV
Sample inner potential	$U_{0,S}$	−7.0 eV
Tip work function	Φ_T	5.1 eV
Tip inner potential	$U_{0,T}$	−9.2 eV
Sample Fermi energy	$E_{F,S}$	0 eV

Tab. 5.1: The material parameters used for the transmission probability simulation.

The optimization procedure of the free parameters in the effective occupation function was implemented in Matlab. In advance, the absolute gap width z_0 was fitted for a representative data set and has been fixed for all following simulation iterations. In addition, a slight offset of the order of a few tens to a few hundreds of meV was added to the energy intervals E_j in order to match the actual work function of the tip. We found that the energy widths ΔE_1 and ΔE_2 – corresponding to the temperature of the two photo-driven contributions to the effective occupation distribution – attain values of several tens to a few hundreds of meV, which is equivalent to $1000 - 2000$ K. These high values are necessary to somewhat flatten out the effects of scattering and field emission resonances.

5.4 Challenges of the combination of a fs-laser with an ultrahigh vacuum STM

The central technical development of this work was the successful combination of an ultrahigh vacuum (UHV) low-temperature STM with a pulsed fs-laser source. In the following, we focus on the challenges which occurred during the setup development and the applied solutions. The major objective is the prevention of laser focus motion relative to the tunnel junction and the simultaneous isolation of the STM from mechanical vibrations within the bandwidth of the measurement electronics (1 kHz). Air pressure variations and floor movements are responsible for such vibrations [267]. Additionally, temperature fluctuations and laser beam misalignment cause focus displacements [356].

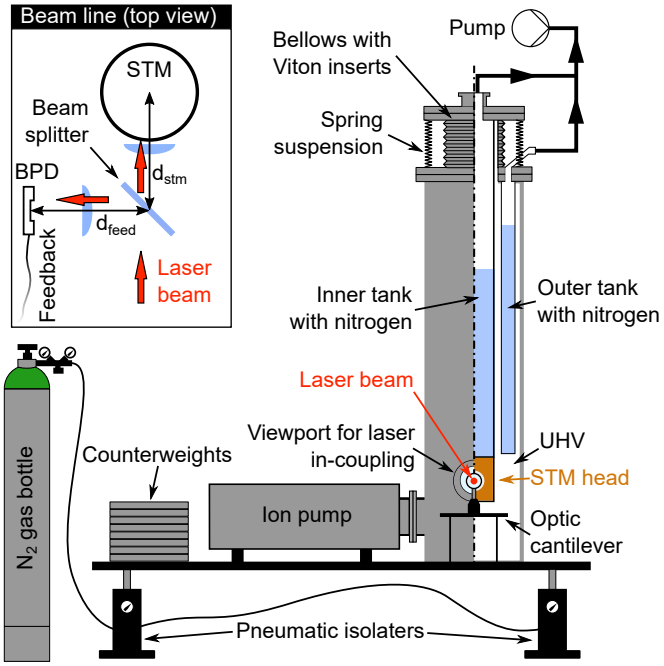

Fig. 5.17: Sketch of the STM experiment. Only the parts important to the focus stabilization are indicated. The sectional drawing of the STM shows the two-chamber cryostat consisting of the heat-shielding outer tank and the inner tank with the attached STM measurement head. Both are cooled with liquid nitrogen in our experiments. We setup several optimization procedures in order to achieve simultaneous vibration isolation and spatial stability of the focus with respect to the STM junction (see text). The inset presents a simplified illustration of the beam line on the optic cantilever. A beam splitter branches the incoming laser beam into a feedback arm and an STM (measurement) arm. The former is stabilized by a beam position detector (BPD) that feedbacks the beam displacement to a piezo actuated mirror on the optic table (not shown). In order to achieve STM-focus stabilization the beam splitter-BPD distance d_{feed} and the beam splitter-STM d_{stm} distance must be identical.

Figure 5.17 presents a schematic illustration of our setup. The standard damping technique is the utilization of pneumatic vibration isolators carrying the STM platform (also used in our experiment). A second damping stage is provided by a two-chamber design for cryogenic cooling: The inner tank is thermally shielded by the outer one, thus cooling

of the inner chamber by helium is possible. The measurement head is attached to the inner tank that is suspended with steel springs to the outer tank and additionally damped by elastomer (Viton) inserts. This strongly suppresses the vibrational power transferred to the measurement system over a broad spectrum. The residual low-amplitude coupling, especially in the sub-Hz regime, does normally not affect the STM performance and atomic resolution is routinely achieved using this damping technique in combination with cryogenic cooling of the apparatus [267]. However, when a laser focus of micrometer-size needs to be steadily positioned on the STM junction even micrometer movements on a second to minute timescale can have a strong impact.

Since we cannot establish a rigid mechanical connection of the laser table to the STM head without significantly corrupting the STM performance, we followed two strategies to combine vibration damping with a sufficient beam focus stability. On the one hand, we reduced the residual inner tank movement to a minimum level by optimizing the mechanical isolator system. On the other hand, we compensate the relative motion between the laser beam and STM platform by setting up an active focus stabilization system. The mechanical optimization consists of three steps (Fig. 5.17):

1. Balancing the system's center of mass with counterweights increases the damping.

2. The pneumatic isolators are operated with compressed nitrogen from gas bottles (the in-house compressed air system is perturbed by pressure fluctuations).

3. Seething of the fluid nitrogen in the cryogenic tanks is suppressed by solidifying the fluid. This is done by reducing the vapor pressure.

Stabilizing the focus is achieved by splitting the beam line on the optic cantilever into two branches (inset in Fig. 5.17 and Fig. 5.9). A beam position detector placed in one of the arms monitors lateral focus displacements with respect to a setpoint position. These deviations are compensated by a feedback controlled piezo-actuated mirror placed on the optical table. This system stabilizes the focus at the position of the feedback detector. Consequently, we achieve a simultaneous stabilization of the STM beam if the optical pathways of the feedback and STM arm are identical ($d_{\mathrm{stm}} \approx d_{\mathrm{feed}}$).

The impact of the mechanical and beam line optimization is measured by a second beam position detector placed in the measurement beam arm on the STM platform, which monitors the horizontal and vertical focus position. In Fig. 5.18 the focus position is plotted as a function of time, before (a,c) and after (b,d) the stabilization measures were taken. In general, the traces (black curves) measured before the optimization had been implemented exhibit noise on a (sub)-second timescale with peak-to-peak values of the order of the focus diameter ($\sim$ 20 µm) (left panels). Furthermore, a shift of the mean position of the laser (red lines) on a minute timescale is observed resulting in a displacement of 15 µm in the vertical direction after 60 min. We find a striking reduction of the focus deviations due to the implemented optimization for both the fast and slow motion (see (b) and (d)). The noise

– measured as the standard deviation calculated from the curves corrected for the long-time trend (red shaded area in Fig. 5.18) – is reduced by a factor of $\sim 3-4$ to a minimum[6] of 1 µm. The almost linear trend lines correspond to a shift of ~ 3 µm (horizontal) and ~ 6 µm (vertical) after 210 min.

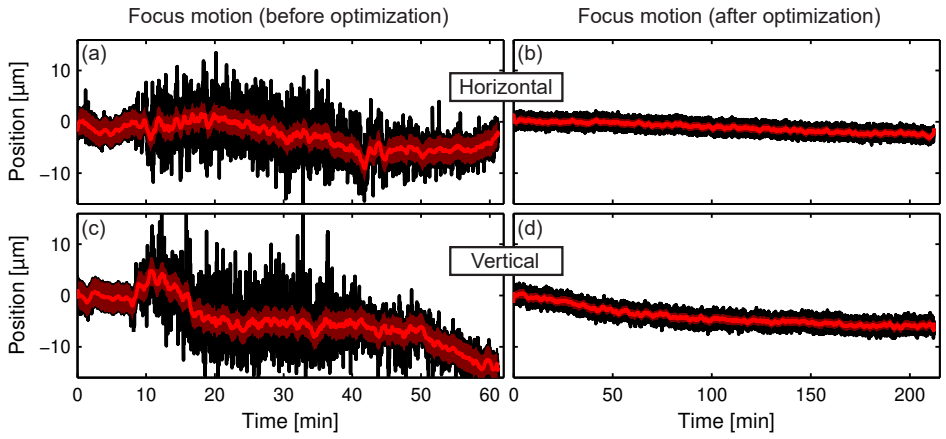

Fig. 5.18: Time traces of the laser focus position measured with a beam position detector placed in the STM beam arm at the same focal distance as the STM center (cf. inset in Fig. 5.17). (a,c) Temporal evolution before the stabilization measures were realized. The beam deviation in the horizontal (a) and vertical direction (c) is dominated by noise of the order of 20 µm measured peak-to-peak. Additionally, an erratic trend (red solid lines) on a minute timescale demonstrates the focus displacement reaching 15 µm after one hour. The standard deviation (corrected for the trend line) is of the order of $3-4$ µm (red shaded area). (b,d) Temporal evolution after the stabilization measures were realized. In comparison to (a,c), the noise as well as the long-term shift is strongly reduced by the optimization (same y-scale as in (a,c)) measured for 3.5 h. The noise is of the order of ~ 1 µm and the almost linear trend (red line) corresponds to a change rate of $15-20$ nm per minute. The sampling rate was 0.5 Hz and 1 Hz for (a,c) and (b,d), respectively.

Deviating optical pathways of the feedback and STM laser arm, non-ideal beam alignment, different optic elements, and temperature fluctuations are inevitable and might be responsible for the residual focus shift (right panels Fig. 5.18). Presumably, it may be prevented by implementing a second pair of beam position detector and piezo-actuated mirror, hence this would adjust not only for one position (the focus) but for the entire beam line. Moreover, we can only actively compensate for the relative movement of the STM platform and the outer chamber; there is a not quantifiable motion of the measurement head attached to the inner tank. As we demonstrated in sec. 5.3, this does not prevent stable and reliable measurements. However, during the experiments we noticed a slow shift of the beam relative to the tunnel junction that might be attributed to the vaporizing of the nitrogen and the accompanied lifting of the inner tank. Thus, a readjustment of the beam position was necessary each 20 min to 30 min. This lifting reaches several millimeters over the entire standing time of the cryo-setup (approximately 72 h) requiring a careful check before starting the measurements. The Appendix 7.5 provides a description of a setup that is designed to circumvent this problem.

[6]These values are close to the resolution of the beam position detector specified to be 0.75 µm by the manufacturer (Thorlabs PDP90A).

CHAPTER 6

Conclusion and outlook

Controlled guiding, concentration, and conversion of electromagnetic energy in nanoscale metal structures are central objectives in the field of nanoplasmonics. Nanostructures feature different electromagnetic wave modes linked to the collective oscillation of the electron gas among which surface plasma oscillations represent an outstanding class. These surface modes are present, for example, at metal-vacuum interfaces, as the two general types of localized and propagating surface plasmon polaritons (LSPs and SPPs) (cf. sec. 2.1). A conical metal tip with a nanometric apex (nanotip) represents an exceptionally multifunctional plasmonic nanostructure, since both wave manifestations – LSP and SPP – can exist in the apex and in the shaft. Although these tips are used in many scanning probe and electron-beam instruments as light and electron sources, a complete physical understanding of the LSP and SPP mode evolution has yet not been developed. In this thesis, we investigated gold nanotips in three experimental studies (chaps. 3, 4, and 5) in order to achieve deeper insights into the mechanisms of surface plasmon excitation, propagation, and the nonlinear conversion to photo-driven currents.

SPP propagation along gold nanotips. SPPs propagating along nanostructure interfaces represent an important mechanism of electromagnetic waveguiding: the structures can be used to transfer, distribute, and concentrate the electromagnetic energy associated with the mode that is bound to the interface [186, 187, 357]. Many applications in nanoplasmonics rely on the customization of sample designs to manipulate the SPP. Hence, this permits to control the energy flux and the energy transfer into other forms [22, 37]. A metallic nanotip provides SPPs gradually transforming (nanofocusing) into nanoscale confinement at the apex (cf. sec. 3.1) [35, 36, 190, 191].

In the first study presented in chap. 3, we investigated the SPP waveguiding properties of free-standing gold tips with small opening angles ($\sim 10 - 15°$) in a transmission electron microscope (TEM) by measuring electron energy loss spectra (EELS) of the electrons closely traversing the nanostructure. The transient electromagnetic field of the tightly focused electron-beam represents a locale probe at the sample position that induces a polarization in the material acting back on the electron which results in a loss of kinetic energy (cf. sec. 2.1.3). Thus, SPP modes can be imaged as a function of space (electron-beam position) and frequency (energy loss). We observed distinct standing wave patterns with characteristic wavelengths depending on the energy loss.

An analytical model has been developed in Ref. [66], which describes the observed energy loss profiles along the tip surface by including several SPP azimuthal mode orders m representing different cross-sectional field distributions (cf. Fig. 3.3). Most importantly, we found the fundamental wave with $m = 0$ (field is constant in the azimuthal direction) to be reflected at the tip truncation leading to the pronounced standing wave pattern. Moreover, the resulting reflection coefficient (i.e., the complex-valued amplitude modifier of the reflected mode) is close to unity. In other words, the SPP is reflected with a nearly 100% efficiency implying a low energy dissipation (generation of heat) in the nanometric apex region. Notably, higher-order modes only contribute with a weakly modulated loss probability to the measured signal somewhat distant from the tip end (cf. Fig. 3.8 and Fig. 3.13).

The relative contributions to the total energy loss due to the fundamental, reflected and higher-order modes critically depend on the tip opening angle, as we have pointed out in sec. 3.4 (cf. also Refs. [66, 219]). Larger opening angles cause radiation to the far-field once the fundamental SPP mode approaches the apex in a process of a breakdown of the adiabatic condition (cf. Eq. 3.3). Hence, the mode energy is not transferred to a back-propagating wave. In contrast, higher-order modes are found to be coupled to the far-field independent of the tip opening angle [217].

These insights may permit designs of metal tip nanostructures for specialized purposes. For example, focused ion beam milling can be used to reduce radiation leakage from the apex by reducing the tip opening angle or to manipulate the SPP dispersion and associated emission spectra by specialized resonator or coupling designs [232, 358, 359].

SPP-driven electron gun for electron-beam experiments. Ultrafast electron emitters are used to probe charge and lattice dynamics in time-resolved electron microscopy and diffraction schemes. Here, electron pulses of fs- to ps-duration are released from the emitter cathode by ultrashort laser transients [52, 53, 55]. Point-like sources, such as metal tips with apex radii of the order of a few nanometer, are ideal for this purpose because electron pulses emitted from the tip end can provide a high degree of transversal and longitudinal coherence when directly illuminating the tip apex [147, 210].

In the second experiment (chap. 4), we investigated multiphoton photoemission from the tip apex that is driven via SPP wave packets coupled to the tip surface and we compared

this with direct apex excitation. In both cases each electron absorbs the energy of four photons (each $\sim 1.5\,\mathrm{eV}$) from the plasmon near-field and overcomes the vacuum barrier (cf. sec. 2.3). The photo-emitted current and its projected emission profile is recorded by a micro channel plate (MCP) detector. A grating coupler milled into the taper surface at a distance of a few tens of micrometer away from the apex launches the SPP modes. We inserted the nanostructure into a modified field emission gun, which allows us to precisely control the electrostatic environment of the tip and hence to manipulate the trajectories of the emitted electrons. Most importantly, we can suppress emission from the tip shaft (e.g., the grating coupler) apart from the apex. As a matter of fact, the efficiency of the SPP-driven operation mode is distinctly higher compared to the direct apex illumination ($\times 150$ electron yield for grating optimized conditions), as has also been found in the Refs. [50, 51, 180].

Besides the better over-all coupling efficiency, SPP-driven electron guns have the advantage of a strongly reduced background illumination, since the diffraction limited laser focus spot is tens of micrometer away from the apex. This is vital in experimental setups in which the electron emitter needs to be placed in close proximity to a sample, such as point-projection microscopy (PPM). In PPM, a point-like source is placed in a micrometer distance to the sample. Emitted charges project an image of the sample with a magnification depending on the emitter-sample-distance onto a two-dimensional detector (analogue to the MCP in our experiment) [360]. Recently, PPM was combined with ultrafast electron emission from tips providing a spatiotemporal resolution on the 10 nm and 100 fs scales [247, 249, 361]. The time resolution is limited because of dispersive pulse broadening suffered over the comparatively large tip-sample distances of $\gtrsim 10\,\mu\mathrm{m}$ required to avoid sample illumination by the diffraction limited focus spot placed on the tip apex [51]. The implementation of SPP-based apex near-fields circumvents this requirement by a remote release of charges via grating couplers [50–52, 210]. This allows significantly smaller tip-sample distances: Using a distance of $\sim 3\,\mu\mathrm{m}$ measurements with doped InP nanowires and Au nano-resonators have demonstrated a time resolution of $\sim 10\,\mathrm{fs}$ (with a magnification of $\times 3 \cdot 10^4$) [51, 52].

SPP-driven electron sources potentially improve the spatiotemporal properties of experimental schemes based on low-energy electron transmission [210], such as ultrafast PPM and low-energy electron diffraction probing the electron and lattice dynamics of two-dimensional materials [55, 249]. In addition, electron microscopy and diffraction may benefit from the better coupling efficiency. For a given electron yield, less laser intensity is required and higher laser pulse repetition rates are possible; reducing the measurement acquisition time [210]. An SPP-based electron gun may also be used to customize the SPP wave packets in order to tailor the electron wavefront [12, 129, 146, 266, 362].

Photocurrents in a tunnel junction. As a very important aspect, nanotips provide a local hotspot of a high field enhancement and electromagnetic energy concentration in tip-gap-substrate systems (cf. sec. 5.1). These hotspots have been implemented very successfully in tip-enhanced Raman spectroscopy (TERS) leading to a strong increase of the signal-to-

background ratio [47, 48, 321, 363], in apertureless near-field scanning optical microscopy (A-NSOM) in which the field localization results in an in-plane resolution of $\lesssim 10\,\mathrm{nm}$ [43–46], and in scanning tunneling microscopy (STM) [327–331]. In STM, the LSP decay is accompanied by an increased local emission of luminescence from the tip-sample contact. Recent STM studies based on the laser excitation of the contact region also demonstrated a strong increase in photochemical reaction rates due to the near-fields [304, 306, 307].

In chap. 5, we explored the prototypical model system of a metal tip in close proximity to a flat metal sample, as it is present in many of the mentioned applications. The illumination of the tip-sample junction with a fs-laser leads to a near-field-driven photocurrent I_{pc}. We are able to distinguish I_{pc} from the regular tunnel current by its distinctly longer decay length ($\times 4-8$) in current-distance measurements ($I(z)$ curves) covering absolute gap widths ($z_{\mathrm{gap}} \sim z$) from $\sim 0.7\,\mathrm{nm}$ to $\sim 5\,\mathrm{nm}$. By adjusting the tip-sample distance, bias voltage and laser power the control of the relative contribution of the photo-driven compared to the regular tunnel current is possible. We analyzed the current decay by means of a coupled dipole model in order to approximate the apex LSP coupling with the sample (cf. sec. 5.1). The resulting near-field (gap mode) exhibits a monotonic reduction with increasing gap width. However, the calculated decay fits neither qualitatively to the exponential curve nor quantitatively to the reduction values found in the measurements. Instead, we can explain the photocurrent decay by the gradual change of the potential barrier between the tip and the sample upon increasing the gap width from $\sim 0.7\,\mathrm{nm}$ to a few nanometers: A transport model basing on electron transfer through the barrier including the image potentials of the system provides the transfer probability $T(E, z_{\mathrm{gap}})$ (cf. sec. 5.2). Applied to the experimental data, it allows to extract an effective, time averaged electron distribution $f_{\mathrm{eff}}(E)$. On this basis, we find electron states around the potential barrier maximum as the most contributing channels to the observed photocurrent.

As we have outlined by Fig. 5.15, the photocurrent decay is dominated by the plasmonic near-field reduction when retracting the tip to distances of the order of 10 nm. Very recently, this has been shown and systematically investigated in Ref. [364] by studying the electron transfer between two opposing tips under fs-laser illumination. In this experiment ($8\,\mathrm{nm} < z_{\mathrm{gap}} < 20\,\mathrm{nm}$), electron emission is given by photoemission *over the barrier*. Whereas in our experiment ($z_{\mathrm{gap}} < 5\,\mathrm{nm}$) the current is dominated by regular tunneling from the Fermi edge and by transfer of electrons that are optically excited to the *vicinity of the barrier maximum* (including also a transfer over the barrier). Hence, for nano-gap systems, the current composition and its decay with increasing gap width shows a transformation from being governed by the reduction of the transfer probability towards being governed by the reduction of the plasmonic near-field.

As we demonstrated in Figs. 5.6(c) and (e), nonlinear photocurrents are able to resolve topographic features with nanometer resolution. The lateral (in-plane) extension of the near-field has recently been investigated by plasmon-driven photochemical reactions in Refs. [304,

306, 307, 365]. The number of molecular interactions was found to drop to zero for lateral distances $\gtrsim 5$ nm from the apex, hence confirming the strong field localization. Furthermore, the process depends linearly on the laser intensity [306]. In contrast, nonlinear processes such as the transfer of electrons which absorbed two photons [314] may significantly increase the locality of surface photochemistry in STM. Different experimental approaches, for example, tip-enhanced Raman spectroscopy [47, 48, 309, 321, 366, 367] and scanning tunneling luminescence [310, 311, 332, 333, 368, 369] have already demonstrated single molecule sensitivity on diverse molecule-substrate systems exposed to apex LSPs provided either by junction illumination (TERS) or by inelastic electron tunneling (luminescence).

The effective population distribution $f_{\mathrm{eff}}(E)$ extracted in our analysis gives valuable insights into the electron excitation mechanism and indicates that multiphoton absorption from the plasmonic near-field followed by electronic relaxation processes (cf. sec. 2.2) are responsible for the photocurrent. Experimental strategies relying on temporal and spectroscopic schemes potentially give further information of the dynamical interactions of the electrons, on the one hand, and the electromagnetic near-field, on the other hand.

Electron population dynamics can be investigated by double-pulse experiments [150, 173, 370, 371]. Our setup can be extended in such a way that it provides $I(z, t_d)$ data sets for different pulse delays t_d (cf. Fig. 5.10). In combination with the presented transport model this might be used to extract electron distributions $f(E, t_d)$ as a function of time.

In scanning tunneling spectroscopy (STS) the local density of states of the sample is probed in the form of differential conductance ($\mathrm{d}I/\mathrm{d}U_B(U_B)$) spectra as a function of the bias voltage U_B [296]. By exploiting STS in a comparative way (fs-illumination vs. unilluminated reference measurements), we may address the question of which electronic states are populated in the sample once the optically excited electrons have transferred.

Additionally, the implementation of an optical spectrometer analyzing the light emitted from the tunnel junction could be used to measure electroluminescence (electron in-photon out processes) [372] and photoluminescence spectra $S_{\mathrm{lum}}(\omega)$ (photon in-photon out processes) [281]. These are related to the localized surface plasmon resonance in the gap and may be used to compare photon emission induced by inelastic electron tunneling and plasmon radiation processes [373, 374]. Ultimately, from $S_{\mathrm{lum}}(\omega, t_d)$ measurements it is possible to retrieve the near-field time structure $E_{\mathrm{nf}}(t)$ including its plasmonic lifetime [140].

STS and time-resolved STM mapping require a spatial overlap of the laser focus and the STM junction that is temporally stable for at least several hours. This might be provided by a sophisticated focus stabilization approach in which a beam position detector is attached to the inner tank of the STM. Thus, the residual motion of the measurement head with respect to the laser focus could be compensated (cf. sec. 5.4). Moreover, the application of a two-laser configuration – consisting of a measurement and position tracking beam line – may give additional flexibility to the setup. The Appendix 7.5 presents some details and a schematically illustration of this proposal.

Perspective of a local excitation microscope

The physical and chemical processes involved in the excitation of an atomistic species adsorbed on a surface (e.g., atom or molecule) exhibit a strong dependency on its atom-scale environment (e.g., step edges, vacancies, or neighboring atoms) [57, 58, 375]. This site-specificity demands imaging and spectroscopy approaches that can investigate and manipulate surface mechanisms (and their dynamics) on a single-atom or single-molecule level [58, 59]. A local excitation microscopy scheme involving complementary electron, field, and photon interactions may contribute to a profound picture of chemical reactions evolving on substrate surfaces.

In the field of scanning tunneling and atomic force microscopy, striking developments enabled researcher to explore different aspects of site-specificity such as imaging of intramolecular bonds [376–381] and electroluminescence [309–311, 332, 333, 368, 369, 382] on a sub-molecular level, interactions between spins and single atom magnets [383–392], and controlled manipulation of molecules including surface chemical reactions [57, 58, 393–396]. Prevalently, these experiments rely on electrons (tunnel current) and electrostatic fields (bias voltage) to drive the mechanisms under investigation. However, photons (electromagnetic fields) have also been added to the toolbox of scanning probe microscopy and spectroscopy. Specifically, Raman scattering [47, 48, 320, 321, 366], photochemistry (isomerization, tautomerization, dissociation, and desorption) [304–307, 365, 366, 397] and fs-dynamics [269, 303] of single molecules have been investigated by illuminating the tip-sample contact with (pulsed) laser light. These inspiring studies demonstrate the exploration of local surface phenomena on an atomic (and partially on a femtosecond) scale. The realization of a fs-laser-STM combination (fs-STM), as we have demonstrated in chap. 5, is yet not routinely operated due to experimental challenges involving thermal instabilities and parasitic effects (e.g., substrate excitation or background signals) [61, 62].

Nanofocusing (cf. chaps. 3 and 4) might render a significant step towards a versatile fs-STM setup. Here, the electromagnetic energy of grating coupled SPPs is highly concentrated at the apex without directly illuminating the tip-sample contact, as schematically illustrated in Fig. 6.1. Near-fields driven by a pulsed laser could allow to study reversible, optically driven mechanisms in a double-pulse approach (cf. Refs. [269, 303]) and to nonlinearly excite molecules (e.g., by frequency mixing or hot electrons [133, 398, 399]). Similar approaches have already been implemented in TERS [36, 41, 208, 209], A-NSOM [45, 46, 203–207], and time-resolved A-NSOM [39, 40].

This nanofocusing setup provides several advantageous features: (1) Grating coupled-SPPs exhibit a broadband coupling efficiency reaching from the visible to the near-infrared energy scale [35, 45, 128]. This facilitates SPP pulses of a few femtoseconds arriving at the apex [45, 50–52, 129], stronger enhanced fields compared to direct illumination [41, 50, 51, 67], and spatiotemporal tailoring of the SPP wave package [129, 266, 362]. Consequently,

this may allow for ultrafast time-resolved measurements and lowers the necessary incident laser power required to drive (reversible and nonlinear) processes like, for example, charging [270, 314], molecular vibrations [303] or photodissociation [365, 375]. (2) An SPP propagation length of several tens of micrometers is possible with quasi-single crystalline gold tapers (cf. sec. 4.2) [45]. Hence, background signals because of far-field scattering are strongly reduced by the spatial separation of the SPP excitation from the gap region [204]. (3) The tip acts as an effective SPP mode filter: Only the fundamental (azimuthally constant) mode with a well-defined polarization reaches the apex (cf. sec. 3.3) [203, 400]. (4) For sufficiently small opening angles, the SPP mode reflection at the apex dominates other processes such as local absorption or far-field radiation (cf. sec. 3.4) [65, 217, 219]. This might reduce thermal instabilities due to energy dissipation in the nanometric apex region.

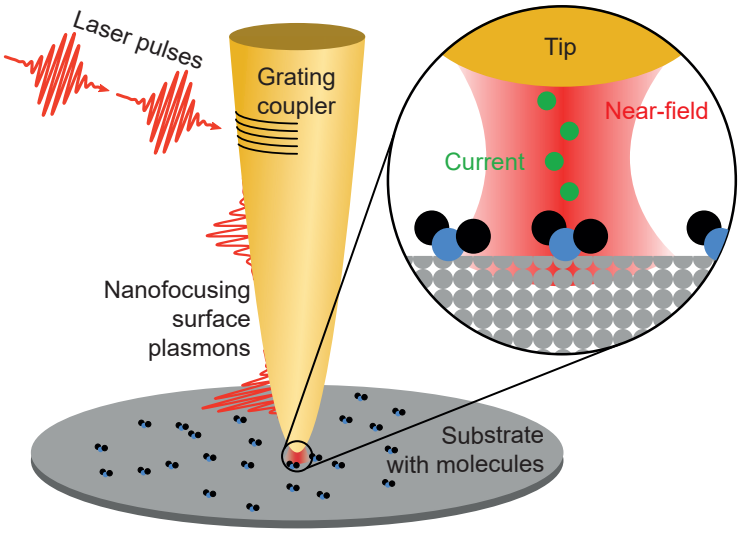

Fig. 6.1: A local excitation microscope for the investigation of individual molecules. Surface plasmons are launched via far-field illumination of a grating coupler several tens of micrometer away from the excitation region at the apex-sample contact. The propagating surface plasmons are nanofocused to a localized near-field (inset). This may allow to excite single molecules.

In addition, the experimental scope might be extended by modifying the nanotip to specific functionalities. The gold nanotips used in our studies have the advantage to be inert under atmosphere and sustain their clean surface. However, other materials can provide surface plasmons with ultraviolet energies, whereas plasmonic mode propagation in gold is suppressed by d-band transitions for energies $\gtrsim 2.2\,\mathrm{eV}$ [134]. Aluminum and silver tips with grating couplers [205, 209] exhibit a spectrum extending the excitation energies to $\sim 3-4\,\mathrm{eV}$ which is an important range in surface photochemistry [399, 401]. Tungsten tips (providing a high mechanical durability) have also be equipped with a grating for surface plasmons in the mid-infrared region [210] that might be used to excite vibrational modes in molecules [57]. Furthermore, the functionalization of the tip (i.e., the adsorption of a foreign atom or molecule at the apex) can give sensitivity to physical or chemical processes which are not addressable in conventional STM and AFM. Specifically, magnetic spin-interactions

with atoms and chemical bonds of molecules can be studied by functionalized tips in scanning probe experiments [376, 377, 383, 385].

In this context, the present thesis represents a crucial step forward by establishing the combination of a fs-STM with plasmonic gold tips and by providing key insights into relevant physical processes evolving in tip nanostructures. The fs-laser excitation of the STM tunnel contact and the accomplishment of challenges regarding thermal and pointing instabilities have been achieved. Control mechanisms governing surface plasmon waveguiding and nanoscale concentration have been investigated in the light of linear and nonlinear interactions in the tip apexes.

We expect that the localized excitation with nanofocused SPPs in a scanning tunneling microscope can feature a significant contribution to surface photochemistry by connecting linear and nonlinear excitation pathways involving electrons, photons, electrostatic and electromagnetic fields. This may give a comprehensive set of complementary information on the site-specific nature of adsorbed molecules.

CHAPTER 7

Appendix

7.1 Generalized Fowler-DuBridge theory

Light with a photon energy of $\hbar\omega$ incident on a solid object excites the electrons in the surface. Energetically elevated electrons can be emitted from a solid state surface resulting in an electron flux I_{total}. Depending on the excitation process thermionic emission (transient or static heating of the electron gas) and photoemission (absorption of photon quanta) can be distinguished. The first theory that included both phenomena was developed by Fowler and DuBridge in the 1930s [157, 158]. Their theory bases on the following assumptions: 1) The electron occupation is determined by the Fermi-Dirac distribution and the electron momentum is uniformly distributed. 2) The likelihood of an electron to absorb the energy of a photon is independent on the initial electronic state. 3) Emission occurs if the kinetic energy $E_\perp$ linked to the momentum component normal to the surface exceeds the work function Φ of the solid. 4) The absorbed energy only increases $E_\perp$. 5) The number of electrons emitted per absorbed photon quanta is proportional to the number of electrons per unit volume whose energy $E_\perp + \hbar\omega$ exceeds Φ [162].

Originally described for linear photon absorption, the Fowler-DuBridge theory was generalized to include also nonlinear absorption processes [159, 161]. In this case, the total current I_{total} is decomposed in a sum over different components I_n each of which is associated with a particular absorption order n:

$$I_n = a_n \left[\frac{e}{\hbar\omega}(1-R_\omega)I_\omega\right]^n T^2 A_C \Lambda \left(\frac{n\hbar\omega - \Phi}{k_B T_e}\right),$$

with the material parameter a_n determining the electron emission probability, the Richardson constant A_C, the light intensity I_ω, the surface reflectivity R_ω, and the electron temperature T_e. For $n = 0$ the equation renders the Richardson description for thermionic emission. The term $T_e^2 A_C \Lambda\left(\frac{n\hbar\omega-\Phi}{k_B T}\right)$ governs the number of available electrons that absorbed the energy $n\hbar\omega$ (according to no. 5 of the assumptions stated above) with the function [162]

$$\Lambda\left(\frac{n\hbar\omega-\Phi}{k_B T}\right) = \int_0^\infty \mathrm{d}y \ln\left(1+\exp\left[-y-\left(\frac{n\hbar\omega-\Phi}{k_B T_e}\right)\right]\right).$$

7.2 SPP dispersion relation for cylindrical structures

The electromagnetic eigenmodes of a cylinder of radius R are derived by solving the Maxwell equations in cylindrical coordinates for the inside (described by the permittivity $\varepsilon_t(\omega)$, non-magnetic material) and outside ($\varepsilon_d = 1$ for vacuum) of the structure. In general, the electric and magnetic field components, (E_r, E_φ, E_x) and (H_r, H_φ, H_x), are determined by a set of Bessel J_m and Henkel H_m functions via the scalar function in Eq. 3.1, the mode order m and the wave vector component q in the x-direction. The tangential components of the electric and magnetic field must be continuous in the cylinder surface ($r = R$) providing a transcendental equation [212, 213],

$$\begin{aligned}&\frac{\omega^2}{c^2}\left(\frac{\delta_{x_t} J_m(x_t)}{x_t J_m(x_t)} - \frac{\delta_{x_d} H_m^{(1)}(x_d)}{x_d H_m^{(1)}(x_d)}\right)\left(\varepsilon_t \frac{\delta_{x_t} J_m(x_t)}{x_t J_m(x_t)} - \varepsilon_d \frac{\delta_{x_d} H_m^{(1)}(x_d)}{x_d H_m^{(1)}(x_d)}\right)\\ &- m^2 q^2\left(\frac{1}{x_d^2}-\frac{1}{x_t^2}\right)^2 = 0,\end{aligned} \tag{7.1}$$

with $x_j = q_j R$ and $\delta_{x_j} = \partial/\partial x_j$ denoting to the partial derivative with respect to x_j for the inside ($j = t$) and outside of the structure ($j = d$). The radial wave vector components q_j are given by Eq. 3.2. We applied a numerical root-finding algorithm to solve Eq. 7.1 for a given mode order m, cylinder radius R and energy $\hbar\omega$ in the complex plane. This yields the complex dispersion relation $q_{mR}(\omega)$ for the surface bound eigenmodes of the cylinder. The permittivity data for gold from Ref. [82] is used for this calculation.

7.3 Transition matrix elements M_{if} for elastic tunneling

Bardeen used the time-dependent Schrödinger equation to derive a integral calculation for the transition matrix elements that determine the electron transfer rate from the initial state in the tip to the final state in the sample (cf. Eq. 5.3) [295]. Therefore, he applied the wave functions of the tip $\Psi^t(z',t) = \psi_i^t(z')\exp(-iE_i t/\hbar)$ and the sample $\Psi^s(z',t) = \psi_f^s(z')\exp(-iE_f t/\hbar)$ in a perturbation approach. In particular, he found that only the values of ψ_i^t and ψ_f^s in the separation plane $\mathbf{S} = (x', y', z' = z_{\mathrm{sep}})$ (indicated as the

dashed line in Fig. 5.3(b)) govern the matrix elements,

$$M_{if} = \frac{\hbar^2}{2m_e} \int_{z_{\mathrm{sep}}} \mathrm{d}x' \mathrm{d}y' \left[\psi_i^t(z') \frac{\partial}{\partial z'} \bar{\psi}_f^s(z') - \bar{\psi}_f^s(z') \frac{\partial}{\partial z'} \psi_i^t(z') \right].$$

Here, $\bar{\psi}_i^t$ and $\bar{\psi}_f^s$ are the complex conjugations of ψ_i^t and ψ_f^s, respectively [267].

7.4 Numerov method and transmission probability

We apply a one-dimensional elastic scattering approach to the problem presented in Fig. 5.16 (for the sake of readability some of the following information overlaps with sec. 5.3.9 'Transport model'). The potential is composed of three regions. The tip and sample are assumed to be field-free (the materials used in our investigation are metals) corresponding to constant potentials V^t and V^s, while the gap is characterized by a complex potential shape $V^g(z')$ (see below).

The electronic wave function is represented by monochromatic components $\Psi(z', t) = \psi(z') \exp(-i\omega t)$ oscillating at a frequency of $\omega = E/\hbar$. These must solve the stationary Schrödinger equation,

$$\left[-\frac{\hbar^2}{2m_e} \frac{\partial^2}{\partial z'^2} + V(z') \right] \psi(z') = E\psi(z'), \tag{7.2}$$

for each component. We assume $\psi(z')$ to be composed of a superposition of an incoming $\psi_I = A_I \exp(ik^t z')$ and a partially reflected plane wave $\psi_R = A_R \exp(-ik^t z')$ on the tip side, and a partially transmitted plane wave on the sample side $\psi_T = A_T \exp(ik^s z')$ (cf. black arrows Fig. 5.16). By inserting the plane wave functions into Eq. 7.2, we find the wave vectors $k^t = \sqrt{2m_e/\hbar^2(E - V^t)}$ and $k^s = \sqrt{2m_e/\hbar^2(E - V^s)}$, which depend on the electron energy E and the (constant) potentials V^t and V^s on the tip and on the sample side. Most importantly, the solution ψ_g for the gap region has to be calculated by determining the three complex-valued scattering amplitudes A_I, A_R and A_T with appropriate boundary conditions [294].

Due to the infinitely delocalized plane waves, normalization is not applicable to the wave function and it does not contribute to the solubility of the problem. Instead, we manually set A_T to unity and determine the values of A_I and A_R relative to A_T without loss of generality. This approach reduces the core problem to the determination of ψ_g. Its computation is performed with the Numerov method, which is applicable to the Schrödinger equation if at least two initial values are known [297, 298]. This condition is satisfied by the knowledge of the partial solution in the sample region ψ_T. The coordinate axis is discretized into $z'_j = z'_0 + j\Delta z'$ equidistant sampling points (start point z'_0, step width $\Delta z'$ and integer j).

Therewith, the Numerov method gives wave function values ψ_j at the jth sampling point,

$$\left(1+\frac{\Delta z'^2}{12}k_j\right)\psi_j = 2\left(1-\frac{5\Delta z'^2}{12}k_{j-1}\right)\psi_{j-1} - \left(1+\frac{\Delta z'^2}{12}k_{j-2}\right)\psi_{j-2}, \tag{7.3}$$

with the wave vector k_j at the position z'_j. The full solution of the wave function $\psi(z')$ is found for a given electron energy E by the iterative calculation of Eq. 7.3 in the gap region with continuously differentiable boundary conditions at $z'=0$ and $z'=z_{\mathrm{gap}}$ [350].

The quantum mechanical electron transport is expressed by the (probability) current density [294],

$$J = \frac{\hbar}{2im_e}\left[\bar{\psi}(z')\frac{\partial}{\partial z'}\psi(z') - \psi(z')\frac{\partial}{\partial z'}\bar{\psi}(z')\right]. \tag{7.4}$$

By inserting the calculated wave function $\psi(z')$ in Eq. 7.4, we find J to be composed of an incoming $J_I = \hbar k^t/m_e|A_I|^2$, a reflected $J_R = \hbar k^t/m_e|A_R|^2$ and a transmitted flux $J_T = \hbar k^s/m_e|A_T|^2$. The ratios J_T/J_I and J_R/J_I provide the transmission T and reflection R_R probabilities [294, 402],

$$T = \frac{k^s}{k^t}\frac{|A_T|^2}{|A_I|^2} = \frac{k^s}{k^t}\frac{1}{|A_I|^2} \quad \text{and} \quad R_R = \frac{|A_R|^2}{|A_I|^2}, \tag{7.5}$$

respectively. We implemented this calculation in a Matlab routine that loops over a set of electron energy, gap width and bias voltage. This results in transmission probability data cube $T(E, z_{\mathrm{gap}}, U_B)$.

The total potential $V(z')$ inserted into Eq. 7.2 is composed as follows. We set V^t and V^s to the inner potential values $U_{0,T}$ and $U_{0,S}$, i.e., the minimum energy a charge carrier from the electron gas can have in the respective material (cf. Tab. 5.1) [403]. The inner potentials determine the possible energy range of which the current can be composed. Thus, $U_{0,T}$ and $U_{0,S}$ must attain appropriate high absolute values. However, we found that the specific value has no significant impact on the results, as was also stated in Ref. [298]. The energy scale is given relative to the Fermi energy of the sample set to $E_{F,S}=0$ resulting in $E_{F,T} = eU_B$ for the Fermi energy of the tip (cf. Fig. 5.16).

For the gap potential $V^g(z')$, we assume a homogenous field distribution due to the bias voltage and work function difference between the tip and the sample. This leads to a potential $V_{\mathrm{bias}}(z') = eU_B(1-z'/z_{\mathrm{gap}})$ and $V_{\mathrm{wf}}(z') = \Phi_T - (\Phi_T - \Phi_S)z'/z_{\mathrm{gap}}$ of triangular shape (cf. dashed line in Fig. 5.16). An additional contribution is given by the image potential V^t_{img} and V^s_{img}: An electron inside the gap polarizes the material and self-interacts with this induced polarization. Physically, the electric field of the electron induces a screening surface charge distribution in the electrodes that can be regarded as attractive Coulomb forces ($\propto e^2/z'^2$) between the electron and its positive image charge in the bulk (Fig. 7.1)

[84]. In summary, we apply the total potential [404],

$$V(z') = \begin{cases} V^t = U_{0,T} & z' \leq 0 \\ V^g(z') = V_{\text{bias}} + V_{\text{wf}} + V^t_{\text{img}} + V^s_{\text{img}} & 0 < z' < z_{\text{gap}} \\ V^s = U_{0,S} & z' \geq z_{\text{gap}} \end{cases}$$

with

$$V^g(z') = eU_B \left(1 - \frac{z'}{z_{\text{gap}}}\right) + \left(\Phi_T - \frac{\Phi_T - \Phi_S}{z_{\text{gap}}} z'\right) - \frac{e^2}{16\pi\varepsilon_0} \left(\frac{1}{z' - z^t} + \frac{1}{z_{\text{gap}} + z^s - z'}\right)$$

to calculate the transmission probability (Eq. 7.5). z^t and z^s are introduced as numerically determined effective surface positions in order to prevent singularities owing to the image potentials with the condition $\lim_{z' \to 0^+} V^g(z') = E_{F,T}$ and $\lim_{z' \to z^-_{\text{gap}}} V^g(z') = E_{F,S}$ [298, 355]. Typical values of z^t and z^s are between 0.01 nm and 0.02 nm. The work functions of the tip Φ_T and the sample Φ_S are given in Tab. 5.1.

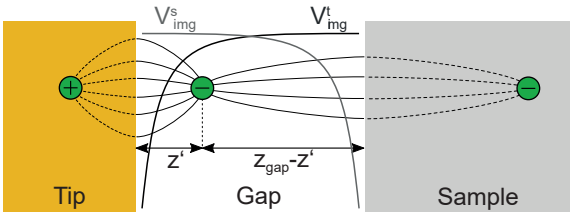

Fig. 7.1: Image potentials of an electron present in the STM junction. The electron polarizes both the tip and the sample material (solid field lines). The resulting surface charge distribution can be regarded as image potentials $V^t_{\text{img}}(z') \propto e^2/z'$ and $V^s_{\text{img}}(z') \propto e^2/(z_{\text{gap}} - z')$ due to Coulomb interaction.

7.5 Novel beam stabilization scheme

In chap. 5 we described the successful combination of a home-built STM with a fs-laser illuminating of the tip-sample contact. We learned about the critical role of the motion of the focus relative to the tunnel junction; a particular challenge consisted in the minimization of this displacement and we are able to stabilize the focus-junction overlap on a 30 min basis (cf. sec. 5.4). After this time period a slight rearrangement of the focus position relative to the tunnel junction is necessary.

Ideally, beam pointing stability is given for several hours, thus facilitating comprehensive spectroscopy mapping experiments under consistent illumination conditions. We identified the residual movement of the inner tank as a severe limiting factor. The presently applied active beam stabilization is not able to monitor and compensate this shifting.

Here, we propose a modified setup in which the beam position detector (BPD) is attached to the bottom part of the measurement head. In this case, the BPD monitors the motion of the inner tank including the tip and sample, as it is illustrated in Fig. 7.2. The piezo-actuated mirror outside the STM compensates for the shift that is measured very close to the tunnel junction.

Furthermore, a two-laser setup consisting of a pulsed measurement beam (red in Fig. 7.2)

and a continuous-wave tracking beam (green in Fig. 7.2) might improve the flexibility and the handling of the setup. Specifically, the tracking laser light is not affected by intentional changes performed on the measurement laser (e.g., polarization, power, or repetition rate modifications). Both lines collinearly propagating through the setup are decoupled in front of the STM viewport, e.g., by means of different polarizations and a polarizing beam splitter, and guided to the tip and BPD, respectively.

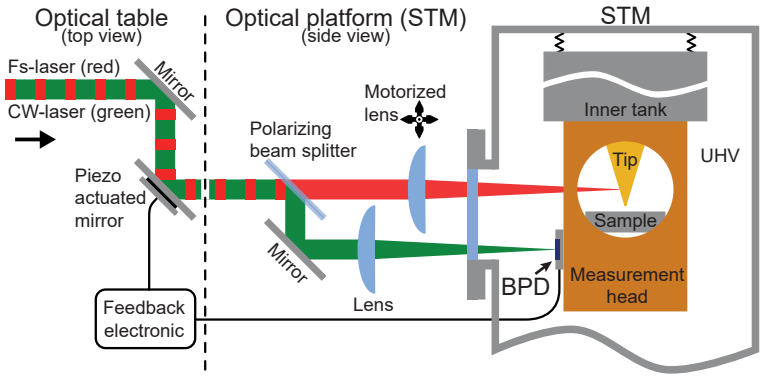

Fig. 7.2: Proposal for a beam stabilization that compensates for the motion of the tip and sample relative to the laser focus. A beam position detector (BPD) is directly attached to the measurement head which is mechanically decoupled from the STM platform. Hence, the focus-junction overlap can be sustained by a piezo actuated mirror controlled by the BPD output. The utilization of a measurement laser (red) and beam tracking laser (green) may give additional flexibility to the system. They are collinearly aligned and decoupled directly in front of the STM viewport.

References

[1] H. Hertz. "Ueber einen Einfluss des ultravioletten Lichtes auf die electrische Entladung". *Annalen der Physik und Chemie* **267** (1887), 983–1000.

[2] A. Einstein. "Über einen die Erzeugung und Verwandlung des Lichtes betreffenden heuristischen Gesichtspunkt". *Annalen der Physik* **322** (1905), 132–148.

[3] W. D. Arnett et al. "Supernova 1987A". *Annual Review of Astronomy and Astrophysics* **27** (1989), 629–700.

[4] A. Heller. "Conversion of sunlight into electrical power and photoassisted electrolysis of water in photoelectrochemical cells". *Accounts of Chemical Research* **14** (1981), 154–162.

[5] B. Genty, J.-M. Briantais, and N. R. Baker. "The relationship between the quantum yield of photosynthetic electron transport and quenching of chlorophyll fluorescence". *Biochimica et Biophysica Acta (BBA) - General Subjects* **990** (1989), 87–92.

[6] H. F. DeLuca. "History of the discovery of vitamin D and its active metabolites". *BoneKEy Reports* **3** (2014), 1–8.

[7] R. Menzel. *Photonics - Linear and Nonlinear Interactions of Laser Light and Matter*. 2nd ed. Berlin, Heidelberg: Springer Berlin Heidelberg, 2007.

[8] M. P. Marder. *Condensed Matter Physics*. 2nd ed. Hoboken, New Jersey: Jon Wiley & Sons, 2010.

[9] H. J. Kimble. "The quantum internet". *Nature* **453** (2008), 1023–1030. arXiv: 0806.4195.

[10] X.-S. Ma et al. "Quantum teleportation over 143 kilometres using active feed-forward". *Nature* **489** (2012), 269–273.

[11] P. B. Corkum and F. Krausz. "Attosecond science". *Nature Physics* **3** (2007), 381–387.

[12] K. E. Priebe et al. "Attosecond electron pulse trains and quantum state reconstruction in ultrafast transmission electron microscopy". *Nature Photonics* **11** (2017), 793–797.

[13] S. W. Hell. "Far-Field Optical Nanoscopy". *Science* **316** (2007), 1153–1158.

[14] L. Möckl, D. C. Lamb, and C. Bräuchle. "Super-resolved Fluorescence Microscopy: Nobel Prize in Chemistry 2014 for Eric Betzig, Stefan Hell, and William E. Moerner". *Angewandte Chemie International Edition* **53** (2014), 13972–13977.

[15] S. Han et al. "High-harmonic generation by field enhanced femtosecond pulses in metal-sapphire nanostructure". *Nature Communications* **7** (2016), 1–7.

[16] S. Ghimire and D. A. Reis. "High-harmonic generation from solids". *Nature Physics* **15** (2019), 10–16.

[17] M. I. Stockman. "Nanoplasmonics: past, present, and glimpse into future". *Optics Express* **19** (2011), 22029.

[18] V. Klimov. *Nanoplasmonics*. 1st ed. Singapore: Pan Stanford Publishing, 2014.

[19] J. Henzie et al. "Nanofabrication of Plasmonic Structures". *Annual Review of Physical Chemistry* **60** (2009), 147–165.

[20] S. Enoch and N. Bonod, eds. *Plasmonics - Fundamentals and Applications of Nanophotonics*. Vol. 167. Springer Series in Optical Sciences. Berlin, Heidelberg: Springer Berlin Heidelberg, 2012, 233–252.

[21] D. K. Gramotnev and S. I. Bozhevolnyi. "Plasmonics beyond the diffraction limit". *Nature Photonics* **4** (2010), 83–91.

[22] J. A. Schuller et al. "Plasmonics for extreme light concentration and manipulation." *Nature Materials* **9** (2010), 193–204.

[23] R. H. Ritchie. "Surface plasmons in solids". *Surface Science* **34** (1973), 1–19.

[24] H. Raether. *Surface Plasmons on Smooth and Rough Surfaces and on Gratings*. 1st ed. Berlin, Heidelberg, New York: Springer, 1988.

[25] W. L. Barnes, A. Dereux, and T. W. Ebbesen. "Surface plasmon subwavelength optics." *Nature* **424** (2003), 824–30.

[26] E. Ozbay. "Plasmonics: Merging Photonics and Electronics at Nanoscale Dimensions". *Science* **311** (2006), 189–193.

[27] R. Zia et al. "Plasmonics: the next chip-scale technology". *Materials Today* **9** (2006), 20–27.

[28] K. F. MacDonald et al. "Ultrafast active plasmonics". *Nature Photonics* **3** (2009), 55–58.

[29] B. Barwick and A. H. Zewail. "Photonics and Plasmonics in 4D Ultrafast Electron Microscopy". *ACS Photonics* **2** (2015), 1391–1402.

[30] M. Kauranen and A. V. Zayats. "Nonlinear plasmonics". *Nature Photonics* **6** (2012), 737–748.

[31] M. S. Tame et al. "Quantum plasmonics". *Nature Physics* **9** (2013), 329–340. arXiv: 1312.6806.

[32] J. Butet, P.-F. Brevet, and O. J. F. Martin. "Optical Second Harmonic Generation in Plasmonic Nanostructures: From Fundamental Principles to Advanced Applications". *ACS Nano* **9** (2015), 10545–10562.

[33] J. Flick, N. Rivera, and P. Narang. "Strong light-matter coupling in quantum chemistry and quantum photonics". *Nanophotonics* **7** (2018), 1479–1501.

[34] S. Kawata, Y. Inouye, and P. Verma. "Plasmonics for near-field nano-imaging and superlensing". *Nature Photonics* **3** (2009), 388–394.

[35] D. K. Gramotnev and S. I. Bozhevolnyi. "Nanofocusing of electromagnetic radiation". *Nature Photonics* **8** (2014), 13–22.

[36] A. Giugni et al. "Adiabatic nanofocusing: spectroscopy, transport and imaging investigation of the nano world". *Journal of Optics* **16** (2014), 114003.

[37] L. Novotny and N. van Hulst. "Antennas for light". *Nature Photonics* **5** (2011), 83–90.

[38] M. I. Stockman et al. "Roadmap on plasmonics". *Journal of Optics* **20** (2018), 043001.

[39] V. Kravtsov et al. "Plasmonic nanofocused four-wave mixing for femtosecond near-field imaging". *Nature Nanotechnology* (2016), 1–7.

[40] T. Jiang et al. "Ultrafast coherent nonlinear nanooptics and nanoimaging of graphene". *Nature Nanotechnology* **14** (2019), 838–843.

[41] S. Berweger et al. "Adiabatic Tip-Plasmon Focusing for Nano-Raman Spectroscopy". *The Journal of Physical Chemistry Letters* **1** (2010), 3427–3432.

[42] X. Ma et al. "Toward High-Contrast Atomic Force Microscopy-Tip-Enhanced Raman Spectroscopy Imaging: Nanoantenna-Mediated Remote-Excitation on Sharp-Tip Silver Nanowire Probes". *Nano Letters* **19** (2019), 100–107.

[43] F. Zenhausern, Y. Martin, and H. K. Wickramasinghe. "Scanning Interferometric Apertureless Microscopy: Optical Imaging at 10 Angstrom Resolution". *Science* **269** (1995), 1083–1085.

[44] A. Bek, R. Vogelgesang, and K. Kern. "Apertureless scanning near field optical microscope with sub-10 nm resolution". *Review of Scientific Instruments* **77** (2006), 043703.

[45] S. Schmidt et al. "Adiabatic nanofocusing on ultrasmooth single-crystalline gold tapers creates a 10-nm-sized light source with few-cycle time resolution." *ACS Nano* **6** (2012), 6040–8.

[46] M. Esmann et al. "Vectorial near-field coupling". *Nature Nanotechnology* **14** (2019).

[47] R. Zhang et al. "Chemical mapping of a single molecule by plasmon-enhanced Raman scattering". *Nature* **498** (2013), 82–86.

[48] J. Lee et al. "Visualizing vibrational normal modes of a single molecule with atomically confined light". *Nature* **568** (2019), 78–82.

[49] R. B. Jaculbia et al. "Single-molecule resonance Raman effect in a plasmonic nanocavity". *Nature Nanotechnology* **15** (2020), 105–110.

[50] J. Vogelsang et al. "Ultrafast Electron Emission from a Sharp Metal Nanotaper Driven by Adia-

batic Nanofocusing of Surface Plasmons". *Nano Letters* **15** (2015), 4685–4691.

[51] M. Müller et al. "Nanofocused Plasmon-Driven Sub-10 fs Electron Point Source". *ACS Photonics* **3** (2016), 611–619. arXiv: 1512.07037.

[52] J. Vogelsang et al. "Observing charge separation in nanoantennas via ultrafast point-projection electron microscopy". *Light: Science & Applications* **7** (2018), 55.

[53] A. Feist et al. "Nanoscale diffractive probing of strain dynamics in ultrafast transmission electron microscopy". *Structural Dynamics* **5** (2018), 014302.

[54] A. Feist et al. "Structural dynamics probed by high-coherence electron pulses". *MRS Bulletin* **43** (2018), 504–511.

[55] M. Gulde et al. "Ultrafast low-energy electron diffraction in transmission resolves polymer/graphene superstructure dynamics". *Science* **345** (2014), 200–204.

[56] S. Vogelgesang et al. "Phase ordering of charge density waves traced by ultrafast low-energy electron diffraction". *Nature Physics* **14** (2018), 184–190.

[57] W. Ho. "Single-molecule chemistry". *The Journal of Chemical Physics* **117** (2002), 11033–11061.

[58] K. Morgenstern, N. Lorente, and K.-H. Rieder. "Controlled manipulation of single atoms and small molecules using the scanning tunnelling microscope". *Physica Status Solidi B* **250** (2013), 1671–1751.

[59] D. P. Woodruff. *Modern Techniques of Surface Science*. 3rd. Cambridge University Press, 2016.

[60] S. Grafström. "Photoassisted scanning tunneling microscopy". *Journal of Applied Physics* **91** (2002), 1717.

[61] H. Shigekawa and S. Yoshida. "Laser-combined Scanning Tunneling Microscopy and Its Applications". *AAPPS Bulletin* **28** (2018), 9–18.

[62] Y. Tian et al. "Recent Advances in Ultrafast Time-Resolved Scanning Tunneling Microscopy". *Surface Review and Letters* **25** (2018), 1841003.

[63] V. A. Ukraintsev and J. T. Yates. "Nanosecond laser induced single atom deposition with nanometer spatial resolution using a STM". *Journal of Applied Physics* **80** (1996), 2561–2571.

[64] A. Dolocan et al. "Two-Color Ultrafast Photoexcited Scanning Tunneling Microscopy". *The Journal of Physical Chemistry C* **115** (2011), 10033–10043.

[65] B. Schröder et al. "Real-space imaging of nanotip plasmons using electron energy loss spectroscopy". *Physical Review B* **92** (2015), 085411.

[66] S. V. Yalunin, B. Schröder, and C. Ropers. "Theory of electron energy loss near plasmonic wires, nanorods, and cones". *Physical Review B* **93** (2016), 115408.

[67] B. Schröder et al. "An ultrafast nanotip electron gun triggered by grating-coupled surface plasmons". *Applied Physics Letters* **107** (2015), 231105.

[68] B. Schröder et al. "Controlling photocurrent channels in scanning tunneling microscopy". *New Journal of Physics* **22** (2020), 033047.

[69] M. Fox. *Optical Properties of Solids*. 2nd ed. New York: Oxford University Press, 2010.

[70] J. Weiner and F. Nunes. *Light-Matter Interaction*. Oxford University Press, 2017, 1–12.

[71] U. Kreibig and M. Vollmer. *Optical Properties of Metal Clusters*. 1st ed. Berlin, Heidelberg, New York: Springer, 1995.

[72] L. Novotny and B. Hecht. *Principles of Nano-Optics*. 1st ed. Cambridge: Cambridge University Press, 2006.

[73] S. A. Maier. *Plasmonics: Fundamentals and Applications*. 1st ed. New York: Springer, 2007.

[74] F. J. García de Abajo. "Optical excitations in electron microscopy". *Reviews of Modern Physics* **82** (2010), 209–275. arXiv: 0903.1669.

[75] A. Sommerfeld. "Zur Elektronentheorie der Metalle auf Grund der Fermischen Statistik". *Zeitschrift für Physik* **47** (1928), 1–32.

[76] A. V. Zayats and I. I. Smolyaninov. "Near-field photonics: surface plasmon polaritons and localized surface plasmons". *Journal of Optics A: Pure and Applied Optics* **5** (2003), S16–S50.

[77] A. Trügler and U. Hohenester. "Strong coupling between a metallic nanoparticle and a single molecule". *Physical Review B* **77** (2008), 115403.

[78] A. Archambault et al. "Quantum theory of spontaneous and stimulated emission of surface plasmons". *Physical Review B* **82** (2010), 035411. arXiv: 1004.0135.

[79] E. Hutter and J. H. Fendler. "Exploitation of localized surface plasmon resonance". *Advanced Materials* **16** (2004), 1685–1706.

[80] T. V. Shahbazyan and M. I. Stockman, eds. *Plasmonics: Theory and Applications*. Vol. 15. Challenges and Advances in Computational Chemistry and Physics. Dordrecht: Springer, 2013.

[81] V. Amendola et al. "Surface plasmon resonance in gold nanoparticles: a review". *Journal of Physics: Condensed Matter* **29** (2017), 203002.

[82] P. B. Johnson and R. W. Christy. "Optical Constants of the Noble Metals". *Physical Review B* **6** (1972), 4370–4379.

[83] P. West et al. "Searching for better plasmonic materials". *Laser & Photonics Reviews* **4** (2010), 795–808. arXiv: 0911.2737.

[84] J. D. Jackson. *Klassische Elektrodynamik*. 3. Auflage. Berlin: De Gruyter, 2001.

[85] C. C. Neacsu, G. A. Steudle, and M. B. Raschke. "Plasmonic light scattering from nanoscopic metal tips". *Applied Physics B* **80** (2005), 295–300.

[86] C. F. Bohren and D. R. Huffman. *Absorption and scattering of light by small particles*. 1st ed. New York, Chichester, u.a.: John Wiley & Sons, 1983.

[87] Y. C. Martin, H. F. Hamann, and H. K. Wickramasinghe. "Strength of the electric field in apertureless near-field optical microscopy". *Journal of Applied Physics* **89** (2001), 5774–5778.

[88] G. Mie. "Beiträge zur Optik trüber Medien, speziell kolloidaler Metallösungen". *Annalen der Physik* **330** (1908), 377–445.

[89] W. Denk and D. W. Pohl. "Near-field optics: Microscopy with nanometer-size fields". *Journal of Vacuum Science & Technology B: Microelectronics and Nanometer Structures* **9** (1991), 510.

[90] O. J. F. Martin and C. Girard. "Controlling and tuning strong optical field gradients at a local probe microscope tip apex". *Applied Physics Letters* **70** (1997), 705.

[91] L. Novotny, R. Bian, and X. Xie. "Theory of Nanometric Optical Tweezers". *Physical Review Letters* **79** (1997), 645–648.

[92] Y. Kawata, C. Xu, and W. Denk. "Feasibility of molecular-resolution fluorescence near-field microscopy using multi-photon absorption and field enhancement near a sharp tip". *Journal of Applied Physics* **85** (1999), 1294.

[93] A. V. Goncharenko, J. K. Wang, and Y. C. Chang. "Electric near-field enhancement of a sharp semi-infinite conical probe: Material and cone angle dependence". *Physical Review B - Condensed Matter and Materials Physics* **74** (2006), 1–9.

[94] A. V. Goncharenko et al. "Electric field enhancement by a nanometer-scaled conical metal tip in the context of scattering-type near-field optical microscopy". *Applied Physics Letters* **88** (2006), 104101.

[95] A. V. Goncharenko, H. Chang, and J.-K. Wang. "Electric near-field enhancing properties of a finite-size metal conical nano-tip." *Ultramicroscopy* **107** (2007), 151–7.

[96] N. Behr and M. B. Raschke. "Optical Antenna Properties of Scanning Probe Tips: Plasmonic Light Scattering, Tip-Sample Coupling, and Near-Field Enhancement". *The Journal of Physical Chemistry C* **112** (2008), 3766–3773.

[97] W. Zhang, X. Cui, and O. J. F. Martin. "Local field enhancement of an infinite conical metal tip illuminated by a focused beam". *Journal of Raman Spectroscopy* **40** (2009), 1338–1342.

[98] A. Arbouet et al. "Interaction of an ultrashort optical pulse with a metallic nanotip: A Green dyadic approach". *Journal of Applied Physics* **112** (2012), 053103.

[99] A. Pors, K. V. Nerkararyan, and S. I. Bozhevolnyi. "Scaling in light scattering by sharp conical metal tips". *Optics Letters* **39** (2014), 3308.

[100] S. Thomas et al. "Large optical field enhancement for nanotips with large opening angles". *New Journal of Physics* **17** (2015), 063010.

[101] A. B. Petrin. "Focusing of light at the nanoapex of a metal microtip located above the plane of a dielectric or metal". *Quantum Electronics* **46** (2016), 848–854.

[102] A. Bouhelier. "Field-enhanced scanning near-field optical microscopy." *Microscopy Research and Technique* **69** (2006), 563–79.

[103] C. Neacsu, G. Reider, and M. B. Raschke. "Second-harmonic generation from nanoscopic metal tips: Symmetry selection rules for single asymmetric nanostructures". *Physical Review B* **71** (2005), 201402.

[104] C. Ropers et al. "Localized Multiphoton Emission of Femtosecond Electron Pulses from Metal Nanotips". *Physical Review Letters* **98** (2007), 043907.

[105] R. Bormann et al. "Tip-Enhanced Strong-Field Photoemission". *Physical Review Letters* **105** (2010), 147601.

[106] D. J. Park et al. "Strong Field Acceleration and Steering of Ultrafast Electron Pulses from a Sharp Metallic Nanotip". *Physical Review Letters* **109** (2012), 244803.

[107] E. Kretschmann and H. Raether. "Notizen: Radiative Decay of Non Radiative Surface Plasmons Excited by Light". *Zeitschrift für Naturforschung A* **23** (1968), 2135–2136.

[108] A. Otto. "Excitation of nonradiative surface plasma waves in silver by the method of frustrated total reflection". *Zeitschrift für Physik A Hadrons and nuclei* **216** (1968), 398–410.

[109] T. Wang et al. "Excitation of propagating surface plasmons with a scanning tunnelling microscope". *Nanotechnology* **22** (2011).

[110] M. Esmann et al. "K-Space Imaging of the Eigenmodes of Sharp Gold Tapers for Scanning Near-Field Optical Microscopy." *Beilstein journal of nanotechnology* **4** (2013), 603–10.

[111] C. Genet and T. W. Ebbesen. "Light in tiny holes". *Nature* **445** (2007), 39–46.

[112] C. Ropers. "Femtosecond Excitations in Metallic Nanostructures". Dissertation. Humboldt-Universität Berlin, 2007.

[113] J. Nelayah et al. "Mapping surface plasmons on a single metallic nanoparticle". *Nature Physics* **3** (2007), 348–353.

[114] J. A. Scholl, A. L. Koh, and J. A. Dionne. "Quantum plasmon resonances of individual metallic nanoparticles". *Nature* **483** (2012), 421–427.

[115] O. Nicoletti et al. "Three-dimensional imaging of localized surface plasmon resonances of metal nanoparticles." *Nature* **502** (2013), 80–4.

[116] O. L. Krivanek et al. "Vibrational spectroscopy in the electron microscope". *Nature* **514** (2014), 209–212.

[117] A. Polman, M. Kociak, and F. J. García de Abajo. "Electron-beam spectroscopy for nanophotonics". *Nature Materials* **18** (2019), 1158–1171.

[118] J. Schefold et al. "Spatial Resolution of Coherent Cathodoluminescence Super-Resolution Microscopy". *ACS Photonics* **6** (2019), 1067–1072.

[119] R. H. Ritchie. "Plasma Losses by Fast Electrons in Thin Films". *Physical Review* **106** (1957), 874–881.

[120] C. J. Powell and J. B. Swan. "Origin of the Characteristic Electron Energy Losses in Aluminum". *Physical Review* **115** (1959), 869–875.

[121] E. A. Stern and R. A. Ferrell. "Surface plasma oscillations of a degenerate electron gas". *Physical Review* **120** (1960), 130–136.

[122] C. Colliex, M. Kociak, and O. Stéphan. "Electron Energy Loss Spectroscopy imaging of surface plasmons at the nanometer scale". *Ultramicroscopy* **162** (2016), A1–A24.

[123] S. T. Park, M. Lin, and A. H. Zewail. "Photon-induced near-field electron microscopy (PINEM): Theoretical and experimental". *New Journal of Physics* **12** (2010), 123028.

[124] B. J. M. Brenny, A. Polman, and F. J. García de Abajo. "Femtosecond plasmon and photon wave packets excited by a high-energy electron on a metal or dielectric surface". *Physical Review B* **94** (2016), 155412.

[125] R. Ritchie et al. "Surface-Plasmon Resonance Effect in Grating Diffraction". *Physical Review Letters* **21** (1968), 1530–1533.

[126] D. Heitmann. "Radiative decay of surface plasmons excited by fast electrons on periodically modulated silver surfaces". *Journal of Physics C: Solid State Physics* **10** (1977), 397–405.

[127] H. F. Ghaemi et al. "Surface plasmons enhance optical transmission through subwavelength holes". *Physical Review B* **58** (1998), 6779–6782.

[128] C. Ropers et al. "Grating-coupling of surface plasmons onto metallic tips: a nanoconfined light source." *Nano Letters* **7** (2007), 2784–8.

[129] S. Berweger et al. "Femtosecond nanofocusing with full optical waveform control." *Nano Letters* **11** (2011), 4309–13.

[130] E. J. Heilweil and R. M. Hochstrasser. "Nonlinear spectroscopy and picosecond transient grating study of colloidal gold". *The Journal of Chemical Physics* **82** (1985), 4762–4770.

[131] S. Link and M. A. El-Sayed. "Optical Properties and Ultrafast Dynamics of Metallic Nanocrystals". *Annual Review of Physical Chemistry* **54** (2003), 331–366.

[132] J. B. Khurgin. "How to deal with the loss in plasmonics and metamaterials". *Nature Nanotechnology* **10** (2015), 2–6.

[133] M. L. Brongersma, N. J. Halas, and P. Nordlander. "Plasmon-induced hot carrier science and technology". *Nature Nanotechnology* **10** (2015), 25–34.

[134] A. M. Brown et al. "Nonradiative Plasmon Decay and Hot Carrier Dynamics: Effects of Phonons, Surfaces, and Geometry". *ACS Nano* **10** (2016), 957–966.

[135] S. Anisimov, B. Kapeliovich, and T. Perel'man. "Electron emission from metal surfaces exposed to ultrashort laser pulses". *Journal of Experimental and Theoretical Physics* **66** (1974), 375–377.

[136] G. Herink, L. Wimmer, and C. Ropers. "Field emission at terahertz frequencies: AC-tunneling and ultrafast carrier dynamics". *New Journal of Physics* **16** (2014), 123005.

[137] N. A. Mortensen et al. "A generalized non-local optical response theory for plasmonic nanostructures". *Nature Communications* **5** (2014), 3809. arXiv: 1312.7190.

[138] W. Zhu et al. "Quantum mechanical effects in plasmonic structures with subnanometre gaps". *Nature Communications* **7** (2016), 11495.

[139] C. Sönnichsen et al. "Drastic Reduction of Plasmon Damping in Gold Nanorods". *Physical Review Letters* **88** (2002), 077402.

[140] A. Anderson et al. "Few-Femtosecond Plasmon Dephasing of a Single Metallic Nanostructure from Optical Response Function Reconstruction by Interferometric Frequency Resolved Optical Gating". *Nano Letters* **10** (2010), 2519–2524.

[141] T. Rohwer et al. "Collapse of long-range charge order tracked by time-resolved photoemission at high momenta". *Nature* **471** (2011), 490–494.

[142] S. Mathias et al. "Self-amplified photo-induced gap quenching in a correlated electron material". *Nature Communications* **7** (2016), 12902.

[143] O. Schmidt et al. "Time-resolved two photon photoemission electron microscopy". *Ap-*

plied Physics B: Lasers and Optics **74** (2002), 223–227.

[144] B. Frank et al. "Short-range surface plasmonics: Localized electron emission dynamics from a 60-nm spot on an atomically flat single-crystalline gold surface". *Science Advances* **3** (2017), e1700721.

[145] D. Podbiel et al. "Imaging the Nonlinear Plasmoemission Dynamics of Electrons from Strong Plasmonic Fields". *Nano Letters* **17** (2017), 6569–6574.

[146] A. Feist et al. "Quantum coherent optical phase modulation in an ultrafast transmission electron microscope". *Nature* **521** (2015), 200–203.

[147] A. Feist et al. "Ultrafast transmission electron microscopy using a laser-driven field emitter: Femtosecond resolution with a high coherence electron beam". *Ultramicroscopy* **176** (2017), 63–73.

[148] G. Storeck et al. "Nanotip-based photoelectron microgun for ultrafast LEED". *Structural Dynamics* **4** (2017), 044024.

[149] S. I. Anisimov, V. A. Benderskiĭ, and G. Farkas. "Nonlinear photoelectric emission from metals induced by a laser radiation". *Soviet Physics Uspekhi* **20** (1977), 467–488.

[150] H. Petek and S. Ogawa. "Femtosecond time-resolved two-photon photoemission studies of electron dynamics in metals". *Progress in Surface Science* **56** (1997), 239–310.

[151] S. E. Irvine, A. Dechant, and A. Y. Elezzabi. "Generation of 0.4-keV femtosecond electron pulses using impulsively excited surface plasmons". *Physical Review Letters* **93** (2004), 1–4.

[152] F. Bisio et al. "Mechanisms of High-Order Perturbative Photoemission from Cu(001)". *Physical Review Letters* **96** (2006), 087601.

[153] M. Bauer, A. Marienfeld, and M. Aeschlimann. "Hot electron lifetimes in metals probed by time-resolved two-photon photoemission". *Progress in Surface Science* **90** (2015), 319–376.

[154] W. Kaiser and C. G. Garrett. "Two-photon excitation in CaF2: Eu2+". *Physical Review Letters* **7** (1961), 229–231.

[155] T. Brabec and F. Krausz. "Intense few-cycle laser fields: Frontiers of nonlinear optics". *Reviews of Modern Physics* **72** (2000), 545–591.

[156] D. Williams and C. Carter. *The Transmission Electron Microscope*. 2nd ed. New York: Springer, 2009.

[157] R. H. Fowler. "The Analysis of Photoelectric Sensitivity Curves for Clean Metals at Various Temperatures". *Physical Review* **38** (1931), 45–56.

[158] L. A. DuBridge. "Theory of the Energy Distribution of Photoelectrons". *Physical Review* **43** (1933), 727–741.

[159] J. Bechtel, W. Lee Smith, and N. Bloembergen. "Two-photon photoemission from metals induced by picosecond laser pulses". *Physical Review B* **15** (1977), 4557–4563.

[160] R. Yen, J. Liu, and N. Bloembergen. "Thermally assisted multiphoton photoelectric emission from tungsten". *Optics Communications* **35** (1980), 277–282.

[161] J. P. Girardeau-Montaut and C. Girardeau-Montaut. "Theory of ultrashort nonlinear multiphoton photoelectric emission from metals". *Physical Review B* **51** (1995), 13560–13567.

[162] G. Ferrini et al. "Non-linear electron photoemission from metals with ultrashort pulses". *Nuclear Instruments and Methods in Physics Research Section A: Accelerators, Spectrometers, Detectors and Associated Equipment* **601** (2009), 123–131.

[163] B. Barwick et al. "Laser-induced ultrafast electron emission from a field emission tip". *New Journal of Physics* **9** (2007), 142–142.

[164] M. Krüger et al. "Attosecond physics in photoemission from a metal nanotip". *Journal of Physics B: Atomic, Molecular and Optical Physics* **45** (2012), 074006.

[165] P. Hommelhoff et al. "Field Emission Tip as a Nanometer Source of Free Electron Femtosec-

ond Pulses". *Physical Review Letters* **96** (2006), 077401.

[166] P. Hommelhoff, C. Kealhofer, and M. A. Kasevich. "Ultrafast Electron Pulses from a Tungsten Tip Triggered by Low-Power Femtosecond Laser Pulses". *Physical Review Letters* **97** (2006), 247402.

[167] C. Ropers et al. "Ultrafast optical excitations of metallic nanostructures: from light confinement to a novel electron source". *New Journal of Physics* **9** (2007), 397–397.

[168] M. Schenk, M. Krüger, and P. Hommelhoff. "Strong-Field Above-Threshold Photoemission from Sharp Metal Tips". *Physical Review Letters* **105** (2010), 257601.

[169] H. Yanagisawa et al. "Laser-induced field emission from a tungsten tip: Optical control of emission sites and the emission process". *Physical Review B* **81** (2010), 115429. arXiv: 1001.5375.

[170] M. Krüger, M. Schenk, and P. Hommelhoff. "Attosecond control of electrons emitted from a nanoscale metal tip." *Nature* **475** (2011), 78–81.

[171] H. Yanagisawa et al. "Energy Distribution Curves of Ultrafast Laser-Induced Field Emission and Their Implications for Electron Dynamics". *Physical Review Letters* **107** (2011), 087601. arXiv: 1103.4310.

[172] G. Herink et al. "Field-driven photoemission from nanostructures quenches the quiver motion". *Nature* **483** (2012), 190–193.

[173] M. Lisowski et al. "Ultra-fast dynamics of electron thermalization, cooling and transport effects in Ru(001)". *Applied Physics A: Materials Science and Processing* **78** (2004), 165–176.

[174] B. Y. Mueller and B. Rethfeld. "Relaxation dynamics in laser-excited metals under nonequilibrium conditions". *Physical Review B* **87** (2013), 035139.

[175] L. Wu and L. K. Ang. "Nonequilibrium model of ultrafast laser-induced electron photofield emission from a dc-biased metallic surface". *Physical Review B - Condensed Matter and Materials Physics* **78** (2008), 1–7.

[176] R. H. Fowler and L. Nordheim. "Electron Emission in Intense Electric Fields". *Proceeding of the Royal Society A* **119** (1928).

[177] L. Wimmer et al. "Terahertz control of nanotip photoemission". *Nature Physics* **10** (2014), 432–436.

[178] B. Piglosiewicz et al. "Carrier-envelope phase effects on the strong-field photoemission of electrons from metallic nanostructures". *Nature Photonics* **8** (2014), 37–42.

[179] M. R. Bionta et al. "Wavelength and shape dependent strong-field photoemission from silver nanotips". *New Journal of Physics* **18** (2016), 103010.

[180] L. Wimmer et al. "Clocking plasmon nanofocusing by THz near-field streaking". *Applied Physics Letters* **111** (2017), 131102.

[181] L. V. Keldysh. "Ionization in the Field of a Strong Electromagnetic Wave". *Soviet Physics JETP* **20** (1965), 1307.

[182] M. Garg and K. Kern. "Attosecond coherent manipulation of electrons in tunneling microscopy". *Science* **367** (2020), 411–415.

[183] C. C. Neacsu, S. Berweger, and M. B. Raschke. "Tip-Enhanced Raman Imaging and Nanospectroscopy: Sensitivity, Symmetry, and Selection Rules". *NanoBiotechnology* **3** (2009), 172–196.

[184] B. Ren, G. Picardi, and B. Pettinger. "Preparation of gold tips suitable for tip-enhanced Raman spectroscopy and light emission by electrochemical etching". *Review of Scientific Instruments* **75** (2004), 837.

[185] J. J. Lingane. "Standard potentials of half-reactions involving + 1 and + 3 gold in chloride medium". *Journal of Electroanalytical Chemistry* **4** (1962), 332–342.

[186] V. S. Volkov et al. "Nanofocusing with Channel Plasmon Polaritons". *Nano Letters* **9** (2009), 1278–1282.

[187] M. Schnell et al. "Nanofocusing of mid-infrared energy with tapered transmission lines". *Nature Photonics* **5** (2011), 283–287.

[188] S. Berweger et al. "Light on the Tip of a Needle: Plasmonic Nanofocusing for Spectroscopy on the Nanoscale". *The Journal of Physical Chemistry Letters* **3** (2012), 945–952.

[189] P. Groß et al. "Plasmonic nanofocusing – grey holes for light". *Advances in Physics: X* **6149** (2016), 1–34.

[190] A. J. Babadjanyan, N. L. Margaryan, and K. Nerkararyan. "Superfocusing of surface polaritons in the conical structure". *Journal of Applied Physics* **87** (2000), 3785.

[191] M. Stockman. "Nanofocusing of Optical Energy in Tapered Plasmonic Waveguides". *Physical Review Letters* **93** (2004), 137404.

[192] N. A. Issa and R. Guckenberger. "Optical Nanofocusing on Tapered Metallic Waveguides". *Plasmonics* **2** (2007), 31–37.

[193] M. W. Vogel and D. K. Gramotnev. "Adiabatic nano-focusing of plasmons by metallic tapered rods in the presence of dissipation". *Physics Letters A* **363** (2007), 507–511.

[194] K. Kurihara et al. "Superfocusing modes of surface plasmon polaritons in conical geometry based on the quasi-separation of variables approach". *Journal of Physics A: Mathematical and Theoretical* **40** (2007), 12479–12503.

[195] M. W. Vogel and D. K. Gramotnev. "Shape effects in tapered metal rods during adiabatic nanofocusing of plasmons". *Journal of Applied Physics* **107** (2010), 044303.

[196] R. P. Zaccaria et al. "Surface plasmon polariton compression through radially and linearly polarized source". *Optics Letters* **37** (2012), 545.

[197] A. B. Petrin. "Regularities of nanofocusing of a surface plasmon wave near the nanoapex of a metallic microtip". *High Temperature* **54** (2016), 475–482.

[198] R. Ruppin. "Effect of non-locality on nanofocusing of surface plasmon field intensity in a conical tip". *Physics Letters, Section A: General, Atomic and Solid State Physics* **340** (2005), 299–302.

[199] A. Wiener et al. "Nonlocal effects in the nanofocusing performance of plasmonic tips." *Nano Letters* **12** (2012), 3308–14.

[200] D. K. Gramotnev, M. W. Vogel, and M. I. Stockman. "Optimized nonadiabatic nanofocusing of plasmons by tapered metal rods". *Journal of Applied Physics* **104** (2008), 034311.

[201] B. Ahn et al. "Optimization of a nanotip on a surface for the ultrafast probing of propagating surface plasmons". *Optics Express* **24** (2016), 92.

[202] E. S. Manuilovich, V. A. Astapenko, and P. A. Golovinskii. "Superfocusing of an ultrashort plasmon pulse by a conducting cone". *Quantum Electronics* **46** (2016), 50–56.

[203] C. C. Neacsu et al. "Near-field localization in plasmonic superfocusing: a nanoemitter on a tip." *Nano Letters* **10** (2010), 592–6.

[204] D. Sadiq et al. "Adiabatic nanofocusing scattering-type optical nanoscopy of individual gold nanoparticles." *Nano Letters* **11** (2011), 1609–13.

[205] T. Umakoshi, Y. Saito, and P. Verma. "Highly efficient plasmonic tip design for plasmon nanofocusing in near-field optical microscopy". *Nanoscale* (2016).

[206] S. F. Becker et al. "Gap-Plasmon-Enhanced Nanofocusing Near-Field Microscopy". *ACS Photonics* **3** (2016), 223–232.

[207] M. Esmann et al. "Plasmonic nanofocusing spectral interferometry". *Nanophotonics* **9** (2020), 491–508.

[208] F. De Angelis et al. "Nanoscale chemical mapping using three-dimensional adiabatic compression of surface plasmon polaritons." *Nature Nanotechnology* **5** (2010), 67–72.

[209] K. Tomita, Y. Kojima, and F. Kannari. "Selective Coherent Anti-Stokes Raman Scattering Microscopy Employing Dual-Wavelength Nanofocused Ultrafast Plasmon Pulses". *Nano Letters* **18** (2018), 1366–1372.

[210] J. Vogelsang et al. "Plasmonic-Nanofocusing-Based Electron Holography". *ACS Photonics* **5** (2018), 3584–3593.

[211] M. Stockman. "Erratum: Nanofocusing of Optical Energy in Tapered Plasmonic Waveguides [Phys. Rev. Lett. 93, 137404 (2004)]". *Physical Review Letters* **106** (2011), 019901.

[212] C. Pfeiffer, E. Economou, and K. Ngai. "Surface polaritons in a circularly cylindrical interface: Surface plasmons". *Physical Review B* **10** (1974), 3038–3051.

[213] U. Schröter and A. Dereux. "Surface plasmon polaritons on metal cylinders with dielectric core". *Physical Review B* **64** (2001), 125420.

[214] F. Lu et al. "Mode evolution and nanofocusing of grating-coupled surface plasmon polaritons on metallic tip". *Opto-Electronic Advances* **1** (2018), 18001001–18001007.

[215] L. Novotny and C. Hafner. "Light propagation in a cylindrical waveguide with a complex, metallic, dielectric function". *Physical Review E* **50** (1994), 4094–4106.

[216] J. Takahara et al. "Guiding of a one-dimensional optical beam with nanometer diameter". *Optics Letters* **22** (1997), 475.

[217] S. Guo et al. "Far-Field Radiation of Three-Dimensional Plasmonic Gold Tapers near Apexes". *ACS Photonics* **6** (2019), 2509–2516.

[218] N. Talebi et al. "Excitation of Mesoscopic Plasmonic Tapers by Relativistic Electrons: Phase Matching versus Eigenmode Resonances". *ACS Nano* **9** (2015), 7641–7648.

[219] S. Guo et al. "Reflection and Phase Matching in Plasmonic Gold Tapers". *Nano Letters* **16** (2016), 6137–6144.

[220] M. W. Vogel. "Optimization of plasmon nanofocusing in tapered metal rods". *Journal of Nanophotonics* **2** (2008), 021852.

[221] F. von Cube. "Near Field Characterization of Plasmonic Nanostructures with Electron Energy Loss Spectroscopy". Dissertation. Rheinische Friedrich-Wilhelms-Universität Bonn, 2014.

[222] A. Hartschuh et al. "High-resolution near-field Raman microscopy of single-walled carbon nanotubes." *Physical Review Letters* **90** (2003), 095503.

[223] F. Keilmann and R. Hillenbrand. "Near-field microscopy by elastic light scattering from a tip." *Philosophical transactions. Series A, Mathematical, physical, and engineering sciences* **362** (2004), 787–805.

[224] V. Kravtsov, J. M. Atkin, and M. B. Raschke. "Group delay and dispersion in adiabatic plasmonic nanofocusing." *Optics Letters* **38** (2013), 1322–4.

[225] E. J. R. Vesseur et al. "Direct observation of plasmonic modes in Au nanowires using high-resolution cathodoluminescence spectroscopy". *Nano Letters* **7** (2007), 2843–2846.

[226] M. Kuttge et al. "Local density of states, spectrum, and far-field interference of surface plasmon polaritons probed by cathodoluminescence". *Physical Review B - Condensed Matter and Materials Physics* **79** (2009), 2–5.

[227] P. Chaturvedi et al. "Imaging of plasmonic modes of silver nanoparticles using high-resolution cathodoluminescence spectroscopy". *ACS Nano* **3** (2009), 2965–2974. arXiv: 0906.1077.

[228] M. Bosman et al. "Mapping surface plasmons at the nanometre scale with an electron beam". *Nanotechnology* **18** (2007), 165505.

[229] G. Boudarham et al. "Spectral Imaging of Individual Split-Ring Resonators". *Physical Review Letters* **105** (2010), 255501.

[230] F. von Cube et al. "Spatio-spectral characterization of photonic meta-atoms with electron energy-loss spectroscopy [Invited]". *Optical Materials Express* **1** (2011), 1009.

[231] D. Rossouw et al. "Multipolar plasmonic resonances in silver nanowire antennas imaged with a subnanometer electron probe." *Nano Letters* **11** (2011), 1499–504.

[232] F. Huth et al. "Resonant antenna probes for tip-enhanced infrared near-field microscopy." *Nano Letters* **13** (2013), 1065–72.

[233] D. T. Schoen et al. "Probing Complex Reflection Coefficients in One-Dimensional Surface Plasmon Polariton Waveguides and Cavities Using STEM EELS". *Nano Letters* **15** (2015), 120–126.

[234] B. Barwick, D. J. Flannigan, and A. H. Zewail. "Photon-induced near-field electron microscopy." *Nature* **462** (2009), 902–906.

[235] F. J. García de Abajo and M. Kociak. "Probing the Photonic Local Density of States with Electron Energy Loss Spectroscopy". *Physical Review Letters* **100** (2008), 106804.

[236] K. Busch, M. König, and J. Niegemann. "Discontinuous Galerkin methods in nanophotonics". *Laser & Photonics Reviews* **5** (2011), 773–809.

[237] C. Matyssek et al. "Computing electron energy loss spectra with the Discontinuous Galerkin Time-Domain method". *Photonics and Nanostructures - Fundamentals and Applications* **9** (2011), 367–373.

[238] J. K. Hyun et al. "Relativistic electron energy loss spectroscopy of solid and core-shell nanowires". *Physical Review B* **81** (2010), 165403.

[239] T. Walther et al. "First experimental test of a new monochromated and aberration-corrected 200kV field-emission scanning transmission electron microscope". *Ultramicroscopy* **106** (2006), 963–969.

[240] A. Taflove and S. C. Hagness. *Computational Electrodynamics: The Finite-Difference Time-Domain Method*. 3rd ed. London: Artech House, 2005.

[241] M. Abramowitz and I. Stegun. *Handbook of Mathematical Functions with Formulas, Graphs, and Mathematical Tables*. New York: Dover Publications, 1972.

[242] B. J. Siwick et al. "An Atomic-Level View of Melting Using Femtosecond Electron Diffraction". *Science* **302** (2003), 1382–1385.

[243] A. H. Zewail. "4D Ultrafast Electron Diffraction, Crystallography, and Microscopy". *Annual Review of Physical Chemistry* **57** (2006), 65–103.

[244] B. Barwick et al. "4D Imaging of Transient Structures and Morphologies in Ultrafast Electron Microscopy". *Science* **322** (2008), 1227–1231.

[245] A. H. Zewail. "Four-Dimensional Electron Microscopy". *Science* **328** (2010), 187–193.

[246] G. Sciaini and R. J. D. Miller. "Femtosecond electron diffraction: heralding the era of atomically resolved dynamics". *Reports on Progress in Physics* **74** (2011), 096101.

[247] E. Quinonez, J. Handali, and B. Barwick. "Femtosecond photoelectron point projection microscope". *Review of Scientific Instruments* **84** (2013).

[248] S. Lahme et al. "Femtosecond single-electron diffraction". *Structural Dynamics* **1** (2014), 034303.

[249] M. Müller, A. Paarmann, and R. Ernstorfer. "Femtosecond electrons probing currents and atomic structure in nanomaterials". *Nature Communications* **5** (2014), 5292. arXiv: 1405.4992.

[250] Y. Morimoto and P. Baum. "Diffraction and microscopy with attosecond electron pulse trains". *Nature Physics* **14** (2018), 252–256.

[251] R. Bormann. "Development and characterization of an electron gun for ultrafast electron microscopy Dissertation". Dissertation. Georg-August-Universität Göttingen, 2015.

[252] R. Bormann et al. "An ultrafast electron microscope gun driven by two-photon photoemission from a nanotip cathode". *Journal of Applied Physics* **118** (2015), 173105.

[253] H. Yanagisawa et al. "Optical Control of Field-Emission Sites by Femtosecond Laser Pulses". *Physical Review Letters* **103** (2009), 257603. arXiv: 0908.3464.

[254] A. R. Bainbridge and W. A. Bryan. "Velocity map imaging of femtosecond laser induced photoelectron emission from metal nanotips". *New Journal of Physics* **16** (2014), 103031.

[255] R. J. D. Miller. "Mapping Atomic Motions with Ultrabright Electrons: The Chemists' Gedanken Experiment Enters the Lab Frame". *Annual Review of Physical Chemistry* **65** (2014), 583–604.

[256] D. J. Flannigan and A. H. Zewail. "4D Electron Microscopy: Principles and Applications". *Accounts of Chemical Research* **45** (2012), 1828–1839.

[257] J. S. Kim et al. "Imaging of Transient Structures Using Nanosecond in Situ TEM". *Science* **321** (2008), 1472–1475.

[258] A. Hanisch-Blicharski et al. "Ultra-fast electron diffraction at surfaces: From nanoscale heat transport to driven phase transitions". *Ultramicroscopy* **127** (2013), 2–8.

[259] M. Eichberger et al. "Snapshots of cooperative atomic motions in the optical suppression of charge density waves." *Nature* **468** (2010), 799–802.

[260] L. Piazza et al. "Design and implementation of a fs-resolved transmission electron microscope based on thermionic gun technology". *Chemical Physics* **423** (2013), 79–84.

[261] V. R. Morrison et al. "A photoinduced metal-like phase of monoclinic VO2 revealed by ultrafast electron diffraction". *Science* **346** (2014), 445–448.

[262] C. Gerbig et al. "Spatio-temporal resolution studies on a highly compact ultrafast electron diffractometer". *New Journal of Physics* **17** (2015), 043050.

[263] A. Paarmann et al. "Coherent femtosecond low-energy single-electron pulses for time-resolved diffraction and imaging: A numerical study". *Journal of Applied Physics* **112** (2012), 113109.

[264] J. Hoffrogge et al. "Tip-based source of femtosecond electron pulses at 30 keV". *Journal of Applied Physics* **115** (2014), 094506. arXiv: 1303.2383v1.

[265] E. Quinonez, J. Handali, and B. Barwick. "Femtosecond photoelectron point projection microscope". *Review of Scientific Instruments* **84** (2013), 103710.

[266] S. Schmidt et al. "Wave front adaptation using a deformable mirror for adiabatic nanofocusing along an ultrasharp gold taper". *Optics Express* **21** (2013), 26564.

[267] B. Voigtländer. *Scanning Probe Microscopy*. NanoScience and Technology. Berlin, Heidelberg: Springer, 2015.

[268] W. Pfeiffer et al. "Photoelectron emission in femtosecond laser assisted scanning tunneling microscopy". *Applied Physics B: Lasers and Optics* **64** (1997), 265–268.

[269] T. L. Cocker et al. "Tracking the ultrafast motion of a single molecule by femtosecond orbital imaging". *Nature* **539** (2016), 263–267.

[270] P. Kloth and M. Wenderoth. "From time-resolved atomic-scale imaging of individual donors to their cooperative dynamics". *Science Advances* **3** (2017), e1601552.

[271] B. Knoll and F. Keilmann. "Near-field probing of vibrational absorption for chemical microscopy". *Nature* **399** (1999), 7–10.

[272] R. Hillenbrand, T. Taubner, and F. Keilmann. "Phonon-enhanced light matter interaction at the nanometre scale." *Nature* **418** (2002), 159–162.

[273] J. J. Baumberg et al. "Extreme nanophotonics from ultrathin metallic gaps". *Nature Materials* **18** (2019), 668–678.

[274] K. Minn, B. Birmingham, and Z. Zhang. "New development of nanoscale spectroscopy using scanning probe microscope". *Journal of Vacuum Science & Technology A* **38** (2020), 030801.

[275] E. Kazuma et al. "STM studies of photochemistry and plasmon chemistry on metal surfaces". *Progress in Surface Science* **93** (2018), 163–176.

[276] C. Lumdee, B. Yun, and P. G. Kik. "Gap-Plasmon Enhanced Gold Nanoparticle Photoluminescence". *ACS Photonics* **1** (2014), 1224–1230.

[277] B. Knoll and F. Keilmann. "Enhanced dielectric contrast in scattering-type scanning near-

field optical microscopy". *Optics Communications* **182** (2000), 321–328.

[278] P. Aravind and H. Metiu. "The effects of the interaction between resonances in the electromagnetic response of a sphere-plane structure; applications to surface enhanced spectroscopy". *Surface Science* **124** (1983), 506–528.

[279] I. Romero et al. "Plasmons in nearly touching metallic nanoparticles: singular response in the limit of touching dimers". *Optics Express* **14** (2006), 9988.

[280] J. A. Porto et al. "Resonance shift effects in apertureless scanning near-field optical microscopy". *Physical Review B* **67** (2003), 085409. arXiv: 0208481 [cond-mat].

[281] V. Kravtsov et al. "Control of Plasmon Emission and Dynamics at the Transition from Classical to Quantum Coupling". *Nano Letters* **14** (2014), 5270–5275. arXiv: 1011.1669v3.

[282] H. Cory et al. "Electric field intensity variation in the vicinity of a perfectly conducting conical probe: Application to near-field microscopy". *Microwave and Optical Technology Letters* **18** (1998), 120–124.

[283] J. Aizpurua, S. P. Apell, and R. Berndt. "Role of tip shape in light emission from the scanning tunneling microscope". *Physical Review B* **62** (2000), 2065–2073.

[284] a. L. Demming, F. Festy, and D. Richards. "Plasmon resonances on metal tips: Understanding tip-enhanced Raman scattering". *The Journal of Chemical Physics* **122** (2005), 184716.

[285] R. M. Roth et al. "Resonant-plasmon field enhancement from asymmetrically illuminated conical metallic-probe tips." *Optics Express* **14** (2006), 2921–2931.

[286] N. A. Issa and R. Guckenberger. "Fluorescence near metal tips: The roles of energy transfer and surface plasmon polaritons." *Optics Express* **15** (2007), 12131–12144.

[287] Z. Yang, J. Aizpurua, and H. Xu. "Electromagnetic field enhancement in TERS configurations". *Journal of Raman Spectroscopy* **40** (2009), 1343–1348.

[288] J. Zuloaga, E. Prodan, and P. Nordlander. "Quantum plasmonics: Optical properties and tunability of metallic nanorods". *ACS Nano* **4** (2010), 5269–5276.

[289] T. V. Teperik et al. "Quantum effects and nonlocality in strongly coupled plasmonic nanowire dimers". *Optics Express* **21** (2013), 27306.

[290] S. Raza et al. "Nonlocal optical response in metallic nanostructures". *Journal of Physics Condensed Matter* **27** (2015).

[291] R. Esteban et al. "Bridging quantum and classical plasmonics with a quantum-corrected model". *Nature Communications* **3** (2012), 825.

[292] K. J. Savage et al. "Revealing the quantum regime in tunnelling plasmonics". *Nature* **491** (2012), 574–577.

[293] J. a. Scholl et al. "Observation of Quantum Tunneling between Two Plasmonic Nanoparticles". *Nano Letters* **13** (2013), 564–569.

[294] K. Konishi and G. Paffuti. *Quantum Mechanics - A New Introduction*. 1st ed. Oxford, New York: Oxford University Press, 2009.

[295] J. Bardeen. "Tunnelling from a Many-Particle Point of View". *Physical Review Letters* **6** (1961), 57–59.

[296] C. J. Chen. *Introduction to Scanning Tunneling Microscopy*. 2nd ed. New York: Oxford University Press, 2008.

[297] B. Numerov. "Note on the numerical integration of d2x/dt2 =f(x,t)". *Astronomische Nachrichten* **230** (1927), 359–364.

[298] J. Bono and R. H. Good. "Conductance oscillations in scanning tunneling microscopy as a probe of the surface potential". *Surface Science* **188** (1987), 153–163.

[299] V. Gerstner et al. "Femtosecond laser assisted scanning tunneling microscopy". *Journal of Applied Physics* **88** (2000), 4851.

[300] M. Mehlhorn et al. "Local investigation of femtosecond laser induced dynamics of water nan-

oclusters on Cu(111)". *Physical Review Letters* **103** (2009), 1–4.

[301] M. Mehlhorn, H. Gawronski, and K. Morgenstern. "Diffusion and Dimer Formation of CO Molecules Induced by Femtosecond Laser Pulses". *Physical Review Letters* **104** (2010), 076101.

[302] H. Böckmann et al. "Direct Observation of Photoinduced Tautomerization in Single Molecules at a Metal Surface". *Nano Letters* **16** (2016), 1034–1041.

[303] S. Li et al. "Joint Space-Time Coherent Vibration Driven Conformational Transitions in a Single Molecule". *Physical Review Letters* **119** (2017), 176002.

[304] H. Böckmann et al. "Near-Field Enhanced Photochemistry of Single Molecules in a Scanning Tunneling Microscope Junction". *Nano Letters* **18** (2018), 152–157.

[305] S. Li et al. "Bond-Selected Photodissociation of Single Molecules Adsorbed on Metal Surfaces". *Physical Review Letters* **122** (2019), 077401.

[306] H. Böckmann et al. "Near-Field Spectral Response of Optically Excited Scanning Tunneling Microscope Junctions Probed by Single-Molecule Action Spectroscopy". *Journal of Physical Chemistry Letters* **10** (2019), 2068–2074.

[307] E. Kazuma et al. "Real-space and real-time observation of a plasmon-induced chemical reaction of a single molecule". *Science* **360** (2018), 521–526.

[308] L. Bartels et al. "Real-Space observation of molecular motion induced by femtosecond laser pulses". *Science* **305** (2004), 648–651.

[309] J. Lee et al. "Vibronic motion with joint angstrom-femtosecond resolution observed through Fano progressions recorded within one molecule". *ACS Nano* **8** (2014), 54–63.

[310] H. Imada et al. "Single-Molecule Investigation of Energy Dynamics in a Coupled Plasmon-Exciton System". *Physical Review Letters* **119** (2017), 1–6.

[311] J. Kröger et al. "Fano Description of Single-Hydrocarbon Fluorescence Excited by a Scanning Tunneling Microscope". *Nano Letters* **18** (2018), 3407–3413. arXiv: 1801.07143.

[312] M. Mehlhorn et al. "An instrument to investigate femtochemistry on metal surfaces in real space". *Review of Scientific Instruments* **78** (2007), 033905.

[313] S. W. Wu, N. Ogawa, and W. Ho. "Atomic-scale coupling of photons to single-molecule junctions." *Science* **312** (2006), 1362–5.

[314] S. W. Wu and W. Ho. "Two-photon-induced hot-electron transfer to a single molecule in a scanning tunneling microscope". *Physical Review B* **82** (2010), 085444.

[315] Y. Terada et al. "Real-space imaging of transient carrier dynamics by nanoscale pump–probe microscopy". *Nature Photonics* **4** (2010), 869–874.

[316] S. Yoshida et al. "Nanoscale probing of transient carrier dynamics modulated in a GaAs–PIN junction by laser-combined scanning tunneling microscopy". *Nanoscale* **4** (2012), 757.

[317] P. Kloth, K. Kaiser, and M. Wenderoth. "Controlling the screening process of a nanoscaled space charge region by minority carriers". *Nature Communications* **7** (2016), 10108.

[318] L. Sun et al. "Optical Stark effect of a local defect on the TiO2(110) surface". *Physical Review B* **98** (2018), 081402.

[319] C. Chen, N. Hayazawa, and S. Kawata. "A 1.7 nm resolution chemical analysis of carbon nanotubes by tip-enhanced Raman imaging in the ambient". *Nature Communications* **5** (2014), 1–5.

[320] S. Jiang et al. "Distinguishing adjacent molecules on a surface using plasmon-enhanced Raman scattering". *Nature Nanotechnology* **10** (2015), 865–869.

[321] J. Lee et al. "Microscopy with a single-molecule scanning electrometer". *Science Advances* **4** (2018), eaat5472.

[322] T. L. Cocker et al. "An ultrafast terahertz scanning tunnelling microscope". *Nature Photonics* **7** (2013), 620–625.

[323] P. Kloth et al. "A versatile implementation of pulsed optical excitation in scanning tunneling microscopy". *Review of Scientific Instruments* **87** (2016), 123702.

[324] O. Takeuchi et al. "New delay-time modulation scheme for optical pump–probe scanning tunneling microscopy (OPP-STM) with minimized light-intensity modulation". *Japanese Journal of Applied Physics* **58** (2019), SIIA12.

[325] N. N. Khusnatdinov, T. J. Nagle, and G. Nunes. "Ultrafast scanning tunneling microscopy with 1 nm resolution". *Applied Physics Letters* **77** (2000), 4434–4436.

[326] S. Yoshida et al. "Subcycle Transient Scanning Tunneling Spectroscopy with Visualization of Enhanced Terahertz Near Field". *ACS Photonics* **6** (2019), 1356–1364.

[327] J. K. Gimzewski et al. "Enhanced Photon Emission in Scanning Tunnelling Microscopy". *Europhysics Letters (EPL)* **8** (1989), 435–440.

[328] R. Berndt, J. K. Gimzewski, and P. Johansson. "Inelastic tunneling excitation of tip-induced plasmon modes on noble-metal surfaces". *Physical Review Letters* **67** (1991), 3796–3799.

[329] M. Bischoff, M. van der Wielen, and H. van Kempen. "STM-induced photon emission spectroscopy of granular gold surfaces in air". *Surface Science* **400** (1998), 127–133.

[330] N. Nilius, N. Ernst, and H.-J. Freund. "Tip influence on plasmon excitations in single gold particles in an STM". *Physical Review B* **65** (2002), 1–8.

[331] G. Schull et al. "Electron-plasmon and electron-electron interactions at a single atom contact". *Physical Review Letters* **102** (2009), 1–4.

[332] A. Yu et al. "Visualization of Nanoplasmonic Coupling to Molecular Orbital in Light Emission Induced by Tunneling Electrons". *Nano Letters* **18** (2018), 3076–3080.

[333] Y. Zhang et al. "Sub-nanometre control of the coherent interaction between a single molecule and a plasmonic nanocavity". *Nature Communications* **8** (2017), 1–7.

[334] A. Rosławska et al. "Single Charge and Exciton Dynamics Probed by Molecular-Scale-Induced Electroluminescence". *Nano Letters* **18** (2018), 4001–4007.

[335] C. C. Leon et al. "Photon superbunching from a generic tunnel junction". *Science Advances* **5** (2019), eaav4986.

[336] V. Gerstner, A. Thon, and W. Pfeiffer. "Thermal effects in pulsed laser assisted scanning tunneling microscopy". *Journal of Applied Physics* **87** (2000), 2574.

[337] O. Takeuchi et al. "Development of Time-Resolved Scanning Tunneling Microscopy in Femtosecond Range". *Japanese Journal of Applied Physics* **41** (2002), 4994–4997.

[338] O. T. M. Aoyama et al. "Probing subpicosecond dynamics using pulsed laser combined scanning tunneling microscopy". *Applied Physics Letters* **85** (2004), 3268–3270.

[339] X. Meng et al. "Two-color field enhancement at an STM junction for spatiotemporally resolved photoemission". *Optics Letters* **42** (2017), 2651.

[340] J. Lee et al. "Laser-induced scanning tunneling microscopy: Linear excitation of the junction plasmon". *The Journal of Chemical Physics* **133** (2010), 104706.

[341] S. Dey et al. "Nonlinear femtosecond laser induced scanning tunneling microscopy". *The Journal of Chemical Physics* **138** (2013), 154202.

[342] G. Binnig et al. "Tunneling spectroscopy and inverse photoemission: Image and field states". *Physical Review Letters* **55** (1985), 991–994.

[343] H.-C. Ploigt et al. "Local work function changes determined by field emission resonances: NaCl/Ag(100)". *Physical Review B* **76** (2007), 195404.

[344] J. Martínez-Blanco and S. Fölsch. "Light emission from Ag(111) driven by inelastic tunneling in the field emission regime". *Journal of Physics: Condensed Matter* **27** (2015), 255008. arXiv: 1503.04331.

[345] T. Kumagai et al. "Local electronic structure, work function, and line defect dynamics of ultrathin epitaxial ZnO layers on a Ag(1 1 1) surface". *Journal of Physics Condensed Matter* **28** (2016).

[346] J. Boneberg et al. "The mechanism of nanostructuring upon nanosecond laser irradiation of a STM tip". *Applied Physics A: Materials Science and Processing* **67** (1998), 381–384.

[347] S. Grafström et al. "Thermal expansion of scanning tunneling microscopy tips under laser illumination". *Journal of Applied Physics* **83** (1998), 3453–3460.

[348] N. Xie et al. "Tip expansion in a laser assisted scanning tunneling microscope". *Applied Physics Letters* **101** (2012), 213104.

[349] P. Bharadwaj, A. Bouhelier, and L. Novotny. "Electrical Excitation of Surface Plasmons". *Physical Review Letters* **106** (2011), 226802. arXiv: 1103.5260.

[350] C. Cohen-Tannoudji, B. Diu, and F. Laloe. *Quantum Mechanics: Volume I: Basic Concepts, Tools, and Applications*. 2nd ed. Wiley-VCH, 2019.

[351] S. Liu, M. Wolf, and T. Kumagai. "Plasmon-Assisted Resonant Electron Tunneling in a Scanning Tunneling Microscope Junction". *Physical Review Letters* **121** (2018), 226802.

[352] J. Hohlfeld et al. "Electron and lattice dynamics following optical excitation of metals". *Chemical Physics* **251** (2000), 237–258.

[353] P. Echenique et al. "Image-potential-induced states at metal surfaces". *Journal of Electron Spectroscopy and Related Phenomena* **126** (2002), 163–175.

[354] E. Chulkov, V. Silkin, and P. Echenique. "Image potential states on metal surfaces: binding energies and wave functions". *Surface Science* **437** (1999), 330–352.

[355] E. Teague. "Room Temperature Gold-Vacuum-Gold Tunneling Experiments". *Journal of Research of the National Bureau of Standards* **91** (1986), 171.

[356] J. Eichler and H.-J. Eichler. *Laser*. 7. Auflage. Berlin, Heidelberg: Springer Berlin Heidelberg, 2010.

[357] S. Lal, S. Link, and N. J. Halas. "Nano-optics from sensing to waveguiding". *Nature Photonics* **1** (2007), 641–648.

[358] H. Böckmann et al. "Near-Field Manipulation in a Scanning Tunneling Microscope Junction with Plasmonic Fabry-Pérot Tips". *Nano Letters* (2019).

[359] S. Kim et al. "High external-efficiency nanofocusing for lens-free near-field optical nanoscopy". *Nature Photonics* (2019).

[360] G. A. Morton and E. G. Ramberg. "Point Projector Electron Microscope". *Physical Review* **56** (1939), 705–705.

[361] A. R. Bainbridge, C. W. Barlow Myers, and W. A. Bryan. "Femtosecond few- to single-electron point-projection microscopy for nanoscale dynamic imaging". *Structural Dynamics* **3** (2016), 023612. arXiv: 1512.00328.

[362] K. Toma et al. "Control of grating-coupled ultrafast surface plasmon pulse and its nonlinear emission by shaping femtosecond laser pulse". *Journal of Applied Physics* **118** (2015), 103102.

[363] E. A. Pozzi et al. "Ultrahigh-Vacuum Tip-Enhanced Raman Spectroscopy". *Chemical Reviews* **117** (2017), 4961–4982.

[364] J. Heimerl et al. "Gap-size dependence of optical near fields in a variable nanoscale two-tip junction". *Physical Review B* **101** (2020), 125403.

[365] C. Lin et al. "Real-space observation of far- and near-field-induced photolysis of molecular oxygen on an Ag(110) surface by visible light". *The Journal of Chemical Physics* **151** (2019), 144705.

[366] N. Tallarida et al. "Isomerization of One Molecule Observed through Tip-Enhanced Ra-

man Spectroscopy". *Nano Letters* **15** (2015), 6386–6394.

[367] A. B. Zrimsek et al. "Single-Molecule Chemistry with Surface- and Tip-Enhanced Raman Spectroscopy". *Chemical Reviews* **117** (2017), 7583–7613.

[368] Y. Zhang et al. "Visualizing coherent intermolecular dipole–dipole coupling in real space". *Nature* **531** (2016), 623–627.

[369] L. Zhang et al. "Electrically driven single-photon emission from an isolated single molecule". *Nature Communications* **8** (2017), 580.

[370] W. S. Fann et al. "Electron thermalization in gold". *Physical Review B* **46** (1992), 13592–13595.

[371] G. V. Hartland. "Optical Studies of Dynamics in Noble Metal Nanostructures". *Chemical Reviews* **111** (2011), 3858–3887.

[372] R. Berndt, J. K. Gimzewski, and P. Johansson. "Electromagnetic interactions of metallic objects in nanometer proximity". *Physical Review Letters* **71** (1993), 3493–3496.

[373] P. Johansson, R. Monreal, and P. Apell. "Theory for light emission from a scanning tunneling microscope". *Physical Review B* **42** (1990), 9210–9213.

[374] B. N. Persson and A. Baratoff. "Theory of photon emission in electron tunneling to metallic particles". *Physical Review Letters* **68** (1992), 3224–3227.

[375] C. Zhou et al. "Site-specific photocatalytic splitting of methanol on TiO2(110)". *Chemical Science* **1** (2010), 575.

[376] J. Repp et al. "Molecules on insulating films: Scanning-tunneling microscopy imaging of individual molecular orbitals". *Physical Review Letters* **94** (2005), 1–4.

[377] L. Gross et al. "The Chemical Structure of a Molecule Resolved by Atomic Force Microscopy". *Science* **325** (2009), 1110–1114.

[378] L. Gross. "Recent advances in submolecular resolution with scanning probe microscopy". *Nature Chemistry* **3** (2011), 273–278.

[379] L. Gross et al. "Bond-Order Discrimination by Atomic Force Microscopy". *Science* **337** (2012), 1326–1329.

[380] L. L. Patera et al. "Mapping orbital changes upon electron transfer with tunnelling microscopy on insulators". *Nature* **566** (2019), 245–248.

[381] K. Kaiser et al. "An sp-hybridized molecular carbon allotrope, cyclo[18]carbon". *Science* **365** (2019), 1299–1301.

[382] H. Imada et al. "Real-space investigation of energy transfer in heterogeneous molecular dimers". *Nature* **538** (2016), 364–367.

[383] C. F. Hirjibehedin, C. P. Lutz, and A. J. Heinrich. "Spin coupling in engineered atomic structures". *Science* **312** (2006), 1021–1024.

[384] S. Loth et al. "Controlling the state of quantum spins with electric currents". *Nature Physics* **6** (2010), 340–344.

[385] S. Loth et al. "Measurement of Fast Electron Spin Relaxation Times with Atomic Resolution". *Science* **329** (2010), 1628–1630.

[386] S. Yoshida et al. "Probing ultrafast spin dynamics with optical pump–probe scanning tunnelling microscopy". *Nature Nanotechnology* **9** (2014), 588–593.

[387] S. Yan et al. "Control of quantum magnets by atomic exchange bias". *Nature Nanotechnology* **10** (2015), 40–45.

[388] F. D. Natterer et al. "Reading and writing single-atom magnets". *Nature* **543** (2017), 226–228. arXiv: 1607.03977.

[389] P. Willke et al. "Hyperfine interaction of individual atoms on a surface". *Science* **362** (2018), 336–339.

[390] G. Czap et al. "Probing and imaging spin interactions with a magnetic single-molecule sensor". *Science* **364** (2019), 670–673.

[391] K. Yang et al. "Coherent spin manipulation of individual atoms on a surface". *Science* **366** (2019), 509–512.

[392] P. Willke et al. "Magnetic resonance imaging of single atoms on a surface". *Nature Physics* **15** (2019), 1005–1010. arXiv: 1807.08944.

[393] A. A. Tseng and Z. Li. "Manipulations of Atoms and Molecules by Scanning Probe Microscopy". *Journal of Nanoscience and Nanotechnology* **7** (2007), 2582–2595.

[394] J. L. Zhang et al. "Towards single molecule switches". *Chemical Society Reviews* **44** (2015), 2998–3022.

[395] K. R. Rusimova et al. "Regulating the femtosecond excited-state lifetime of a single molecule". *Science* **361** (2018), 1012–1016.

[396] T. Esat et al. "A standing molecule as a single-electron field emitter". *Nature* **558** (2018), 573–576.

[397] M. J. Comstock et al. "Reversible Photomechanical Switching of Individual Engineered Molecules at a Metallic Surface". *Physical Review Letters* **99** (2007), 038301.

[398] K. Watanabe et al. "Photochemistry on Metal Nanoparticles". *Chemical Reviews* **106** (2006), 4301–4320.

[399] Y. Zhang et al. "Surface-Plasmon-Driven Hot Electron Photochemistry". *Chemical Reviews* **118** (2018), 2927–2954.

[400] J. S. Lee et al. "Superfocusing of electric or magnetic fields using conical metal tips: effect of mode symmetry on the plasmon excitation method." *Optics Express* **19** (2011), 12342–12347.

[401] X.-Y. Zhu. "Surface photochemistry". *Surface Science* **299-300** (1994), 996–1007.

[402] O. M. Probst. "Tunneling through arbitrary potential barriers and the apparent barrier height". *American Journal of Physics* **70** (2002), 1110–1116.

[403] N. V. Smith, C. T. Chen, and M. Weinert. "Distance of the image plane from metal surfaces". *Physical Review B* **40** (1989), 7565–7573.

[404] J. Pitarke, F. Flores, and P. Echenique. "Tunneling spectroscopy: surface geometry and interface potential effects". *Surface Science* **234** (1990), 1–16.

Author contributions

This dissertation is authored by Benjamin Schröder (B.S.) within the doctoral program of the Georg-August School of Science (GAUSS) and according to the doctoral regulations RerNat-O 2018. The scientific contribution is discussed in the chaps. 3, 4, and 5 which base on three peer-reviewed articles published with B.S. as the leading author,

1. B. Schröder, T. Weber, S. V Yalunin, T. Kiel, C. Matyssek, M. Sivis, S. Schäfer, F. von Cube, S. Irsen, K. Busch, C. Ropers, and S. Linden, Real-space imaging of nanotip plasmons using electron energy loss spectroscopy, Phys. Rev. B **92** (2015), 085411,

2. B. Schröder, M. Sivis, R. Bormann, S. Schäfer, and C. Ropers, An ultrafast nanotip electron gun triggered by grating-coupled surface plasmons, Appl. Phys. Lett. **107** (2015), 231105,

3. B. Schröder, O. Bunjes, L. Wimmer, K. Kaiser, G. A. Traeger, T. Kotzott, C. Ropers, and M. Wenderoth, Controlling Photocurrent Channels in Scanning Tunneling Microscopy, New J. Phys. **22** (2020), 033047.

These articles are reprinted in accordance to the original work in the sec. 3.3, 4.2, and 5.3 (except for adaptions of quantity notations and reference order). All studies represent the work done by B.S. including sample preparation, design and setup of the experiments, data acquisition, simulation, modeling, and data analysis with the following particularities:

1. B.S. and Thorsten Weber (T.W.) (group of Stefan Linden (S.L.) from the university of Bonn) equally contributed to this study. Tip sample holders have been prepared (transfer to TEM grid holder by a focused ion beam (FIB) instrument) together with Murat Sivis (M.S.). EELS data sets have been acquired by B.S. together with T.W. and Felix von Cube in the group of Stephan Irsen from the caesar institute in Bonn. The analytical modeling and finite-element calculations describing the electron energy loss at nanotips have been developed by Sergey V. Yalunin (S.V.Y.), Christian Matyssek (C.M.) and Thomas Kiel (T.K.) (C.M. and T.K. are in the group of Kurt Busch from the Max Born institute in Berlin). The analytical model has been published in another article authored by S.V.Y., B.S., and Claus Ropers (C.R.) briefly discussed in sec. 3.4. Data analysis was conducted by B.S. and T.W.. The publication was mainly drafted by B.S., T.W., S.L., and C.R..

2. The grating structures have been prepared by M.S. with FIB. Data analysis has been performed by B.S. with some references to the work of Reiner Bormann. The publication was drafted by B.S., M.S., Sascha Schäfer, and C.R..

3. The scanning tunneling microscope (STM) was set up by Bernhard Spicher, Georg Traeger (G.T.), Martin Wenderoth (M.W.), and B.S.. B.S., Katharina Kaiser (K.K.),

and G.T. established the fs-laser beam line fed into the STM and the beam stabilization optimization (sec. 5.4) within the master thesis of K.K.. Samples (Copper crystals with Germanium clusters) have been prepared by Thomas Kotzott. STM measurements are conducted with the help of Ole Bunjes (O.B.). The electron transport model (secs. 5.2 and 5.3.9) has been implemented by B.S. and Lara Wimmer. Data analysis and manuscript preparation have been accomplished by B.S., O.B., M.W., and C.R..

Related co-authored publications

- S. V. Yalunin, B. Schröder, and C. Ropers, Theory of electron energy loss near plasmonic wires, nanorods, and cones, Phys. Rev. B **93** (2016), 115408,
- L. Wimmer, B. Schröder, M. Sivis, G. Herink and C. Ropers, Clocking plasmon nanofocusing by THz near-field streaking, Appl. Phys. Lett. **111** (2017), 131102.

Conference and workshop contributions

- Poster presentation: *Real-space imaging of nanotip plasmons using electron energy loss spectroscopy*, DPG Frühjahrstagung (SKM), 2015, Berlin, Germany
- Talk: *Real-space imaging of nanotip plasmons using electron energy loss spectroscopy*, 7th International Conference on Surface Plasmon Photonics (SPP7), 2015, Jerusalem, Israel
- Poster presentation: *Nanotip surface plasmons: real-space imaging using EELS and grating-coupled nonlinear photoemission*, 4th International Workshop on Ultrafast Nanooptics (UNO4), 2015, Bad Dürkheim, Germany
- Poster presentation: *Real-space imaging of nanotip plasmons using electron energy loss spectroscopy*, DPG Frühjahrstagung (SKM), 2016, Regensburg, Germany
- Talk: *An Ultrafast Nanotip Electron Gun Triggered by Grating-Coupled Surface Plasmons*, DPG Frühjahrstagung (SKM), 2016, Regensburg, Germany
- Poster presentation: *Real-space imaging of nanotip plasmons using electron energy loss spectroscopy*, Summer School on Interfaces and Energy, 2016, Göttingen, Germany
- Talk: *Near-field Driven Nonlinear Photoemission from the Tunnel Junction of a Scanning Tunneling Microscope*, DPG Frühjahrstagung (SKM), 2018, Berlin, Germany
- Talk: *Near-Field Driven Photo-Assisted Tunneling in a Scanning Tunneling Microscope*, DPG Frühjahrstagung (SKM), 2019, Regensburg, Germany
- Poster presentation: *Ultrafast Near-Field Driven Electron Transfer Through a Tunnel Junction in a Scanning Tunneling Microscope*, International Workshop on Correlated Dynamics in Energy Conversion (IWCE2019), 2019, Göttingen, Germany

Acknowledgement

An dieser Stelle möchte ich mich bei den Menschen bedanken, die mich bei dieser Arbeit unterstützt haben.

Ganz besonders danke ich Prof. Dr. Claus Ropers für die exzellente Betreuung dieser Arbeit, für die Motivation und Inspiration, die auch über schwierigere Zeiten hinweghalfen und für die spannende Forschung, an der ich beteiligt bin. Direkt daran anschließend möchte ich PD Dr. Martin Wenderoth meinen besonderen Dank für die hervorragende Betreuung, lehrreichen Diskussionen und Aufnahme in seine Arbeitsgruppe aussprechen. Nicht nur auf wissenschaftlicher, sondern auch auf persönlicher Ebene war die Arbeit in beiden Gruppen sehr bereichernd.

Prof. Alec M. Wodtke, PhD danke ich sehr für den Einsatz als Korreferent und im Betreuungsausschluss.

Für die tolle wissenschaftliche und technische Zusammenarbeit möchte ich mich namentlich bei (alphabetische Ordnung) Bernhard Spicher, Georg Traeger, Karin Ahlborn, Katharina Kaiser, Dr. Lara Wimmer, Dr. Max Gulde, Dr. Murat Sivis, Ole Bunjes, Dr. Reiner Bormann, Prof. Dr. Sascha Schäfer, Prof. Dr. Sergey Yalunin und Thomas Kotzott bedanken. Den Mitgliedern aus beiden Gruppen empfinde ich große Dankbarkeit nicht nur für die inspirierenden Diskussionen und die gegenseitige Motivation, sondern vor allem für die offenen Ohren und tröstenden Worte, die mir über eine schwere Zeit hinweghalfen, die mich während der Promotion ereilte. Ich habe enge Freundschaften geschlossen!

Großer Dank geht auch an die Gruppen von Prof. Dr. Stefan Linden und Dr. Stephan Irsen in Bonn und Prof. Dr. Kurt Busch in Berlin für die fruchtbare Zusammenarbeit. Insbesondere den Gruppenmitgliedern Dr. Thorsten Weber und Dr. Felix von Cube danke ich für die freundliche Aufnahme in Bonn und die schöne Zeit beim Messen.

Für die Unterstützung in feinmechanischen und elektrischen Belangen danke ich Rasit Kösker, Christof Schmidt und Alexander Gehrt und ihren Teams.

Ich danke Dr. Andreas Blumenstein, Dr. Armin Feist, Frank Westholt, Gerrit Schröder, Ole Bunjes und Dr. Philipp Kloth für das engagierte Korrekturlesen und die hilfreichen Tipps bei der Erstellung dieser Arbeit.

Zu guter Letzt danke ich von Herzen den Menschen, die mich über die letzten Jahre getragen (und ertragen) haben. Ganz besonders danke ich meiner Frau Julia, die mir den nötigen Rückhalt gegeben und besonders in der finalen Zeit den Rücken freigehalten hat. Sie schenkte Vertrauen auch dann, wenn ich zweifelte! Mein Sohn Jannis verdient ebenfalls Dank für den schweren Verzicht auf gemeinsame Zeit, in der ich die “Dokdokarbeit” verfasste. Meinen Eltern Mechthild und Peter und meiner Schwester Franziska danke ich vor allen anderen Dingen für ihren Glauben an mich und ihre unerschöpfliche Unterstützung. Schließlich gebührt auch all meinen Freunden Dankbarkeit für die dringend nötige Ablenkung, sei es durch Computer- oder Rollenspiel, Reisen, Hausbau oder Mountainbiking.